

**VISUAL FUNCTION AND RETINAL STRUCTURE WITH GANGLION CELL  
ABLATION AND IN MYOPIA**

By

Ashutosh Jnawali

A DISSERTATION submitted to the Graduate Faculty,  
of the College of Optometry, University of Houston,

in partial fulfillment of the requirements for the degree of

Doctor of Philosophy

in

PHYSIOLOGICAL OPTICS AND VISION SCIENCE

Chair of Committee: Lisa A Ostrin, OD, Ph.D., FAAO

Committee Member: Laura J Frishman, Ph.D., FAAO, FARVO

Committee Member: Nimesh B Patel, OD, Ph.D., FAAO

Committee Member: Christine F Wildsoet, OD, Ph.D., FAAO, FARVO

University of Houston  
May 2020

## DEDICATION/EPIGRAPH

कर्मण्येवाधिकारस्ते मा फलेषु कदाचन ।  
माकर्मफलहेतुर्भूर्मा ते सङ्गोऽस्त्वकर्मणि ॥

-Bhagavad Gita, Ch 2.47

“Thy concern is with action alone, never with the results. Let not the fruit of action be thy motive, nor let thy attachment be for inaction.”

## ACKNOWLEDGMENTS

I am immensely grateful for everyone who have helped me in this journey of doctoral degree. Firstly, I would like to express my sincere gratitude to my advisor Dr. Lisa Ostrin for her continuous guidance and support on my dissertation work and on all the related projects. She continually motivated and guided me through all aspects of my projects, and always provided a friendly environment which always put me at ease to approach her with any difficulty at work. I am thankful to her for providing me with so many opportunities to learn new techniques with various aspects of different projects. Her guidance also helped me immensely with the writing of this dissertation and all publications associated with the works that form this dissertation. I would also like to thank Dr. Laura Frishman for all her guidance on my path in the graduate program. She enabled me to not only learn ERG recordings in mice, rats and guinea pigs, but also helped me understand, analyze and interpret the results from the recordings. I am very thankful to her for her guidance with all the advising and reading sessions. I want to thank Dr. Nimesh Patel for his valuable guidance with OCT imaging and analysis, and for enabling me to learn programming for OCT image analysis, which was integral part of my dissertation work. I am also thankful to him for his time, very helpful discussions and suggestions on various aspects of the projects. I also thank Dr. Christine Wildsoet for her helpful interactions at various scientific meetings, and for her important suggestions on my proposal and dissertation.

I want to thank all my friends from Ostrin lab, including past and present lab members. They have been always helpful in maintaining a great positive atmosphere for all the work that goes on in the lab, and they have always extended their help with my experiments. I am also thankful to my colleagues, especially Suman, Gareth and Laura, who have always been there from day one of our journey in the graduate program, and I am grateful to them for sharing their

friendship with wonderful memories and making this journey a pleasant one. I am also thankful to all the graduate students at UHCO, who make the graduate program so much fun. I want to thank Dr. Krista Beach, a past member of Ostrin lab, for helping me learn histology and immunohistochemistry, which were crucial for the guinea pig experiments. I want to thank Dr. Alan Burns for his help with the DeltaVision core microscope. I am very thankful to Lin Xiao, another graduate student in our program, who helped me with the guinea pig optic nerve crush experiments at a crucial time. I want to thank my parents Prof. Dr. Damodar Jnawali and Mrs. Kalpana Jnawali, who have been my role models in performing their duties, and who provided great environment for my academic and spiritual growth. I am thankful to my sisters Mrs. Anuradha Jnawali and Dr. Anasooya Jnawali for their immense love and care that has made my life so beautiful. I would like to express my humble gratitude and offerings to Bhagawan Sri Sathya Sai Baba, my spiritual teacher and master, whose guidance and teachings have made a profound effect on my life.

I want to give special thanks to the Animal Care Operations for all their help with taking care of our animals and ensuring that our experiments ran smoothly. I acknowledge and thank the grants K08 EY022696 (PI- Dr. Lisa Ostrin) and P30 EY007751 (PI- Dr. Laura Frishman) for making all this work possible.

## ABSTRACT

**Purpose:** The guinea pig is a model of human retinal physiology and pathology. However, detailed understanding of retinal structure and function is lacking. Here we describe retinal structure and function in healthy guinea pigs, and develop a model of ganglion cell loss. Using imaging analysis techniques developed in these studies, we then evaluated ocular parameters in school age children as a function of age, axial length, and refraction.

**Methods:** 1) In guinea pigs, spatial frequency discrimination was evaluated using optomotor responses. Retinal function was assessed using flash and pattern electroretinogram (ERG). Structure was assessed *in vivo* using spectral domain optical coherence tomography (SD-OCT). Retrograde retinal ganglion cell degeneration was induced with unilateral optic nerve crush, and changes in retinal structure and visual function were examined. Retinal ganglion cell density and distribution were quantified histologically. 2) In school age children ( $n = 53$ ), the optic nerve head, lamina cribrosa, retina, and choroid were evaluated using SD-OCT. Images were analyzed in MATLAB and assessed in relation to age, axial length, and refractive error.

**Results:** 1) Mean spatial frequency discrimination of guinea pigs was 1.65 cycles/degree. The photopic negative response (PhNR) and the oscillatory potentials (OPs) were similar to those in primates. The visual streak was localized the superior retina, with peak ganglion cell density of  $1621 \pm 129$  cells/mm<sup>2</sup>. With unilateral optic nerve crush, loss of optomotor responses, thinning of retinal nerve fiber layer, and reduction of PhNR and OP1 amplitudes were observed. Pattern ERG responses were largely unaffected. 2) In children, minimum foveal thickness and retinal thickness increased with age. Bruch's membrane opening area increased with myopic refractive error, and vertical cup-to-disc ratio decreased with increasing axial length and myopic refractive error.

**Conclusion:** We demonstrated that retinal ganglion cells contribute to the PhNR and OPs of flash ERG in guinea pigs. These findings will be valuable when assessing progression of ocular disease in this animal model. In school age children, we described normative values for retinal and optic nerve head parameters, and demonstrate that ocular remodeling occurs in school age children with normal eye growth and during early stages of myopia.

## TABLE OF CONTENTS

DEDICATION/EPIGRAPH .....	iv
ACKNOWLEDGMENTS .....	v
ABSTRACT.....	vii
TABLE OF CONTENTS.....	ix
LIST OF TABLES .....	xii
LIST OF FIGURES .....	xiv
CHAPTER 1: INTRODUCTION .....	1
1.1 Introduction to Myopia .....	1
1.2 Potential complications of myopia and association with glaucoma .....	2
1.3 Guinea Pig as a model of myopia .....	2
1.4 Potential role of guinea pig as a model of optic neuropathy and glaucoma .....	3
1.5 Retinal structural assessment in myopia and glaucoma.....	4
1.6 Visual function assessment in myopia and glaucoma.....	5
1.7 Purpose of studies in guinea pigs and in children.....	10
1.7 Overall methodology .....	12
1.8 Overview of dissertation chapters.....	13
CHAPTER 2 : EVALUATION OF VISUAL FUNCTION IN GUINEA PIG WITH BEHAVIORAL AND ELECTROPHYSIOLOGICAL METHODS.....	16
2.1 Introduction.....	16
2.3 Methods.....	19
2.3.1 Animals .....	19
2.3.2 Optomotor responses .....	19
2.3.3 Electroretinography.....	21
2.3.4 Ganglion cell quantification.....	22
2.3.5 Statistical Analysis.....	25
2.4 Results.....	25
2.4.1 Optomotor responses .....	25
2.4.2 Electroretinography.....	27
2.4.3 Ganglion cell quantification.....	32
2.5 Discussion .....	34
2.6 Conclusions.....	38
CHAPTER 3 : IN VIVO IMAGING OF THE RETINA, CHOROID AND OPTIC NERVE HEAD IN GUINEA PIGS .....	40
3.2 Introduction:.....	40

3.3 Materials and Methods.....	42
3.3.1 Animal preparation .....	43
3.3.2 Image Acquisition.....	43
3.3.3 Refraction and Biometry.....	46
3.3.4 Image analysis.....	48
3.3.5 Intraobserver, interocular, and intersession repeatability .....	52
3.3.6 Histology.....	52
3.3.7 Statistical analysis.....	53
3.4 Results.....	53
3.4.1 Refraction and Biometry.....	53
3.4.2 Thickness of retinal layers .....	55
3.4.3 Regional variations .....	57
3.4.4 Intraobserver, interocular, and intersession repeatability .....	59
3.4.5 In vivo versus histological measurements .....	64
3.5 Discussion.....	67
3.5.1 Biometry .....	67
3.5.2 Refractive Indices .....	68
3.5.3 Comparing measurements from in vivo imaging with histological measurements .....	68
3.5.4 RNFL thickness .....	69
3.5.5 Retinal Thickness in Rodents.....	69
3.5.6 Visual Streak and Retinal Thickness .....	70
3.5.7 Previous Findings.....	70
3.5.8 Limitations of Study .....	72
3.6 Conclusions.....	73
CHAPTER 4 : RETINAL GANGLION CELL ABLATION IN GUINEA PIGS	74
4.2 Introduction.....	74
4.2 Methods.....	76
4.2.1 Optic nerve crush procedure .....	76
4.2.2 Behavioral visual function .....	77
4.2.3 Ocular Imaging .....	77
4.2.4 Electrophysiology .....	81
4.2.5 Intravitreal Injections .....	82
4.2.6 In vitro ganglion cell quantification.....	83
4.2.7 Statistical Analysis.....	86
4.3 Results.....	86
4.3.1 Behavioral vision .....	86
4.3.2 Retinal structure .....	86
4.3.3 Full field flash ERG.....	90
4.3.4 Effects of GABA on the flash and pattern ERG .....	95
4.4 Discussion.....	100

4.5 Conclusions.....	106
<b>CHAPTER 5 : THE OPTIC NERVE HEAD, LAMINA CRIBROSA, AND NERVE FIBER LAYER IN NON-MYOPIC AND MYOPIC CHILDREN .....</b>	<b>107</b>
5.2 Introduction.....	107
5.3 Methods.....	109
5.3.1 Subjects .....	109
5.3.2 Image Acquisition.....	110
5.3.3 Image analysis.....	112
5.3.4 Statistical Analysis.....	119
5.4 Results.....	119
5.4.1 Subjects .....	119
5.4.2 Optic Nerve Head and Lamina Cribrosa Structure .....	122
5.4.3 Macular Structure.....	128
5.3.4 Interocular Symmetry .....	130
5.5 Discussion.....	130
<b>CHAPTER 6: DISCUSSION.....</b>	<b>135</b>
<b>REFERENCES: .....</b>	<b>146</b>

## LIST OF TABLES

<b>Table 2-1:</b> Amplitude ( $\mu\text{V}$ ) and implicit times (ms) of the a-wave, b-wave, and photopic negative response (PhNR) of the full field flash ERG from adult guinea pigs ( $n = 6$ ) for flash strength of $10.0 \text{ cd.s/m}^2$ .....	29
<b>Table 2-2:</b> Amplitude ( $\mu\text{V}$ ) and implicit time (ms) for pattern ERG components from adult guinea pigs ( $n=6$ ) for alternating stimuli of spatial frequencies ranging from 0.025 to 0.25 cycles per degree; the first negative trough (N1), positive peak (P1), and second negative trough (N2), as well as the N1P1 and P1N2 components, are shown .....	30
<b>Table 3-1:</b> Spherical equivalent refraction and biometric measurements, including central corneal thickness, anterior chamber depth, lens thickness, axial length, and mean corneal power, for right (OD) and left (OS) eyes ( $n = 8$ ), compared with paired t-test.....	54
<b>Table 3-2:</b> Intraobserver measures for the left eye of each animal ( $n = 9$ ), measurements compared with paired t-test (* indicates significance at $p < 0.05$ ), intraclass correlation coefficient (ICC), 95% confidence interval (CI), and coefficient of variation (CV).....	60
<b>Table 3-3:</b> Interocular measures for each animal ( $n = 8$ ); right and left eyes are compared with paired t-test (* indicates significance at $p < 0.05$ ), intraclass correlation coefficient (ICC), 95% confidence interval (CI), and coefficient of variation (CV) .....	61
<b>Table 3-4:</b> Intersession measures for the left eye of each animal ( $n = 9$ ), sessions compared with paired t-test (* indicates significance at $p < 0.05$ ), intraclass correlation coefficient (ICC), 95% confidence interval (CI), and coefficient of variation (CV) .....	62
<b>Table 3-5:</b> Measures derived from OCT imaging and histology for the same eyes ( $n = 7$ )	66
<b>Table 4-1:</b> Retinal nerve fiber layer thickness ( $\mu\text{m}$ ) by quadrant at baseline and following optic nerve crush in right eyes; ** = $P < 0.01$ at 12 week .....	88
<b>Table 4-2:</b> Amplitude ( $\mu\text{V}$ ) of ERG waves before and 10 min after intravitreal injections of GABA in the left eyes of young guinea pigs ( $n=6$ ) .....	96
<b>Table 5-1:</b> Subject characteristics and biometry ( $n = 52$ ); P values are shown for unpaired t-tests between non-myopes ( $n = 29$ ) and myopes ( $n = 23$ ).....	121
<b>Table 5-2:</b> Relationships of optic nerve head parameters, including Bruch's membrane opening (BMO) area, minimum rim width (MRW), anterior lamina cribrosa surface depth (ALCSD), and vertical and horizontal cup-to-disc ratio, with axial length (AL) and spherical equivalent refractive error (SER), for all subjects ( $n = 52$ ); age-adjusted $R^2$ and P values are shown for multiple regression analysis.....	123

**Table 5-3:** Global and sectoral peripapillary choroidal thicknesses for all subjects (n = 51), for non-myopes (n = 28), and for myopes (n = 23); repeated measures ANOVA showed a significant difference by sector ( $P < 0.001$ ) but not by refractive error group ( $P = 0.09$ ).....125

**Table 5-4:** Scaled global and sectoral peripapillary RNFL thicknesses for all subjects (n = 49), for non-myopes (n = 29), and for myopes (n = 23); repeated measures ANOVA showed that peripapillary RNFL thickness varied by sector ( $P < 0.001$ ), but not by refractive error group ( $P = 0.23$ ). .....127

**Table 5-5:** Total global and sectoral retinal thicknesses ( $\mu\text{m}$ ) in the 6 mm annulus for all subjects (n = 52), for non-myopes (n = 29), and for myopes (n = 23); repeated measures ANOVA showed that macular retinal thickness varied by sector ( $P < 0.001$ ), but not by refractive error group ( $P = 0.79$ ).....129

## LIST OF FIGURES

<b>Figure 1-1:</b> Representative traces of light adapted flash ERG responses .....	8
<b>Figure 1-2:</b> Schematic diagram of an optokinetic drum setup.....	9
<b>Figure 2-1:</b> Behavioral assessment of spatial frequency discrimination in guinea pigs.....	20
<b>Figure 2-2:</b> Representative images on ganglion cell counting.....	24
<b>Figure 2-3:</b> Spatial frequency sensitivity in adult guinea pigs.....	26
<b>Figure 2-4:</b> Representative raw traces for flash and pattern ERG .....	28
<b>Figure 2-5:</b> N1P1 and P1N2 amplitudes of pattern ERG for different spatial frequencies .....	31
<b>Figure 2-6:</b> Representative retinal ganglion cell density heat map.....	33
<b>Figure 3-1:</b> Representative scanning laser ophthalmoscope images of the ONH.....	45
<b>Figure 3-2:</b> Representative biometry images from Lenstar compared against enucleated globe.....	47
<b>Figure 3-3:</b> Representative B-scan images from radial scans at the ONH .....	49
<b>Figure 3-4:</b> Representative segmentation images of circular and radial scans at the ONH .....	51
<b>Figure 3-5:</b> A point cloud illustration of the ILM and BMO points .....	56
<b>Figure 3-6:</b> Thickness maps derived from 24 line radial scans .....	58
<b>Figure 3-7:</b> Intersession Bland-Altman analysis.....	63
<b>Figure 3-8:</b> Representative images comparing OCT b-scan with histological section .....	65
<b>Figure 4-1:</b> SD-OCT imaging of the guinea pig retina.....	80
<b>Figure 4-2:</b> Retinal flat mount images from guinea pig eyes at 20X.....	85
<b>Figure 4-3:</b> Retinal nerve fiber layer and total retinal thicknesses following optic nerve crush .....	89
<b>Figure 4-4:</b> Results from flash ERG following optic nerve crush .....	91
<b>Figure 4-5:</b> Results for oscillatory potentials following optic nerve crush.....	92
<b>Figure 4-6:</b> Results for pattern ERG following optic nerve crush.....	94
<b>Figure 4-7:</b> Representative images of retinal ganglion cells stained with RBPMS98	
<b>Figure 4-8:</b> Retinal ganglion cell density from all control eyes (n = 7) and optic nerve crush eyes .....	99
<b>Figure 5-1:</b> Representative SLO images and corresponding b-scan images from OCT scans.....	111

**Figure 5-2:** Representative SLO image with 48 line radial scans (green) .....115  
**Figure 5-3:** Representative macular volume scan thickness map .....118  
**Figure 5-4:** Representative point cloud for a 12 year old subject .....124

## **CHAPTER 1: INTRODUCTION**

The main research goals of this dissertation are 1) the evaluation of visual function in guinea pigs with non-invasive techniques, 2) evaluation of retinal structure in guinea pigs with non-invasive *in vivo* imaging techniques and comparison with *in vitro* measures, 3) assessment of retinal structural and functional changes in a guinea pig model of optic neuropathy, and 4) evaluation of retinal and optic nerve head parameters in non-myopic and myopic school age children as a function of age, axial length, and refraction. In this chapter, I will provide background information relevant to understanding of the rationale and critical elements of my dissertation. This chapter will include a brief introduction to myopia and its associated complications, including increased risk of glaucoma, role of guinea pig as a popular model of myopia, potential role of guinea pig as a model to study myopia and glaucoma together, retinal structure and function assessment techniques that will be used in this dissertation, and an overview of the dissertation chapters.

### ***1.1 Introduction to Myopia***

Myopia (short sightedness), the most common type of refractive error, is a condition in which parallel rays of light from distant objects focus in front of the retina when the accommodation is relaxed. Uncorrected refractive error is the most common cause of visual impairment globally, and the second most common cause of blindness globally.<sup>1</sup> The global prevalence of myopia is at an ever-increasing rate, and it is estimated that 50% of the world population will become myopic by the year 2050, with 10% of the world population projected to have high myopia by the same year.<sup>2</sup> The prevalence of myopia and high myopia varies by geography globally, and is higher in East Asian countries, with prevalence in urban areas in

these countries as high as 69-90% for myopia and 10-20% for high myopia.<sup>3, 4</sup> The prevalence of myopia is also increasing in the United States and Europe.<sup>5, 6</sup> Higher prevalence of uncorrected refractive error and myopia contribute to significant socio-economic burden.<sup>7, 8</sup>

### ***1.2 Potential complications of myopia and association with glaucoma***

Myopia is often associated with increased risk of potentially blinding conditions, such as myopic macular degeneration, cataract, choroidal neovascularization, retinal detachment, and glaucoma.<sup>9-11</sup> The prevalence of glaucoma is found to be significantly higher in high myopic eyes compared to low myopic or emmetropic eyes.<sup>12</sup> Specifically, myopic subjects have been shown to have twofold to threefold increased risk of glaucoma compared to that with non-myopic eyes.<sup>13, 14</sup> Furthermore, myopia is found to be associated with an increased prevalence of all forms of open angle glaucoma and ocular hypertension.<sup>14-19</sup> It is also suggested that glaucoma prevalence increases in highly myopic individuals with larger optic discs.<sup>20</sup> Structural changes observed in the posterior segment with myopia include thinner subfoveal choroidal thickness,<sup>21, 22</sup> larger disc area,<sup>23</sup> thinner lamina cribrosa,<sup>24</sup> and morphological changes at and around the optic nerve head.<sup>25</sup> These structural changes at and around the optic nerve head in myopia and high myopia might be contributing factors for increased risk of glaucoma in myopic eyes.<sup>25</sup>

### ***1.3 Guinea Pig as a model of myopia***

The guinea pig, a common household pet, is a popular animal model of myopia.<sup>26-28</sup> Although originally classified as a rodent, phylogenetic analysis using amino acid sequence indicated that the guinea pig has an ordinal status separate from the Rodentia by an early evolutionary divergence.<sup>29</sup> Guinea pigs are a precocial species with a well-developed visual system at birth, showing both structural and functional retinal maturity prior to birth.<sup>30-32</sup> They

are a diurnal species, unlike rats and mice, and possess dichromatic vision with two types of cone system having peak spectral sensitivities similar to those of primate retina.<sup>33</sup> Guinea pigs respond to form deprivation and show rapid ocular development.<sup>26</sup> Other benefits of the guinea pig include easy breeding, rapid growth with developmental maturation at the age of 5 months, docile temperament, and wide availability.<sup>34</sup>

#### ***1.4 Potential role of guinea pig as a model of optic neuropathy and glaucoma***

Guinea pigs show some remarkable resemblances in ocular structure and function with the primate. The guinea pig retina shows a pattern of histogenesis and organization very similar to primate retina.<sup>31, 35</sup> Functionally, light adapted electroretinogram (ERG) responses from guinea pig retina are very similar to those from primate retina. Previous studies have assessed retinal function in guinea pigs using full field photopic flash ERG.<sup>36, 37</sup> One study investigated the photopic ERG responses in albino guinea pigs (n=19), and compared the responses with those of human, rat, and mouse.<sup>37</sup> The authors concluded that the guinea pig represented a superior rodent model of the human photopic ERG for the following reasons. Guinea pigs demonstrate similar morphology and time course of the photopic ERG and oscillatory potentials (OPs) responses as in humans. They show inhibitory type photopic ERG responses similar to diurnal species like primates, unlike the excitatory type photopic ERGs as seen in nocturnal species like rodents.<sup>36, 37</sup> Furthermore, responses of guinea pig photopic ERGs to intravitreal injections of blockers of the ON and OFF retinal pathways are similar to those from human eyes with retinopathies known to have anomalies of those pathways.<sup>37</sup>

Another striking feature in guinea pigs that resembles primate retina is the presence of collagenous lamina cribrosa.<sup>38, 39</sup> The lamina cribrosa is a sieve-like three dimensional porous structure within the optic nerve head that bridges the scleral canal, through which retinal

ganglion cell axons exit the eye.<sup>40</sup> In humans, the lamina cribrosa is made of a collagenous meshwork. The lamina cribrosa is suggested to be the primary site of damage in glaucoma, where local blockage of axonal transport occurs.<sup>41-43</sup> Although rodents such as rats and mice are frequently used in glaucoma studies, they do not possess a collagenous lamina cribrosa. The lamina cribrosa is completely absent in mice, whereas in rats, although lamina like structure is present, it is not a well-defined structure and consists of merely of thin fragments of the connective tissue in cross section which are associated with blood vessels lined with astrocytes.<sup>44-46</sup> In guinea pigs, the lamina cribrosa is multilayered and consists of distinct collagen layers, with collagen types I, III, IV and V.<sup>38, 46</sup> In non-human primates and humans, these collagen layers are made up of collagen beams, which are surrounded by glial cells that form channels supporting the bundles of nerve fibers traversing the lamina cribrosa. In guinea pigs, similar arrangement of the collagen beams and glial tissue is observed.<sup>38</sup> Furthermore, the pial septa in the optic nerve head of guinea pigs separates the optic nerve fibers into bundles.<sup>38, 44</sup> These similarities of guinea pig optic nerve head and lamina cribrosa structure suggest that guinea pig could be a viable alternative to study glaucomatous optic nerve damage.

### ***1.5 Retinal structural assessment in myopia and glaucoma***

The changes that occur in the retina and optic nerve head with myopia can be assessed using *in vivo* and *in vitro* techniques. With advanced imaging techniques such as the optical coherence tomography (OCT), it has become possible to evaluate the retinal and optic nerve head structures *in vivo*, thus allowing for longitudinal assessment of these structures in conditions such as myopia and glaucoma. Since first demonstrated by Huang et al.,<sup>47</sup> OCT imaging has advanced further from time domain to spectral domain OCT, thereby reducing the imaging time greatly. Additionally, with swept source OCT, it is now possible to image the

deeper layers such as the posterior sclera and posterior lamina cribrosa surface *in vivo*, which has made evaluation of these deeper structures much easier. OCT imaging has allowed for *in vivo* assessment of structural changes in these conditions without the need to sacrifice a large number of animals. Using OCT imaging, previous studies have reported important changes in the retina and optic nerve head in myopia, such as retinal nerve fiber layer thinning and redistribution of retinal thickness,<sup>48, 49</sup> lamina cribrosa surface changes such as thinning and tilting,<sup>24, 50, 51</sup> choroidal thinning<sup>21, 52</sup> and optic nerve head enlargement.<sup>53, 54</sup> Similarly, OCT has proved to be a valuable tool to aid in the diagnosis and management of glaucoma. Changes such as retinal nerve fiber layer thinning, optic nerve head changes such as decreased minimum rim width and lamina cribrosa surface depth changes have been reported in glaucoma using OCT imaging.<sup>55-60</sup> OCT imaging is often used in animal models, including in rodents, to assess retinal structure in various ocular conditions. For example, in rodent models of optic nerve crush and glaucoma, thinning of retina has been demonstrated with OCT imaging.<sup>61-63</sup> However, retinal and optic nerve head structure has not been fully described in guinea pigs using OCT imaging.

### ***1.6 Visual function assessment in myopia and glaucoma***

In rodents, visual function in conditions such as myopia and glaucoma is often assessed with non-invasive *in vivo* techniques such as ERG and behavioral measures of spatial frequency discrimination. The ERG response represents the extracellular potential arising from currents flowing through the retina as a result of neuronal signaling, and can be used to assess retinal electrical function of living intact retina. Full field flash ERG consists of exposing the eye to flashes of light, and recording waveforms of the different components through an electrode on the cornea. The major light adapted flash ERG components consist of the a-wave, b-wave, and photopic negative response (Figure 1-1 A). In the mammalian retina, the a-wave has been

shown to represent the activity of photoreceptors, and the b-wave primarily represents activity of bipolar cells.<sup>64-66</sup> An additional component of the ERG, the oscillatory potentials, are high frequency waves on top of b- wave and are thought to represent the inner retinal function in humans.<sup>67, 68</sup> Similarly, the PhNR has been shown to represent retinal ganglion cell activity in non-human primates, humans, and rodents.<sup>69-72</sup> Another type of ERG used to primarily assess retinal ganglion cell function is the pattern ERG. First described by Riggs, et al. in 1964,<sup>73</sup> the pattern ERG response represents the retinal bio-potential evoked by a temporally modulated patterned stimulus (checkerboard or grating) of a constant mean luminance, but varying local luminance. The major components of the pattern ERG are the initial negative going component (N1), the first positive component (P1) and the second negative component (N2) (Figure 1-1 B). In rodents and primates, P1 and N2 have been shown to receive contributions from retinal ganglion cells.<sup>74, 75</sup>

There is lack of literature regarding retinal function assessment with ERG in guinea pigs. Although some previous studies have demonstrated that photopic full field flash ERG responses in guinea pigs are very similar to humans,<sup>36, 37</sup> no study has till date evaluated the presence of PhNR in guinea pigs. Similarly, no study has reported pattern ERG responses in guinea pigs.

Another method of assessing visual function behaviorally in rodents is spatial frequency discrimination with optokinetic and optomotor responses. Optokinetic responses represent the reflexive eye movements that occur when following vertical gratings moving in the visual field in either the clockwise or the counter clockwise direction. These movements reduce and stabilize the movement of an image across the retina in a compensatory fashion.<sup>76</sup> Instead of just moving the eyes with the head still, some animals rotate the head in the direction of rotation

of stimulus, which represents an optomotor response.<sup>77</sup> In mice and rats, spatial frequency discrimination can be assessed rapidly with optokinetic and optomotor responses using optokinetic drum (figure 1-2).<sup>78, 79</sup> This method employs the use of a drum lined on the inside with square wave gratings of different spatial frequencies. The drum is rotated about a stationary platform at the center. The rodent is placed on the platform, and as the drum rotates, the optomotor response is observed to assess the spatial frequency discrimination. Such behavioral measure of vision has not been well established in guinea pigs.

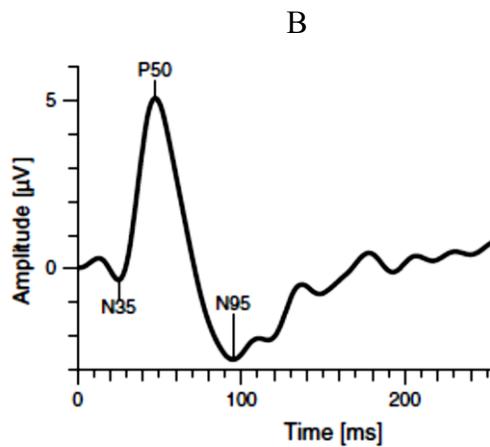
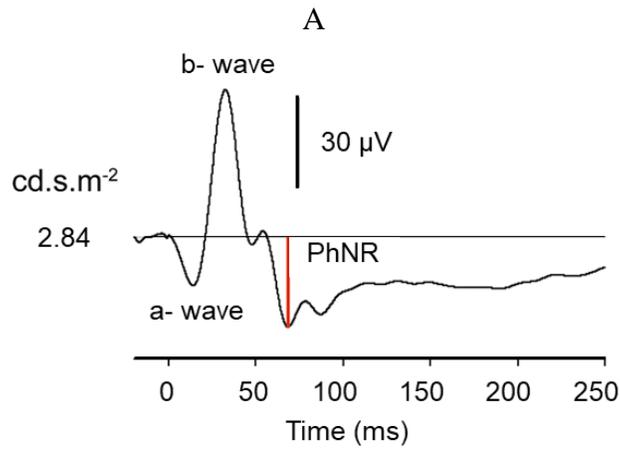


**Figure 1-1:** Representative traces of light adapted flash ERG responses

A) Representative trace of a light adapted flash ERG response from human retina with the a-wave, b-wave, and photopic negative response (PhNR) indicated, from Frishman, et al., 2018;<sup>80</sup>  
 B) Representative transient pattern ERG response from human retina for a stimulus of 0.8 cycles per degree, with the initial negative component N35, first positive component P50, and second negative component (N95) indicated, from Bach, et al., 2013<sup>81</sup>

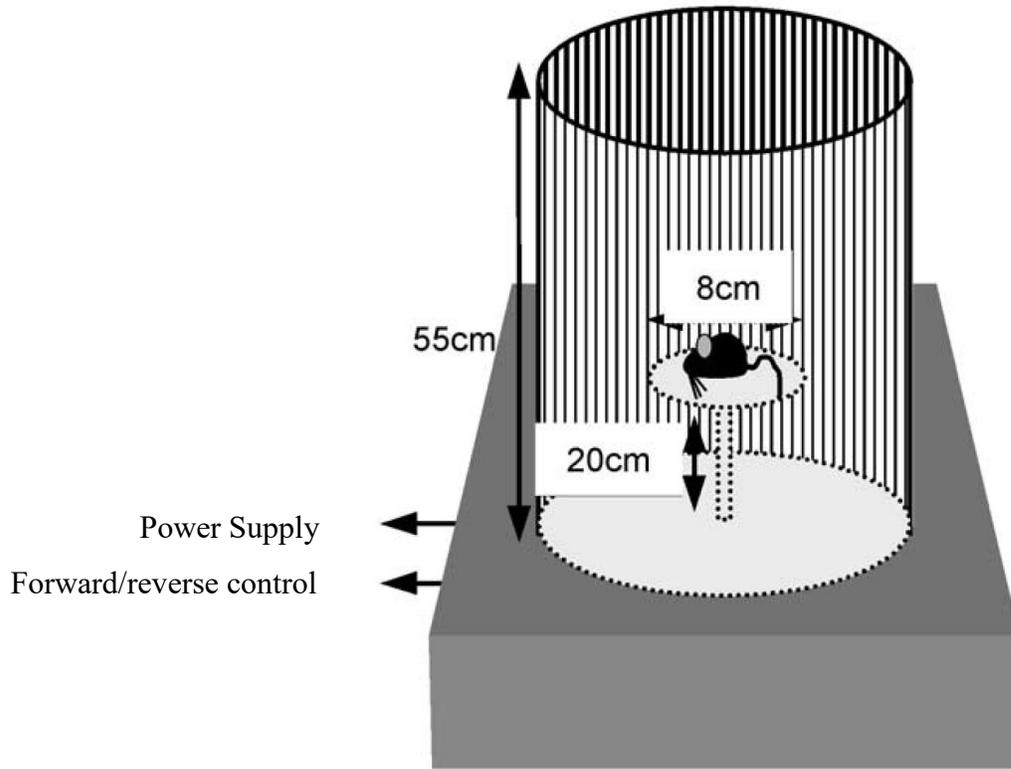


**Figure 1-2:** Schematic diagram of an optokinetic drum setup

A schematic diagram of optokinetic drum setup for assessing spatial frequency discrimination in rats (not to scale), from Thuang, et al., 2002<sup>78</sup>

### ***1.7 Purpose of studies in guinea pigs and in children***

Because of the similarities in retinal and optic nerve head structure and visual function between guinea pigs and primates, as described above, the guinea pig is a viable animal model to study glaucomatous optic neuropathy and susceptibility of glaucoma in myopic eyes. As guinea pigs are an existing animal model of myopia, they can be used to evaluate the hypothesis that the higher than normal prevalence of glaucoma in myopic eyes is secondary to changes in ocular structure and function resulting from myopic eye growth. As a first step, it is important to further understand retinal structure and function in normal guinea pigs. While this has been explored in other rodent models, such as rats and mice, in great detail, the same is lacking in guinea pigs. For example, it is known that retinal ganglion cells contribute to the photopic negative response and pattern ERG components in mice, rats, non-human primates, and humans; however, this is unknown in guinea pigs. Similarly, in order to assess changes with experimental manipulations such as glaucoma and myopia, normal retinal and optic nerve head structure should be characterized in detail in healthy guinea pigs. Furthermore, the retinal source of origin of the flash and pattern electroretinogram components should be determined in guinea pigs, so that these components can be used to assess the dysfunction of the related retinal structures in pathological conditions including myopia and glaucoma. To this end, as part of my dissertation, I investigated whether guinea pig inner retinal function can be quantified using flash and pattern electroretinogram and whether the components seen in other rodents and primates are present in this species. I also investigated whether the limits of spatial frequency discrimination in guinea pigs could be assessed with optomotor responses and further investigated the location of visual streak in the guinea pig retina. With the structural studies, I aimed to investigate whether repeatable measures of retinal and optic nerve head structure can

be obtained with *in vivo* imaging in guinea pigs and whether the measurements would be comparable to *in vitro* measures. I further investigated whether retrograde degeneration of retinal ganglion cells can be achieved in guinea pigs with optic nerve crush induced optic neuropathy, and whether we could assess retinal structural and functional changes with retinal ganglion cell degeneration in guinea pigs longitudinally using non-invasive techniques. I aimed to determine the contribution of retinal ganglion cells towards the flash and pattern ERG responses, and compare the functional and structural changes in terms of detection of retinal ganglion cell dysfunction and loss.

It is known in the literature that significant growth and remodeling of ocular structure occurs in children during the process of emmetropization and myopia development.<sup>82-84</sup> As the global burden of myopia is increasing,<sup>2,85</sup> along with the associated ocular complications, there is increasing interest to better understand the underlying mechanisms and changes in ocular structure with myopia. A large number of population based studies have suggested myopia associated changes in ocular structure, mostly in adult population.<sup>9, 11, 86</sup> I am interested in evaluating whether such myopia related ocular changes reported in adult population can be detected early on in school age children, which is the age when myopia development and progression begins.

The information gained from this research will be helpful in assessing retinal structural and functional changes in guinea pig model of myopia, optic neuropathy, and glaucoma. Guinea pigs could be the first animal model to undergo both myopia and glaucoma so that the susceptibility to glaucoma in myopic eyes can be further investigated.

## ***1.7 Overall methodology***

### **Guinea Pig Experiments**

**Subjects:** Experiments for chapters 2, 3, and 4 were carried out in pigmented guinea pigs (Elm Hill breed). For chapters 2 and 3, normal guinea pigs without any experimental manipulation to the eyes were used. Chapter 4 required guinea pig model of ganglion cell degeneration, which was achieved with the retrobulbar optic nerve crush method described in chapter 4.

**Surgical preparations:** For chapter 4, animals underwent a unilateral optic nerve crush procedure in right eyes, and left eyes served as controls. Optic nerve was exposed by blunt dissection of the sub-Tenon's space and the nerve was grasped with blunt curved forceps under direct visualization, 2-3 mm behind the globe, and pressure was manually applied for approximately 10 seconds. Care was taken not to cause injury to the surrounding vasculature. Immediate dilation of the pupil and loss of the pupillary light reflex was used as confirmation of a successful procedure.

**Data Acquisition:** Electrophysiological recordings were obtained from anesthetized animals with stimulators (Celeris, Diagnosys, LLC, MA) placed in touch with the cornea. ERG data were processed and analyzed with Replay program in MATLAB. For *in vivo* imaging in guinea pigs, images were collected with spectral domain optical coherence tomography (SD-OCT, Spectralis HRA+OCT; Heidelberg Engineering, Heidelberg, Germany). OCT images were analyzed with custom written program in MATLAB. Spatial frequency discrimination was assessed behaviorally with custom made optokinetic drum, lined on the inside with square wave gratings printed on photographic plates, calibrated for the drum. Retinal whole mounts were imaged with DeltaVision wide field deconvolution fluorescence microscope (GE Life Sciences,

Pittsburgh, PA) at 20X magnification. Ganglion cell quantification was done with ImageJ. Histological sections were imaged with a light microscope (DM1000, Leica, Germany).

Human subjects: For chapter 5, school age children were recruited mainly from the clinical facility at the University of Houston College of Optometry. Additional subjects were recruited from outside the college.

Data Acquisition: *In vivo* imaging was performed on both eyes of each subject with spectral domain optical coherence tomography (SD-OCT, Spectralis HRA+OCT; Heidelberg Engineering, Heidelberg, Germany). Scan protocol included three scans of each eye; 1) a 48-line radial scan (20°, 1024 A-scans per B-scan, Figure 1A), 2) a 12° peripapillary circular scan (1536 A-scans, Figure 1B) centered at the optic nerve head, and 3) a 97-line macular volume scan (20° x 20°, 1024 A-scans per B-scan, Figure 1C). Enhanced depth imaging mode was used for radial scans to better visualize deeper structures, including the peripapillary choroid and lamina cribrosa surface.

### ***1.8 Overview of dissertation chapters***

Chapter 1 is an introduction of the concepts critical for this dissertation, providing background on questions, including, “What is myopia?” “What are the retinal structural changes associated with myopia?” “What is the association between myopia and glaucoma?” and “How can guinea pigs be used for as a model to study retinal structural and functional changes in optic neuropathy, glaucoma and myopia?”

Chapter 2 is a manuscript titled, “Visual function in guinea pigs with electrophysiological and behavioral methods.” To develop the guinea pig model of optic neuropathy and glaucoma to study associations between myopia and glaucoma, it is important to develop methods to assess visual function non-invasively in this species so that retinal

functional changes with any ocular condition could be followed longitudinally. This chapter describes non-invasive method of electrophysiology to evaluate retinal function and describes components of electroretinogram in guinea pigs shown to be related to retinal ganglion cells in other mammalian species. This chapter also describes a method to assess behavioral visual function in guinea pigs, and describes the topographical distribution of retinal ganglion cells in this species.

Chapter 3 is a published manuscript titled, “*In vivo* imaging of the retina, choroid, and optic nerve head in guinea pigs.” This chapter describes the non-invasive *in vivo* imaging of retinal structure in guinea pigs with optical coherence tomography imaging, assesses repeatability of the measurements and compares *in vivo* measures with histological measures.

Chapter 4 is a manuscript titled, “Retinal structure and function with ganglion cell ablation in the guinea pig.” This chapter explores the retinal structural and functional changes with optic nerve crush in guinea pigs, using imaging and visual function assessment techniques described in chapters 2 and 3. Chapter 4 further describes the contribution of retinal ganglion cells to the different components of flash and pattern ERGs in guinea pigs.

Chapter 5 is a submitted manuscript titled, “Optic nerve head and lamina cribrosa in non-myopic and myopic children.” This chapter describes the retinal and optic nerve head structures in relation to age, axial length, and refraction in school age children, also using imaging and analysis techniques described in chapter 3. Although this chapter is a bit of a departure from previous chapters looking at retinal structure and function in guinea pigs, the imaging analysis techniques developed for chapter 2 were directly applied in this study.

Chapter 6 contains an overall discussion of all the experiments in this dissertation. In this chapter, I summarize 1) the components of ERGs, their retinal origin, and their application

in studies of optic neuropathy and myopia, 2) the significance of evaluating retinal structure and function non-invasively in guinea pigs with induced retrograde degeneration of retinal ganglion cells and potential applications of this model for further studies of glaucoma and myopia, 3) the significance of evaluating retinal and optic nerve head structure in school age children as a function of age, axial length and refraction, and 4) an overview of my future research directions in vision science.

## **CHAPTER 2: EVALUATION OF VISUAL FUNCTION IN GUINEA PIG WITH BEHAVIORAL AND ELECTROPHYSIOLOGICAL METHODS**

Ashutosh Jnawali, Laura J Frishman, Lisa A Ostrin

### ***2.1 Introduction***

Guinea pigs are an important model of human ocular conditions, and are commonly used as a model of eye growth and myopia.<sup>26-28, 87, 88</sup> Guinea pigs are precocial animals with a well-developed visual system at birth, showing both structural and functional retinal maturity.<sup>30-32</sup> Unlike rats and mice, which are nocturnal, guinea pigs are crepuscular (i.e. most active at dawn and dusk). They have dichromatic vision with two types of cones, short and medium wavelength sensitive, having peak spectral sensitivities similar to those of primate retina.<sup>33</sup> Benefits of the guinea pig model include easy breeding, developmental maturation at the age of five months, docile temperament, and wide availability.<sup>34</sup> Several strains of guinea pigs have been shown to develop form deprivation and lens induced myopia.<sup>26, 88-91</sup> However, guinea pig visual function has not been fully characterized.

In rodents, spatial frequency discrimination can be assessed rapidly using an optomotor paradigm.<sup>78, 79, 92</sup> An optomotor paradigm utilizes reflexive movements of the head or body that occur when the environment is moving or drifting across the retina.<sup>77</sup> Optomotor responses function to stabilize the image of the moving object on the retina.<sup>76, 77, 93</sup> To examine optomotor responses, the animal is placed on a stationary platform at the center of a drum that is rotated in either direction (clockwise or counterclockwise), and the animal is observed for tracking movements of the body or head.<sup>92, 94</sup> This technique is simple, rapid, and non-invasive.<sup>94</sup> Using this method, mice and rats have been shown to have a spatial frequency discrimination of

approximately 0.4 and 0.6 cycles per degree, respectively.<sup>94, 95</sup> Interestingly, under monocular conditions, an optokinetic response in mice and rats is elicited only when the stimulus is rotating in the temporal to nasal direction. The lack of a response to stimuli rotating in the nasal to temporal direction is attributed to having only crossed subcortical projections from the eyes,<sup>95, 96</sup> and may be an evolutionary adaptation for lower mammals of prey. In higher mammals, such as felines and primates, monocular optokinetic responses have been shown to be similar to either direction of motion.<sup>97, 98</sup> Such behavioral measures of vision have not been well established in guinea pigs. One previous study utilized optomotor responses to evaluate head tracking gain (the ratio of angular head speed to drum speed) in guinea pigs of different ages and with different refractive states.<sup>99</sup> However, the limits of grating acuity and potential differences with monocular viewing were not reported.

Electroretinography is a non-invasive objective assessment of retinal function, which is useful in investigating the progression of disease. The full field photopic flash electroretinogram (ERG) elicits a retinal response with components representing inner and outer cell types.<sup>36, 37</sup> Researchers have investigated the photopic ERG responses in guinea pigs, and compared the responses with those of human, rat, and mouse.<sup>36, 37</sup> The guinea pig ERG waveforms were found to be more similar than other rodents to the primate photopic ERG.<sup>37</sup> Additionally, the intensity response function for oscillatory potentials in the photopic ERG responses from humans and guinea pigs have been shown to be comparable.<sup>37</sup> Furthermore, responses of guinea pig photopic ERGs to intravitreal injections of blockers of the ON and OFF retinal pathways were similar to those from human eyes with retinopathies known to have anomalies of those pathways.<sup>37</sup> The a-wave component in guinea pigs has been shown to include contributions from second order neurons, hyperpolarizing bipolar cells and horizontal cells, and exhibit a strong negative-going

off-response, similar to that seen in monkeys.<sup>36</sup> Another component of photopic ERG in the mammalian retina is the photopic negative response (PhNR), which is known to be related to retinal ganglion cells in mice and primates.<sup>69-71</sup> However, this component has not yet been reported in guinea pigs. Characterization of the PhNR response in guinea pigs would be useful to study the integrity of inner retina in pathological conditions such as glaucoma.

The pattern ERG is a retinal bio-potential evoked by temporally modulated patterned stimulus,<sup>81</sup> and has been shown to arise primarily from the retinal ganglion cells in mammalian retina in species such as cats,<sup>100</sup> mice,<sup>74</sup> rats,<sup>101</sup> non-human primates,<sup>102</sup> and humans.<sup>103</sup> On the other hand, retinal ganglion cells have been shown to not contribute to the avian pattern ERG.<sup>104-106</sup> In mammals, the pattern ERG has been used as a tool to investigate retinal ganglion cell dysfunction in conditions such as glaucoma.<sup>107</sup> No study has yet reported pattern ERG responses in guinea pigs.

Retinal ganglion cell distribution and density can be used to predict potential spatial frequency discrimination. A region of high density retinal ganglion cells indicates the presence of a fovea or visual streak. Rats and mice do not have a fovea or a well-defined visual streak,<sup>108, 109</sup> while rabbits have been shown to possess a visual streak in the retina below the optic nerve head.<sup>110</sup> Guinea pigs have been shown to possess a visual streak; however, the location and cell density are conflicting between studies.<sup>111, 112</sup>

The goals of this study were to investigate spatial frequency discrimination using optomotor responses, to characterize the pattern ERG and PhNR responses, and to describe retinal ganglion cell density distribution histologically in adult guinea pigs. These findings will help to further establish the guinea pig as a model of human ocular function and disease.

## **2.3 Methods**

### 2.3.1 Animals

Six healthy adult female pigmented guinea pigs (Elm Hill Labs, MA, USA), aged 2.5 years, were included in this study. Animals were kept under a 12 hour light/dark cycle and provided food and water *ad libitum*. Procedures were approved by the Institutional Animal Care and Use Committee at the University of Houston and conformed to the ARVO statement for the Use of Animals in Ophthalmic and Vision Research.

### 2.3.2 Optomotor responses

Visual performance was assessed behaviorally using a custom optomotor instrument. The setup consisted of a motorized cylindrical drum of 55 cm diameter with a stationary platform at the center. Square wave gratings for spatial frequencies from 0.3 to 2.4 cycles per degree (cpd) in steps of 0.3 cpd, were printed on photographic papers and used to line the inside of the drum. The gratings were calibrated for spatial frequencies at the center of the drum. Awake animals were placed on the central stationary platform in a plastic beaker (Figure 2-1). The drum was rotated at a constant speed of 12 degrees per second in both clockwise and counterclockwise directions. The speed of rotation was selected based on the literature where similar setup was used to assess head tracking responses in rats and mice.<sup>78, 79</sup> The tracking response of the animals to the rotating stimulus was evaluated by observing head rotation. The test was repeated at least three times for each direction of rotation and for each spatial frequency. Eyes were tested both monocularly and binocularly. For monocular testing, one eye was occluded using a black piece of cloth. The maximum spatial frequency that elicited observable tracking response in both directions was noted for each animal for both monocular and binocular viewing conditions.

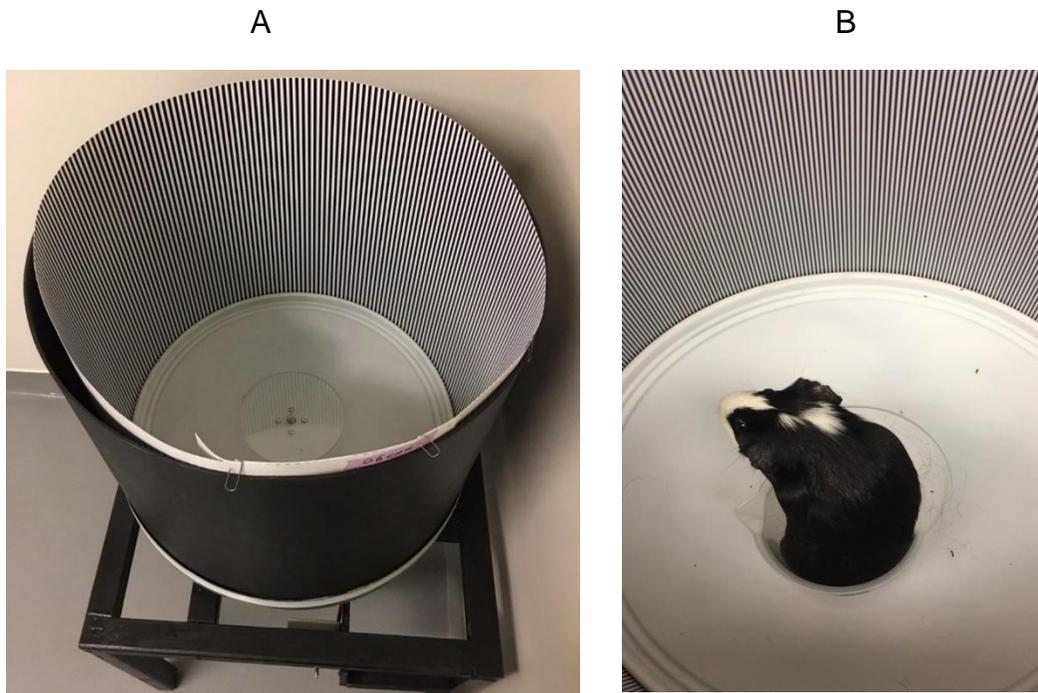


**Figure 2-1:** Behavioral assessment of spatial frequency discrimination in guinea pigs

A) custom optomotor instrument B) guinea pig on stationary platform in the instrument

### 2.3.3 Electroretinography

For electroretinography (ERG), animals were anesthetized with ketamine (30 mg/kg, VEDCO Inc, MO, USA) and xylazine (3 mg/kg, Lloyd Laboratories, Philippines); anesthesia was maintained with a 50% dose every 40 minutes, as needed, via a subcutaneous needle fixed in the back. ERG responses were obtained under light adapted conditions. Pattern ERGs were recorded from each eye, followed by flash ERGs. For pattern ERG, the stimulator probe (Celeris, Diagnosys, LLC, MA) was placed in contact with the cornea, aligned with the center of the pupil, and the reference electrode was placed on the fellow eye. Artificial tears (Refresh Liquigel, Allergan) were applied on both eyes to maintain corneal hydration. A ground electrode was inserted under the skin on the fore limb. The probe uses a pinhole aperture. The built-in heating function of the instrument's stage was used to maintain the body temperature at 37°C. Stimuli consisted of square wave gratings of frequencies ranging from 0.025 to 0.25 cycles per degree at 100% contrast, modulated at a temporal frequency of 1.05 Hz. 1800 responses were averaged for each eye. For flash ERG, stimulator probes were placed in contact with each cornea, aligned with the center of the pupil, and responses were collected from both eyes simultaneously. Flash intensity of 10.0 cd.s/m<sup>2</sup> with background intensity of 9.0 cd.s/m<sup>2</sup> was used; this intensity was previously shown to elicit ERG b-waves of near maximal amplitude in the guinea pig.<sup>37</sup> Responses from 10 flashes were averaged for each eye. To assess repeatability, ERG responses were recorded from six animals on two occasions, separated by at least a week.

ERG responses were analyzed in a custom written program in MATLAB (The MathWorks, Inc., Natick, MA, USA). For flash ERGs, a-wave amplitudes were measured from baseline to the a-wave trough on the raw trace. For b-wave and PhNR measurement, a band pass filter of 1-50 Hz was applied to the raw trace. The amplitude of b-wave was measured from a-wave trough to the

b-wave peak. The PhNR was measured from baseline to the trough immediately following the b-wave. For pattern ERG recordings, drift correction and band pass filter of 1-100 Hz were applied to the raw traces. The first negative trough (N1), the first positive peak (P1), and the second negative trough (N2) were identified, the amplitudes and implicit times were measured for each waveform, as well as for the N1P1 and P1N2 components.

#### 2.3.4 Ganglion cell quantification

Animals (n = 4) were euthanized with 100 mg/kg sodium pentobarbital (Fatal-Plus or Euthasol, Vortech Pharmaceuticals, MI, USA), and one eye each was marked for orientation, enucleated, and placed in phosphate buffered saline (PBS) solution. Eyes were fixed in 4% paraformaldehyde for two hours, orientation cuts were made, and the tissue was washed with PBS and PBS with tritonX. The whole eyecups with orientation cuts were then immersed in blocking buffer solution for at least an hour, and transferred to rounded bottomed tubes containing primary antibody, alpha-RBPMS (retinol binding protein with multiple splicing) rabbit antibody (Ab) (Abcam, Cambridge, MA, USA), a specific marker for retinal ganglion cells, at 1:500 dilution. The eyecups were kept on rotator at 4°C for five days. On the sixth day, eyes were washed with PBS and PBS with tritonX, and vitreous was removed under a light microscope (DM1000, Leica, Germany). Eyecups were labeled with secondary antibody, goat anti-rabbit alexa fluor 488 (ThermoFisher Scientific, Grand Island, NY, USA) at 1:250 dilution for two hours followed by a PBS with tritonX wash. Under low illumination, retina was isolated from the retinal pigment epithelium and choroid and mounted on glass slides using cyto seal mounting medium (Cytoseal 60, Richard-Allan). The slides were incubated in the dark overnight and imaged on DeltaVision wide field deconvolution fluorescence microscope (GE Life Sciences, Pittsburg, PA) at 20X magnification the following day.

Images were collected as panels for the retinal flat mounts under 20X. The panels were stitched together for the composite image, and saved as jpeg images (Figure 2-2 A). The images were then imported in Fiji (ImageJ, NIH, Bethesda, MD, USA).<sup>113</sup> Grids with boxes of size 250 x 250  $\mu\text{m}^2$  were overlaid over the entire retinal flat mount image. Retinal ganglion cells were counted on every third box manually with cell counter in Fiji (Figure 2-2 B). Counts were converted to ganglion cell density in cells/ $\text{mm}^2$ .

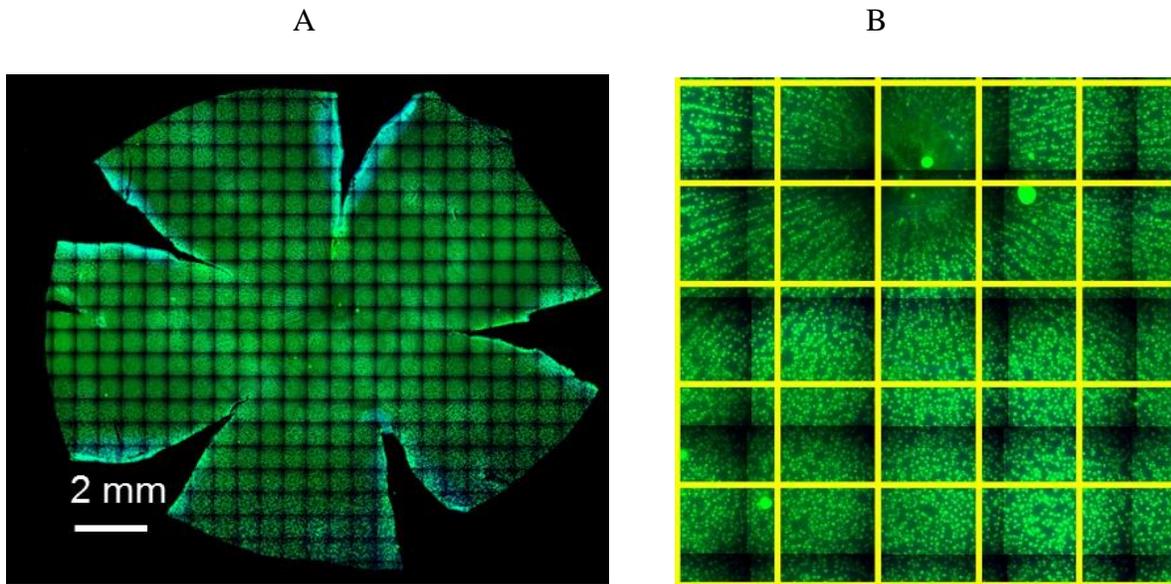


**Figure 2-2:** Representative images on ganglion cell counting

A) Representative stitched image of guinea pig retinal whole mount (green labels represent retinal ganglion cells) and B) magnified image of central retina from the retinal whole mount; each yellow box is  $250 \times 250 \mu\text{m}^2$

### 2.3.5 Statistical Analysis

Statistical analysis was performed using MedCalc<sup>®</sup> statistical software version 18 (MedCalc Software, Belgium). Data are expressed as mean  $\pm$  standard deviation. Normality of data was assessed with Saphiro-Wilk test. The repeatability of ERG amplitudes was assessed with coefficient of variation.

## **2.4 Results**

### 2.4.1 Optomotor responses

Results for behavioral assessment of vision using an optomotor paradigm are shown in Figure 2-3. With binocular viewing, the mean maximum spatial frequency to elicit a tracking response was  $1.65 \pm 0.49$  cpd, which was the same as that obtained with monocular viewing when the stimulus rotated in the temporal to nasal direction. However, when the stimulus rotated in the nasal to temporal direction under monocular viewing, the mean maximum spatial frequency to elicit tracking decreased  $0.75 \pm 0.16$  cpd, demonstrating a directional selectivity for stimuli rotating towards the midline.

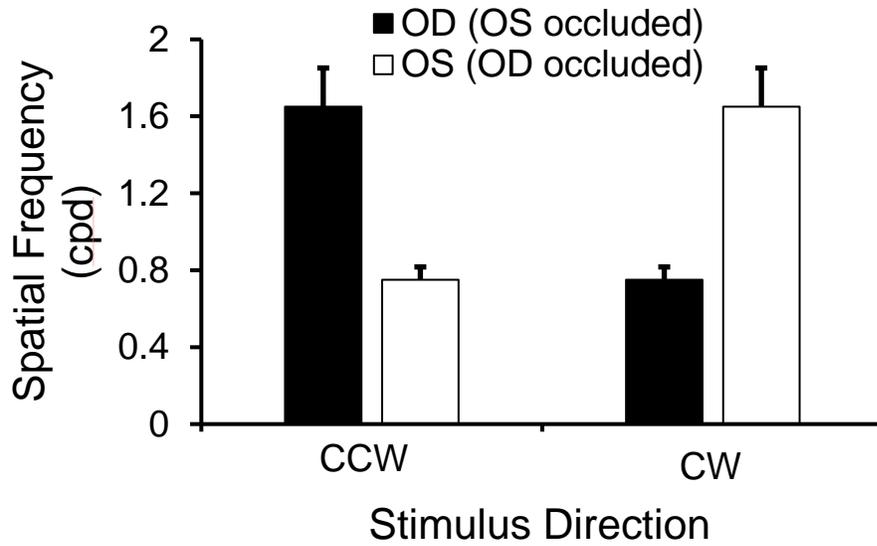


**Figure 2-3:** Spatial frequency sensitivity in adult guinea pigs

Monocular optomotor spatial frequency sensitivity in cycles per degree (cpd) for clockwise (CW) and counterclockwise (CCW) rotating gratings for adult guinea pigs (n = 6)

## 2.4.2 Electroretinography

Representative flash and pattern ERG traces are shown in Figure 2-4. Response amplitudes and implicit times for the a-wave, b-wave, and PhNR of the flash ERG are summarized in Table 2-1. Mean a-wave amplitude was  $19.24 \pm 4.24 \mu\text{V}$ , b-wave amplitude was  $33.58 \pm 8.22 \mu\text{V}$ , and the PhNR was  $24.0 \pm 5.72 \mu\text{V}$ . For repeat measures, the coefficient of variation with 95% confidence intervals for a-wave, b-wave, and PhNR amplitudes were 33.15% (0-47.50), 28.77% (0-42.06), and 21.06% (0-33.33), respectively.

Response amplitudes and implicit times for N1, P1, N2, N1P1 and P1N2 of the pattern ERG are summarized in Table 2-2. The N1P1 component reached a maximum amplitude of  $3.50 \pm 1.16 \mu\text{V}$  at the lowest spatial frequency tested (0.025 cpd, Figure 2-5 A). The amplitude reduced by almost half for the next spatial frequency of 0.05 cpd ( $1.65 \pm 0.97 \mu\text{V}$ ), and remained relatively stable at further higher spatial frequencies of 0.075, 0.1, and 0.125 cpd. The N1P1 amplitude to a 0.25 cpd stimulus further reduced to  $0.51 \pm 0.17 \mu\text{V}$ . For N2, the results were more variable, and a consistent negative trough below the baseline was not always present. Thus, the positive values for N2 amplitude represent the trough immediately following the P1 peak that did not cross the baseline. For this reason, P1N2 was used to describe the N2 responses following the P1 peak. The peak amplitude of P1N2 was obtained at 0.05 cpd spatial frequency, and responses for spatial frequencies either larger or smaller than 0.05 cpd were attenuated (Figure 2-5 B). The mean implicit time for P1 and N2 for the optimal stimulus of 0.05 cpd at 100% contrast were  $50.33 \pm 1.86 \text{ ms}$  and  $88.0 \pm 3.16 \text{ ms}$ , respectively. The coefficient of variation with 95% confidence intervals for N1P1 and P1N2 amplitudes were 24.42% (0-36.48) and 39.15% (0-58.58) respectively.

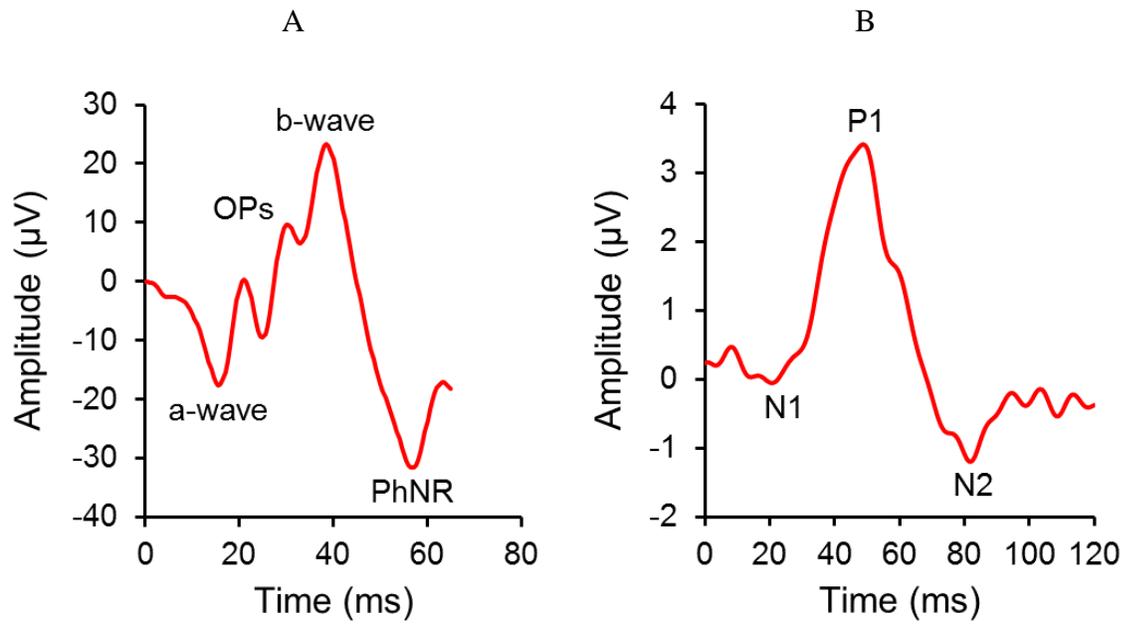


**Figure 2-4:** Representative raw traces for flash and pattern electroretinogram

A) a full field flash ERG elicited with a  $10.0 \text{ cd.s/m}^2$  stimulus and B) a pattern ERG elicited with a 0.05 cycle per degree alternating square wave stimulus at 100% contrast

**Table 2-1:** Amplitude ( $\mu\text{V}$ ) and implicit times (ms) of the a-wave, b-wave, and photopic negative response (PhNR) of the full field flash ERG from adult guinea pigs ( $n = 6$ ) for flash strength of  $10.0 \text{ cd.s/m}^2$

	Amplitude ( $\mu\text{V}$ )	Implicit time (ms)
a-wave	$19.2 \pm 4.2$	$13.7 \pm 0.9$
b-wave	$33.6 \pm 8.2$	$32.3 \pm 2.3$
PhNR	$24.0 \pm 5.7$	$54.1 \pm 2.2$

**Table 2-2:** Amplitude ( $\mu\text{V}$ ) and implicit time (ms) for pattern ERG components from adult guinea pigs ( $n=6$ ) for alternating stimuli of spatial frequencies ranging from 0.025 to 0.25 cycles per degree; the first negative trough (N1), positive peak (P1), and second negative trough (N2), as well as the N1P1 and P1N2 components, are shown

Pattern ERG		Spatial frequency (cycles per degree)					
		0.025	0.05	0.075	0.1	0.125	0.25
N1	Amplitude	0.63 $\pm$ 0.47	-0.07 $\pm$ 0.20	-0.19 $\pm$ 0.33	-0.31 $\pm$ 0.38	-0.27 $\pm$ 0.26	0.16 $\pm$ 0.54
	Implicit time	27 $\pm$ 3.46	25.16 $\pm$ 1.83	26.83 $\pm$ 3.92	23.66 $\pm$ 4.27	25.83 $\pm$ 4.57	25 $\pm$ 10.53
P1	Amplitude	3.81 $\pm$ 1.13	1.90 $\pm$ 0.87	1.73 $\pm$ 0.86	1.75 $\pm$ 0.62	1.96 $\pm$ 0.91	0.51 $\pm$ 0.17
	Implicit time	54.5 $\pm$ 3.61	51.16 $\pm$ 3.60	53.5 $\pm$ 4.32	57.5 $\pm$ 5.08	55.5 $\pm$ 7.71	42.33 $\pm$ 10.50
N2	Amplitude	2.19 $\pm$ 2.61	-0.85 $\pm$ 1.07	-0.37 $\pm$ 0.87	1.18 $\pm$ 0.66	0.56 $\pm$ 0.61	-0.85 $\pm$ 0.36
	Implicit time	85 $\pm$ 6.57	83.33 $\pm$ 4.32	85.16 $\pm$ 3.54	86.66 $\pm$ 7.06	88.33 $\pm$ 3.66	79.83 $\pm$ 6.40
N1P1	Amplitude	3.50 $\pm$ 1.16	1.65 $\pm$ 0.97	1.87 $\pm$ 0.70	1.95 $\pm$ 0.56	2.00 $\pm$ 0.86	0.51 $\pm$ 0.17
P1N2	Amplitude	1.30 $\pm$ 1.45	2.49 $\pm$ 0.10	2.24 $\pm$ 0.16	0.76 $\pm$ 0.09	1.43 $\pm$ 0.25	1.36 $\pm$ 0.19

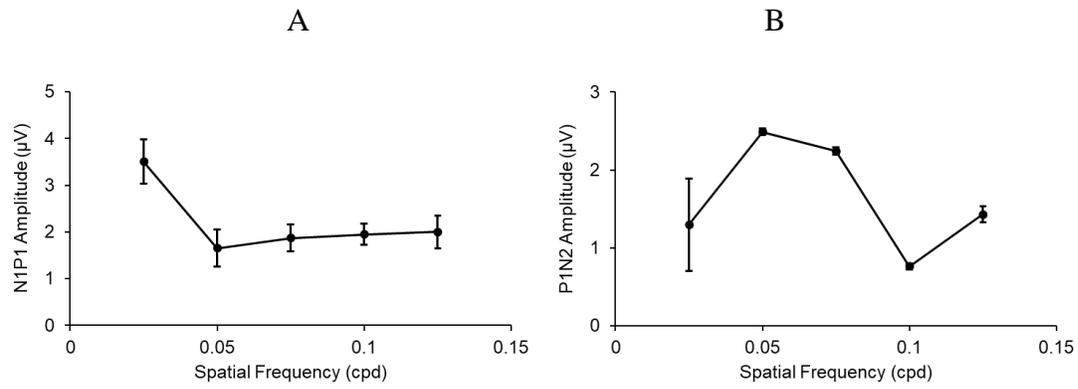


**Figure 2-5:** N1P1 and P1N2 amplitudes of pattern ERG for different spatial frequencies

A) N1P1 and B) P1N2 amplitudes of the pattern ERG for alternating stimuli of increasing spatial frequency from 0.025 to 0.125 cycles per degree (cpd) in adult guinea pigs (n = 6)

### 2.4.3 Ganglion cell quantification

A representative retinal ganglion cell density heat map from left eye of one guinea pig is shown in Figure 2-6. The mean peak retinal ganglion cell density for all eyes was  $1621 \pm 129$  cells/mm<sup>2</sup>. The peak density was located approximately 1-2 mm superior to the optic nerve head and extended laterally on either side towards the nasal and temporal retina, representing the visual streak. Density decreased progressively from the visual streak to the superior retina with the least density of 64 cells/mm<sup>2</sup> in the extreme periphery superiorly. Excluding the visual streak, a difference in the retinal ganglion cell density in the ventral and dorsal retina was observed, with greater density in the inferior retina compared to the superior retina. The maximum ganglion cell density in the inferior retina was  $1328 \pm 204$  cells/mm<sup>2</sup>.



## ***2.5 Discussion***

The main goals of this study were to describe visual function in guinea pigs using behavioral and electrophysiological measures. The spatial frequency sensitivity in adult guinea pigs was determined with optomotor responses. Partial directional selectivity was observed. The presence of a quantifiable and repeatable photopic negative response (PhNR) and pattern ERG responses was demonstrated. The location of visual streak was identified to be in the superior retina using a specific marker for retinal ganglion cells. Findings from this study will be important for future studies evaluating retinal functional changes in guinea pigs in conditions such as myopia, optic neuropathy, and glaucoma.

We utilized a custom optokinetic instrument to assess behavioral visual function in guinea pigs, and found a maximum spatial frequency discrimination of approximately 1.6 cycles per degree, determined by evaluating head tracking responses to drifting gratings in both clockwise and counterclockwise directions. Assessment of acuity in rodents using optomotor responses is a well-established technique. Cowey, et al. first demonstrated such tracking responses in rats to drifting gratings and found that tracking was lost in eyes with complete sectioning of optic nerve.<sup>79</sup> Similarly, Thaug et al. demonstrated that optomotor responses could be used to differentiate between mice with normal vision and those with severe retinal degeneration.<sup>78</sup> The maximum spatial frequency discrimination with gratings in wild type mice has been reported to be 0.5 cpd.<sup>114</sup> Prusky, et al, used a virtual optomotor system to demonstrate a maximum grating acuity of 0.4 cpd.<sup>94</sup> An interesting finding was that mice, as well as rats, were only able to track drifting stimuli when the gratings rotated from temporal to nasal visual field, and showed no tracking response when the gratings moved from nasal to temporal visual field.<sup>79, 95</sup> This directional selectivity may be due to insufficient ipsilateral projections from the eyes to the visual cortex.<sup>95</sup> In this study, we

also observed directional selectivity in guinea pigs. However, unlike in rats and mice, the directional selectivity in guinea pigs was not complete. Rather, the mean spatial frequency sensitivity measured with gratings drifting from nasal to temporal visual field for each eye was approximately half of the sensitivity for temporal to nasal rotation. This suggests that there might be sufficient ipsilateral projection from each eye to the visual cortex to allow spatial frequency discrimination in either direction.<sup>115</sup> While not complete directional selectivity as in other rodents, this partial directional selectivity allows the visual capabilities of each eye to be measured under binocular conditions by changing the direction of rotation.

The light adapted flash ERG showed that a- and b-wave amplitudes in guinea pigs were approximately 19  $\mu\text{V}$  and 34  $\mu\text{V}$ , respectively. Previous studies have reported amplitudes for a- and b-waves in albino guinea pigs to be approximately 40  $\mu\text{V}$  and 111  $\mu\text{V}$ , respectively.<sup>36, 37</sup> Vingrys et al. also reported larger ERG waveforms in albino guinea pigs compared to those found here.<sup>116</sup> While the stimulus strength used in all studies was similar, the earlier studies used albino guinea pigs, as opposed to pigmented guinea pigs. This difference, as well as differences in instruments and electrodes, may account for reported differences in amplitudes between studies. Amplitudes observed here are also much smaller than those from mice and humans,<sup>37, 74</sup> and more similar to those reported in rabbits,<sup>117</sup> which, like guinea pigs, possess an avascular retina. In addition to instrument related differences, difference in the amplitudes between species could be due to varying contribution of the different retinal neurons for each component. For example, the contribution of horizontal cells to the b-wave amplitude in mice and rats is known to be smaller than that in primates.<sup>65</sup>

The PhNR of the full field ERG is the immediate negative trough following the b-wave.<sup>69</sup> In non-human primates and humans, the PhNR has been shown to originate from retinal ganglion

cells.<sup>69, 70</sup> Previous studies evaluating the ERG in guinea pigs have not reported a PhNR.<sup>36, 37, 118,</sup>  
<sup>119</sup> We observed a consistent PhNR in guinea pigs, with an implicit time of approximately 54 ms, similar to that reported in non-human primates and humans.<sup>69, 70</sup> This similarity in relatively short time for the peak PhNR in guinea pigs and humans, compared to a longer time in mice of 150 ms,<sup>71</sup> raises the possibility that the retinal origin of this component in guinea pigs and humans might be similar, most likely originating from retinal ganglion cells and their axons. The presence of the PhNR in guinea pigs might provide a metric to assess inner retinal function, and therefore, future studies aimed at determining the origin of the PhNR in guinea pigs would be valuable.

Pattern ERG responses in guinea pigs have not been reported previously. We found that the pattern ERG waveforms were similar in shape to those from other mammalian species including mice, rats, non-human primates, and humans, with an initial negative trough (N1), positive peak (P1), and second negative trough (N2).<sup>81, 101, 120, 121</sup> In humans, these waveforms are referred to as N35, P50, and N95, respectively, with the numbers referring to the average time of peak for those components.<sup>81</sup> Here, a 0.025-0.05 cpd grating was the optimal stimulus size to elicit a maximum pattern ERG response. The amplitudes of the components P1 and P1N2 in guinea pigs were similar to those found in humans and non-human primates,<sup>81, 121</sup> as well as rabbits. However, amplitudes have been shown to be higher in mice and rats.<sup>122, 123</sup> Likewise, the mean implicit time for these components in guinea pigs were similar to humans, but were different from those in mice and rats.<sup>74, 121</sup> Thus, guinea pig pattern ERG responses are more comparable in amplitude and implicit times to humans and non-human primates than to mice and rats. In mice and monkeys, the retinal source of origin of pattern ERG has been determined to be retinal ganglion cells.<sup>74, 124</sup> The demonstration of the presence of pattern ERG in guinea pigs in this study and the similarities to

primates opens possibilities for further studies investigating the retinal origin of these waveforms and their implications in retinal disease.

We found a mean peak retinal ganglion cell density of approximately 1621 cells/mm<sup>2</sup> with the maximum of 1760 cells/mm<sup>2</sup> in one animal, which approaches the peak density reported by Rodriguez, et al (2064 cells/mm<sup>2</sup>), using a similar staining technique.<sup>125</sup> RBPMS (retinol binding protein with multiple splicing) antibody has been shown to be a highly specific marker for retinal ganglion cells in the mammalian retina including rats, mice, rabbit, macaque, and guinea pigs.<sup>125</sup> Do Nascimento et al. reported peak retinal ganglion cell density of 2272 cells/mm<sup>2</sup>.<sup>111</sup> However, they used Nissl stain for quantification of ganglion cells, which is a non-specific marker for nucleic acid and stains all nuclei. Since the retinal ganglion cell layer might contain a large proportion of displaced amacrine cells,<sup>111</sup> it is likely the retinal ganglion cell count obtained with non-specific labeling of cells with Nissl staining was confounded with amacrine cell population. Because of the use of markers not specific to retinal ganglion cells, authors relied on morphological clues such as cell body diameter, color of nucleus, and prominence of nucleolus to differentiate between ganglion cells and other neurons. On the other hand, Choudhury, et al. reported a peak retinal ganglion cell density of 720-864 cells/mm<sup>2</sup>.<sup>112</sup> This lower density could be due to not taking into account retinal ganglion cell with small cell bodies.<sup>111</sup> Both our study and that of Do Nascimento, et al, found that the visual streak was located in the superior retina above the optic nerve head, and, excluding the visual streak, the ganglion cell density increased in the inferior retina.<sup>111</sup> We speculate that the superior location of the visual streak aids the guinea pig in searching for food on the ground, while the high ganglion cell density in the inferior retina aids the guinea pig in viewing incoming predators, such as birds, in the superior field.

A peak retinal ganglion cell density of 1760 cells/mm<sup>2</sup> predicts a maximum spatial frequency discrimination of 2.07 cpd, with a calculated retinal magnification factor of 99 microns per degree, or 4.15 cells per degree (1760 cells/mm<sup>2</sup> = 42 cells/mm, retinal magnification factor = 0.099 mm/deg, sampling density = cells/mm x mm/deg = 42 x 0.099 = 4.15 cells/deg).<sup>111</sup> With optomotor responses, we found a mean spatial frequency discrimination of 1.64 cpd, and with pattern ERG, a response was elicited with a maximum spatial frequency grating of 0.5 cpd. It is not unexpected that maximum spatial frequency discrimination is less with functional measures than that predicted by maximum retinal ganglion cell density. The spatial frequency discrimination determined with optomotor tracking depends on properties of the retinal efferent pathways to subcortical structures. The nucleus of the optic tract and the dorsal terminal nucleus of the accessory optical system are involved in the optomotor tracking responses.<sup>76, 95</sup> The cells in the nucleus of the optic tract and the dorsal terminal nucleus have large receptive fields, thus yielding lower spatial frequency preference.<sup>95</sup> Similarly, detection of pattern ERG responses is dependent on several factors, including instrument specific variables and electrode sensitivity, and therefore, may result in lower spatial frequency discrimination than that predicted solely by retinal ganglion cell density.

## ***2.6 Conclusions***

This study characterized guinea pig visual function using behavioral and electrophysiological methods, and determined the location of visual streak in the guinea pig retina with markers selective to retinal ganglion cells. Findings suggest that spatial frequency discrimination can be rapidly assessed in guinea pigs using optomotor responses. Presence of a PhNR in the full field flash ERG and pattern ERG responses in guinea pigs, and the similarity of

these waveforms to those in primates, further supports the use of guinea pigs as a model of human ocular disease.

#### Acknowledgements

This study was funded by NIH NEI K08 EY022696 and NIH NEI P30 EY007551. The authors thank Alan Burns for help with Delta Vision imaging, Krista Beach and Sudan Puri for help with immunohistochemistry and John Bauer for help with constructing the custom optokinetic drum.

## CHAPTER 3: IN VIVO IMAGING OF THE RETINA, CHOROID AND OPTIC NERVE HEAD IN GUINEA PIGS

Ashutosh Jnawali, Krista M Beach, Lisa A Ostrin

Published in Current Eye Research. 2018 Aug;43(8):1006-1018.

### 3.2 Introduction

Myopia is associated with structural changes in the eye, including a longer axial length, thinner choroid,<sup>126, 127</sup> and changes in optic nerve head morphology.<sup>23</sup> Furthermore, myopia poses an increased risk for the development of primary open angle glaucoma,<sup>12, 13, 15</sup> which results in nerve fiber layer thinning<sup>128</sup> and optic nerve head changes, including decreased minimum rim width<sup>129</sup> and increased Bruch's membrane opening,<sup>130</sup> ultimately leading to permanent vision loss. Guinea pigs are becoming an increasingly popular model of myopia,<sup>27, 28, 131</sup> and may also represent a promising model of glaucoma. Guinea pig retinal physiology, both *in vitro* single cell recordings<sup>132, 133</sup> and *in vivo* electrophysiology,<sup>37, 134</sup> have previously been characterized. Additionally, *in vitro* retinal and optic nerve head (ONH) structures in the guinea pig have been examined,<sup>38, 135</sup> however, *in vivo* methods to assess the retina, choroid and ONH have not yet been established.

Optical coherence tomography (OCT) is a non-invasive imaging technique using low-coherence interferometry for cross sectional imaging of the internal tissue microstructures. OCT is widely used as an objective clinical and research tool for high resolution imaging of the retina, choroid, and ONH.<sup>136-138</sup> With the introduction of spectral domain (SD) OCT and eye tracking technology, high resolution scans can be obtained in a short period of time, with greater than 50,000 axial scans per second.<sup>55, 139, 140</sup> Studies have shown that SD-OCT has high intra- and inter-session reproducibility in monitoring glaucoma progression.<sup>138, 141-143</sup> OCT as a method to assess

*in vivo* ocular structures in the guinea pig would be a beneficial technique to follow disease progression in this animal model.

Myopia and glaucoma have been studied in a wide variety of animal models, including dogs,<sup>144</sup> rats, mice,<sup>145, 146</sup> zebrafish<sup>147</sup> and non-human primates,<sup>148</sup> among others, which has contributed to our understanding of the disease pathology and led to innovative treatment strategies.<sup>149, 150</sup> However, each animal model presents unique challenges. Non-human primate models, though having a close resemblance to human anatomy and cellular organization, have limitations in terms of economics and practicality.<sup>151</sup> Current rodent models provide an opportunity to study genetic manipulations and test large numbers of animals, but are limited by their small globe size and structural differences in the ONH compared to humans,<sup>149</sup> primarily the absence of a collagenous lamina cribrosa.<sup>45, 152</sup> Structural changes in the lamina cribrosa have been described in glaucomatous eyes in a number of previous studies.<sup>129, 153, 154</sup> Unlike rats and mice, guinea pigs possess a collagenous lamina cribrosa,<sup>38</sup> which may be better suited to model glaucomatous change observed at the ONH in humans. Additionally, it has been demonstrated that guinea pigs do not require anesthesia for intraocular pressure measurements with rebound tonometer<sup>38</sup>; therefore, anesthesia induced alterations in intraocular pressure can be avoided with this technique in guinea pigs.

Another advantage of the guinea pig compared to other rodents are the similarities in retinal physiology with primate retina. Unlike rats and mice which are nocturnal creatures and possess an ultraviolet sensitive cone, guinea pigs are crepuscular and have short and medium wavelength cones with spectral sensitivity similar to the primate retina.<sup>33</sup> Guinea pig photopic electroretinogram (ERG) responses are much closer to primate photopic ERG responses than that

of the rat and mouse.<sup>36,37</sup> This similarity of guinea pig ERG to primate ERG is promising and offers potential for future studies.

Other benefits of the guinea pig include easy breeding, quick growth with developmental maturation at the age of 5 months, docile temperament, and wide availability.<sup>34</sup> Thus, guinea pigs, a precocial mammal frequently used as a model of human disease, are posed to be a valuable and informative model of both myopia and glaucoma structural and functional studies.

A number of studies have evaluated the retinal organization of guinea pigs, mainly using a histological approach.<sup>111, 112</sup> While *in vivo* OCT imaging in mice<sup>155</sup> and rats<sup>156, 157</sup> has been validated, few studies have utilized this technique in guinea pigs. Most recently, Li, et al, used OCT to assess retinal and choroidal thickness in guinea pigs to correlate axial length and refraction, and to compare to histological sections.<sup>158</sup> The authors reported good agreement between *in vivo* and histological measurements; however, transverse scaling was not accounted for, and only a single point in the posterior pole was assessed. Other retinal and ONH metrics, such as nerve fiber layer thickness, Bruch's membrane opening, and minimum rim width have not been evaluated in guinea pigs. Quantification of such parameters in normal guinea pigs is critical in characterizing structural changes which are expected to occur in conditions such as myopia and glaucoma. The goal of this study was to establish protocols for *in vivo* OCT imaging in the guinea pig and to characterize normal retinal, choroidal, and ONH structures. To this aim, we assessed intraobserver, interocular and intersession differences in normal guinea pigs, and compared *in vivo* images to histological analysis.

### **3.3 Materials and Methods**

Nine adult pigmented guinea pigs of Elm Hill breed (Elm Hill Labs, MA, USA), aged 2.5 years, were included in this study (6 female, 3 male). The mean weight of males was  $1151.75 \pm$

163.65 g and that of females was  $1070.5 \pm 71.28$  g. Animals were kept under 12 hour light/dark cycle and provided food and water *ad libitum*. Procedures were approved by the Institutional Animal Care and Use Committee at the University of Houston and conformed to the ARVO statement for the Use of Animals in Ophthalmic and Vision Research.

### 3.3.1 Animal preparation

For imaging, animals were anesthetized with a subcutaneous injection of ketamine (30 mg/kg, VEDCO Inc, MO USA) and xylazine (3 mg/kg, Lloyd Laboratories, Philippines). Both eyes were dilated with topically instilled 2.5% tropicamide (Bauch and Lomb, NY USA) and 1% phenylephrine (Paragon BioTeck Inc, OR USA). The eyelids were held open with a custom lid speculum. To prevent the corneal surface from drying and to optimize optical quality, custom contact lenses were fabricated in-house (DAC 2X-ALM OTT, DAC International, CA USA) with Boston XO material, and inserted with artificial tears (Refresh Liquigel, Allergan). Contact lens parameters included a 3.5 mm central thickness, 8 mm total diameter, and 4.5 mm base curve.

### 3.3.2 Image Acquisition

*In vivo* imaging was performed for both eyes of each animal with spectral domain optical coherence tomography (SD-OCT, Spectralis HRA+OCT; Heidelberg Engineering, Heidelberg, Germany) with an 870 nm (average) super luminescent diode light source. High resolution imaging mode was utilized with an acquisition rate of 38,400 a-scans per second. The axial resolution of the instrument is 3.5  $\mu\text{m}$ /pixel digital (7  $\mu\text{m}$  optical) and lateral resolution of 6  $\mu\text{m}$ /pixel digital (14  $\mu\text{m}$  optical). Animals were positioned prone on a custom-built stage, and the instrument was aligned with the eye using the x-y-z adjustment of the camera. The posterior segment was brought into focus by first adjusting the instrument's focus and then adjusting the reference arm to bring the retinal surface into sharp focus. The mean scan focus was  $-3.77 \pm 2.20$  D for OD and  $-3.61 \pm$

1.78 D for OS. The imaging focus was similar across two eyes and across imaging sessions. Scan parameters included a 12° circular scan (1536 a-scans, Figure 3-1A) and a 24 line radial scan (20°, 1024 a-scans per line, 7.5° intervals, Figure 3-1B), both centered on the optic nerve head (ONH). Enhanced depth imaging mode was utilized for improved visualization of the choroid. Preliminary imaging showed that averaging 40 frames for circular scans and 16 frames for radial scans provided optimum noise reduction and image quality, and was therefore used for image acquisition. All images had image quality above 25 dB (mean  $29 \pm 2.75$  dB). Approximately one week after the initial session, imaging was repeated in one eye for all animals. To minimize scan distance as a confounding factor, the contact lens, the scan focus, and the reference arm length were kept constant for each eye of each animal.

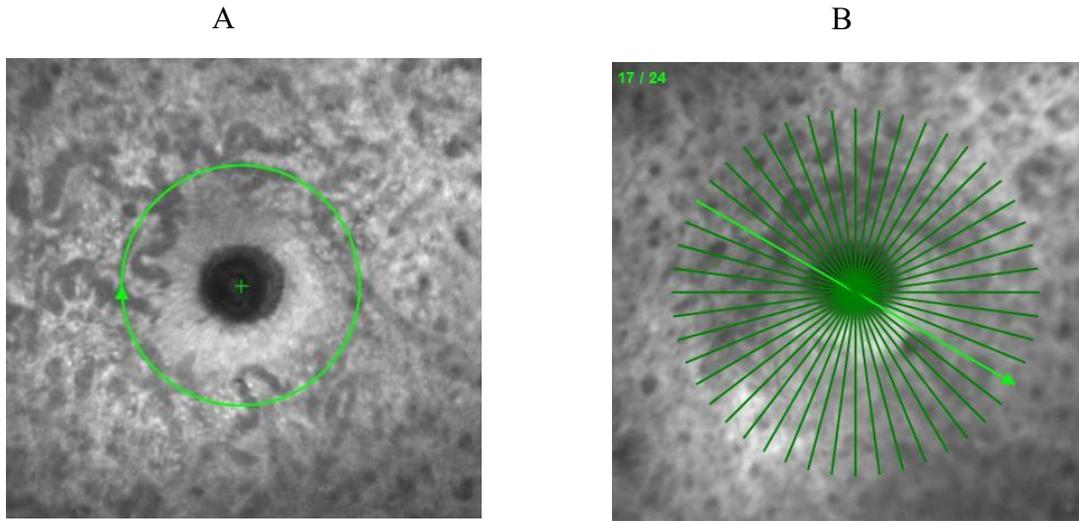


**Figure 3-1:** Representative scanning laser ophthalmoscope images of the ONH

A) Scanning laser ophthalmoscope image of the ONH showing the 12 degree circular scan centered on the ONH. B) Scanning laser ophthalmoscope image of the ONH showing the 20 degree, 24 line radial scan

### 3.3.3 Refraction and Biometry

Refractive error was measured for each eye with animals awake, hand held, and undilated. Streak retinoscopy (WelchAllyn, Skaneateles Falls, NY, USA) was performed twice and averaged. Biometry (LenStar, Haag-Streit, Germany) was performed under anesthesia. A lid speculum was inserted, and animals were positioned on a custom stage aligned with the instrument. The LenStar biometer uses optical low coherence reflectometry to determine corneal thickness, anterior chamber depth, lens thickness and axial length. Although LenStar is calibrated for measurement of ocular dimensions in human eyes, its use has been reported in much smaller eyes such as tree shrews,<sup>159, 160</sup> and as reported in these studies, the ocular dimensions of tree shrews are comparable to guinea pig eyes. Since guinea pig eyes are much smaller than human eyes, the short eye mode in the biometer was used so that consistent peaks for the four refractive surfaces (cornea, anterior and posterior lens and retina) were visible (Figure 3-2A). Axial length and lens thickness were measured for 8 eyes against a rule on the enucleated eyes (Figures 3-2B, 3-2C). To further confirm measurements obtained from Lenstar, ocular dimensions of two eyes were compared from the LenStar and A-scan ultrasonography (AXIS II, Quantel Medical, Bozeman, MT) using immersion technique with 10 scans per eye at a frequency of 11 MHz. The media velocities for anterior chamber (1540 m/s), vitreous chamber (1540 m/s), and lens (1645 m/s) were obtained from literature.<sup>34, 161</sup> Corneal refractive index and lens refractive index were obtained from published normative data for guinea pigs.<sup>34, 161</sup> Ocular dimensions from LenStar were compared to results from A-scan ultrasonography.

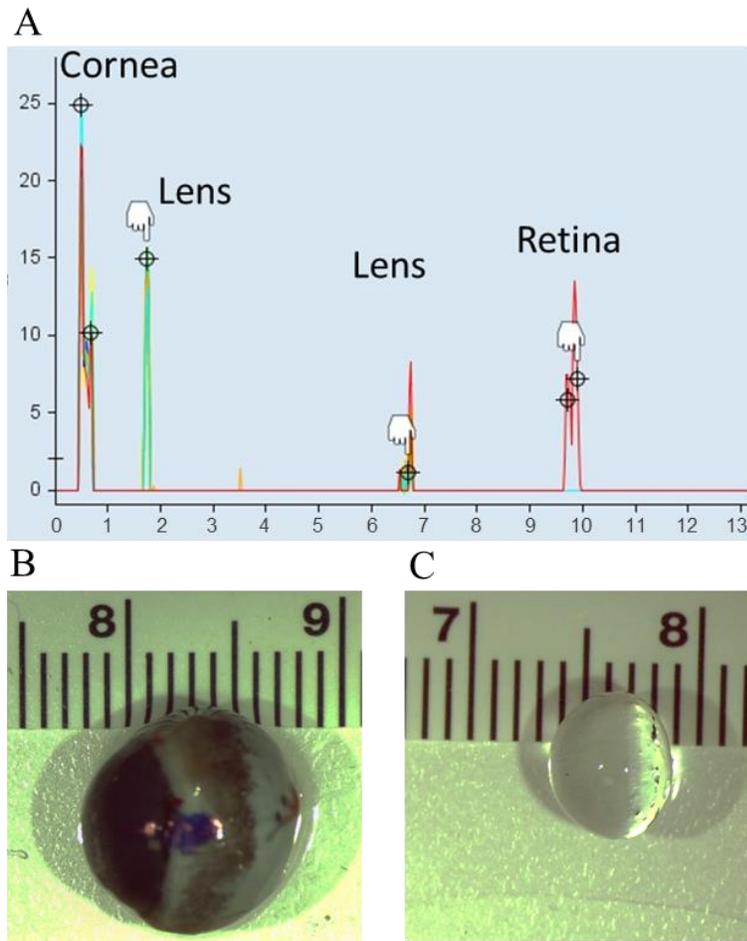


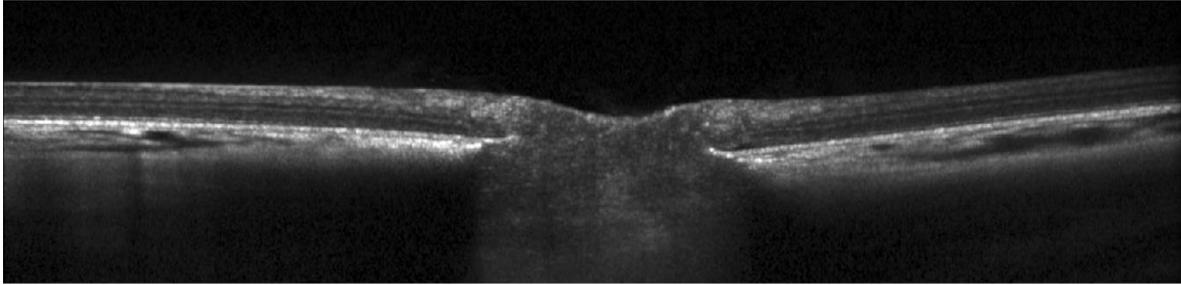
**Figure 3-2:** Representative biometry images from Lenstar compared against enucleated globe

A) Representative A- scan derived from the LenStar biometer from an adult guinea pig in this study. B) Enucleated globe and C) isolated lens shown against a scale (cm)

### 3.3.4 Image analysis

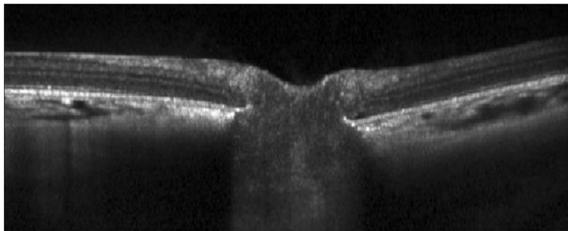
SD-OCT images were exported as raw (.vol) files. A custom program (MatLab, MathWorks) was used to optimize the image quality, scale the images to adjust for lateral magnification, and manually segment the images. To compensate for the transverse scaling, biometric measurements were used to create a three-surface schematic eye of the guinea pig to locate the posterior nodal point,<sup>162</sup> and calculate the distance from the posterior nodal point to the retina (i.e. posterior nodal distance, PND). We adopted the methods for scaling calculation described previously for a three surface schematic eye.<sup>163</sup> Assuming a spherical globe and retina to convert linear distance of PND to angular measure in microns per degree, the PND was used to calculate the scan length and transverse scaling. The assumption that the retina is spherical helps to convert the linear distance of posterior nodal point to the retina in angular distance in microns per degree, from the relationship of length of arc and radius in a spherical surface. This method of calculating the retinal magnification factor using posterior nodal point location has been described in detail in the literature.<sup>164, 165</sup> The microns per degree retinal scaling (RS) was calculated as  $RS = \frac{\pi}{180} \times PND$ . The transverse scaling (TS) in microns per pixel were calculated as  $TS = (\text{microns per degree})/(\text{pixels per degree})$ , and this value was used as the transverse scaling factor to account for lateral magnification. After calculating the transverse scaling, each OCT B-scan image was compensated so as to maintain the same size for the length and width of each pixel, which would give the corrected measurements in three dimensions. The perpendicular direction concerned with axial scaling is based on refractive index and interference in the different components of ocular media. As such, the axial scaling was taken as  $3.87 \mu\text{m}/\text{pixel}$  from the manufacturer's instructions. Figure 3-3 shows an image before and after scaling.

A



Unscaled Image

B



Scaled Image

**Figure 3-3:** Representative B-scan images from radial scans at the ONH

A) Raw OCT image through the optic nerve head. B) Same scan as (A) corrected for lateral magnification

For internal limiting membrane (ILM) and Bruch's membrane, the segmentation lines were automatically delineated, and lines were manually corrected for any segmentation errors. The points on the x and y axis were interpolated for nearest neighbor while fitting the line. For other layers, a line was plotted at the 0 y position on the image and modified manually to delineate the layer of interest. For circular and radial scans, the ILM, ganglion cell/nerve fiber layer (GC/NFL), outer plexiform layer (OPL), Bruch's membrane and posterior choroid were segmented to calculate thicknesses of GC/NFL, outer retina, total retina and choroid (Figures 3- 4A, 4B). Thicknesses were calculated for each of the 1536 a-scans of the circular scan and 1024 a-scans of each of the 24 line radial scans. For radial scans, Bruch's membrane opening (BMO) was manually identified for each line scan. The perpendicular distance from each of BMO point to the ILM was defined as minimum rim width (MRW). For BMO metrics, an ellipse was fitted through the 48 BMO points, and the area and diameter were calculated. Thickness maps were generated for total retina, GC/NFL, outer retina and choroid with the method of interpolation in Matlab, interpolating all points between the 20 degree line scans. The ONH region was excluded by applying a mask calculated from the BMO diameter. The remaining thickness map was divided into quadrants (superior, inferior, nasal and temporal) for sectoral thickness calculations.

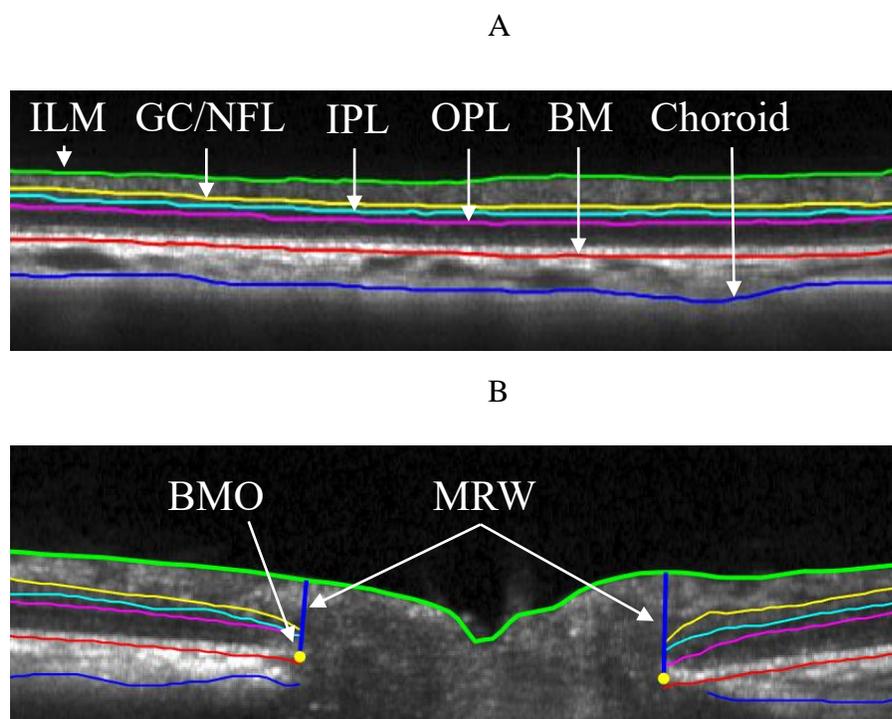


**Figure 3-4:** Representative segmentation images of circular and radial scans at the ONH

A) B-scan image of 12 degree circular scan. B) B-scan image for a single line of radial scan. Segmentation indicates inner limiting membrane (ILM, green), ganglion cell/nerve fiber layer complex (GC/NFL, yellow), inner plexiform layer (IPL, light blue), outer plexiform layer (OPL, magenta), Bruch's membrane (BM, red), and posterior choroid (blue).

### 3.3.5 Intraobserver, interocular, and intersession repeatability

To assess intraobserver repeatability, the image segmentation was repeated by the same observer (author AJ) on two separate occasions for one eye for each animal. For interocular comparisons, all measurements were compared between two eyes of each animal. For intersession repeatability, imaging was repeated in all animals at least a week after the first session.

### 3.3.6 Histology

Histology was performed on 7 eyes of 7 guinea pigs after OCT imaging. Animals were euthanized with 100 mg/kg sodium pentobarbital (Fatal-Plus, Vortech Pharmaceuticals, MI, USA). Eyes were marked for orientation, enucleated and bisected at the equator. Posterior segments were frozen (n = 6) or embedded in paraffin (n = 1). For frozen sections, tissue was fixed overnight at 4° C in a solution of 4% paraformaldehyde in 0.1M sodium phosphate buffer, and cryoprotected in successive sucrose infiltrations (5-20%) for 6 hours. Tissue was then embedded in a 1:1 solution of 20% sucrose and optimal cutting temperature freezing compound (Tissue-Tek) and snap frozen in liquid nitrogen. Orientation markings were made on the tissue block consistent with the orientation markings of the globe. Eight µm cryosections (Leica CM 1950, Leica) were cut from the posterior segment of the eye through the ONH. With the help of orientation markings, the sections were cut through the ONH in the horizontal dimension thus extending from nasal to temporal retina. For paraffin embedding, the posterior segment was fixed overnight in 4% paraformaldehyde, dehydrated and paraffin infiltrated. Following sectioning, the slides were deparaffinized with xylene and rehydrated. Frozen and paraffin embedded sections were stained with hematoxylin and eosin (H & E), mounted (Cytoseal 60, Richard-Allan), and imaged with a light microscope (DM1000, Leica, Germany). To be consistent with the radial scan findings from OCT imaging, three histological sections closest to the center of the ONH were used for analysis. Images

were imported into Matlab and analyzed similar to OCT imaging, with manual segmentation of the ILM, Bruch's membrane, GC/NFL, and inner and outer plexiform layers for thickness calculations. Histological sections were taken through the ONH horizontally from nasal to temporal retina to avoid the visual streak, which is reportedly in the superior retina above the ONH.<sup>111</sup> Hyper-reflective features of the OCT images were aligned with histological images to assess correspondence of retinal and choroidal layers.

### 3.3.7 Statistical analysis

Data are expressed as mean  $\pm$  standard deviation. Regional variations were assessed with one-way ANOVA with post-hoc Tukey-Kramer test for pairwise comparisons. The coefficient of variation (CV), intraclass correlation coefficient (ICC)<sup>166</sup> and 95% confidence intervals were calculated for intraobserver, interocular and intersession measures, and paired t-tests and Bland-Altman analyses<sup>167</sup> were performed. Statistical analysis was performed using MedCalc (MedCalc Software, 12.3.0, Mariakerke, Belgium). A critical value  $< 0.05$  was considered statistically significant.

## 3.4 Results

### 3.4.1 Refraction and Biometry

Animals were hyperopic, with a mean spherical equivalent refraction of  $+3.50 \pm 0.77$  D. Mean axial length was  $9.997 \pm 0.12$  mm, and mean corneal power was  $71.09 \pm 2.85$  D. There were no statistically significant differences between the right and left eyes for refractive and biometric measures (Table 3-1).

**Table 3-1:** Spherical equivalent refraction and biometric measurements, including central corneal thickness, anterior chamber depth, lens thickness, axial length, and mean corneal power, for right (OD) and left (OS) eyes (n = 8), compared with paired t-test

	<b>Spherical equivalent refraction (D)</b>	<b>Central corneal thickness (μm)</b>	<b>Anterior chamber depth (mm)</b>	<b>Lens thickness (mm)</b>	<b>Axial length (mm)</b>	<b>Corneal power (D)</b>
OD	+3.28 ± 0.94	251.75 ± 20.81	1.21 ± 0.09	5.52 ± 0.08	9.995 ± 0.11	72.18 ± 2.83
OS	+3.73 ± 0.55	252.5 ± 20.75	1.21 ± 0.11	5.54 ± 0.08	9.998 ± 0.13	70.00 ± 2.87
<i>P</i> value	0.299	0.94	0.94	0.67	0.77	0.20

For 8 eyes that were measured *in vivo* with the LenStar and subsequently enucleated and measured against a scale, average *in vivo* lens thickness and axial length were  $5.34 \pm 0.04$  mm and  $10.00 \pm 0.07$  mm, respectively, and *ex vivo* isolated lens thickness and axial length were  $5.52 \pm 0.12$  mm and  $10.70 \pm 0.39$  mm. The LenStar measures axial length from the cornea to the retinal pigment epithelium, whereas *ex vivo* axial length was measured from the cornea to the sclera, so also includes the choroid and sclera. The guinea pig sclera is reported to be around  $200 \mu\text{m}$ .<sup>168</sup> Thus, the LenStar axial length measurements are expected to be shorter than *ex vivo* measurements. Additionally, the isolated eye is no longer restrained by extraocular muscles within the orbit and therefore, small increases in length are expected after enucleation. The isolated lens is no longer stretched by zonular fibers, and therefore lens thickness is expected to be slightly different *ex vivo* compared to *in vivo*. For two additional eyes in which the ocular dimensions were measured with the LenStar and A-scan ultrasonography, axial dimensions corresponded well (shown in the representative Figure S1 in the supplemental material).

#### 3.4.2 Thickness of retinal layers

From OCT images, mean total retinal thickness was  $151.13 \pm 6.38 \mu\text{m}$ , GC/NFL thickness was  $40.39 \pm 2.53 \mu\text{m}$ , outer retinal thickness was  $68.32 \pm 2.75$  and choroidal thickness was  $71.36 \pm 8.57 \mu\text{m}$ . A representative example of the ILM and BMO delineation is shown in Figure 3-5. Minimum rim width was  $139.34 \pm 17.17 \mu\text{m}$ , BMO area was  $0.192 \pm 0.023 \text{ mm}^2$ , and BMO diameter was  $489.66 \pm 16.24 \mu\text{m}$ . Rim volume was  $0.0126 \pm 0.0022 \text{ mm}^3$ .

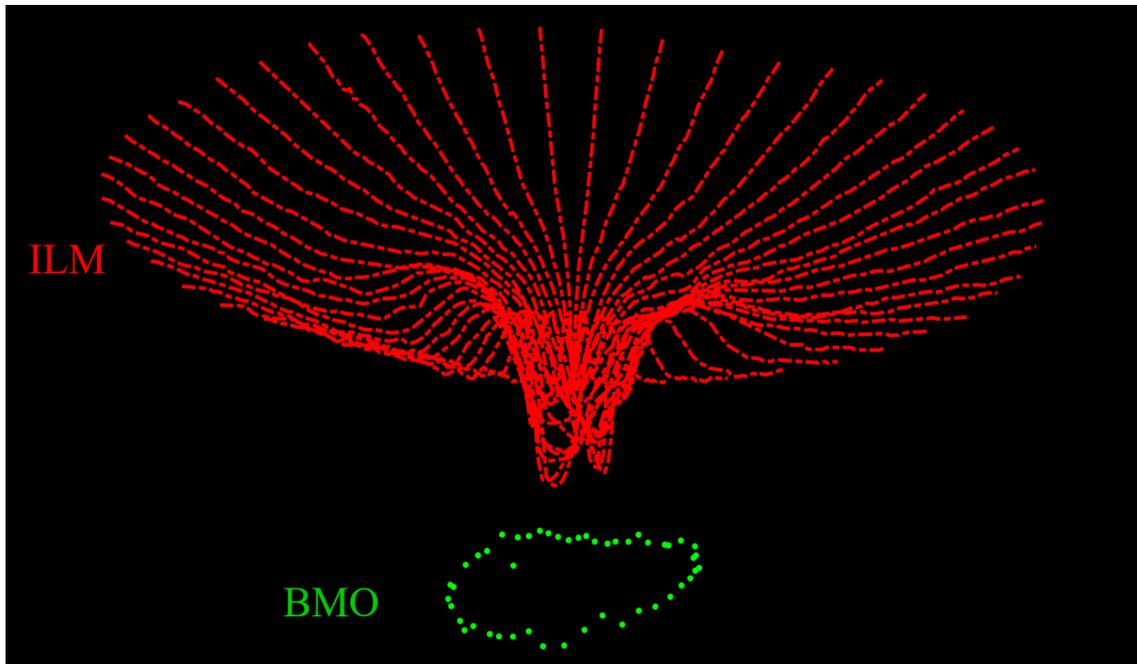


**Figure 3-5:** A point cloud illustration of the ILM and BMO points

A three-dimensional point cloud illustrating the inner limiting membrane (ILM, red) and Bruch's membrane opening (BMO, green) for one eye, derived from a 24 line radial scan.

### 3.4.3 Regional variations

Thicknesses for total retina, GC/NFL, outer retina and choroid by quadrant are shown in Figure 3-6. One-way ANOVA showed that there were significant regional variations for total retinal thickness ( $F_{3,32} = 5.17$ ,  $p = 0.005$ ), GC/NFL ( $F_{3,32} = 17.91$ ,  $p < 0.001$ ), and outer retina ( $F_{3,32} = 13.43$ ,  $p < 0.001$ ). Post-hoc Tukey-Kramer pairwise comparisons showed that total retina thickness was greatest in the superior region ( $158.29 \pm 5.59 \mu\text{m}$ ) and least in the inferior region ( $149.8 \pm 4.81 \mu\text{m}$ ). The GC/NFL was thinnest in the superior region ( $39.14 \pm 2.71 \mu\text{m}$ ) and thickest in the inferior region ( $49.12 \pm 3.75 \mu\text{m}$ ). The outer retina was thickest in the superior region ( $72.91 \pm 3.20 \mu\text{m}$ ) and thinnest in the inferior region ( $63.32 \pm 2.87 \mu\text{m}$ ). There were no significant nasal/temporal variations with any retinal thickness measure. There were no significant regional variations observed in the choroid ( $F_{3,32} = 0.53$ ,  $p = 0.67$ ). The visual streak lies in the superior retina. (chapter 2)

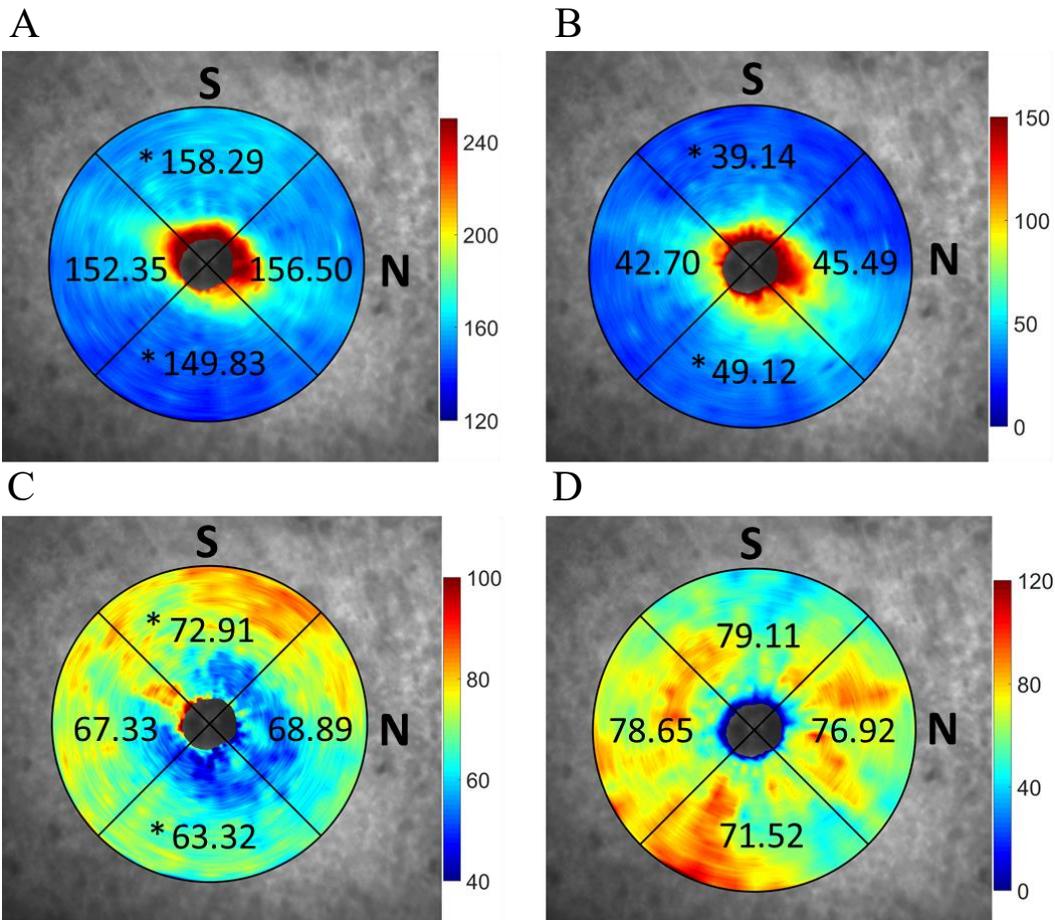


**Figure 3-6:** Thickness maps derived from 24 line radial scans

A) total retina, B) ganglion cell/nerve fiber layer complex, C) outer retina, and D) choroid, overlaid on the corresponding scanning laser ophthalmoscope images; \* indicates significant ( $p < 0.05$ ) difference between superior and temporal thicknesses. The numbers represent thickness in microns.

#### 3.4.4 Intraobserver, interocular, and intersession repeatability

Intraobserver repeatability was assessed for thicknesses of total retina, GC/NFL, outer retina and choroid, and ONH parameters by having the same observer segment the OCT images on two occasions (Table 3-2). Significant differences were observed for total retina, GC/NFL and choroid; however, these differences from repeat segmentation ranged from 0.56 to 6.05  $\mu\text{m}$ , which are not expected to be clinically significant. The ICCs for these measures ranged from 0.83 to 0.99, and CV ranged from 0.88% to 7.75%, indicating high repeatability.

For interocular measurements, one animal was excluded due to congenital structural irregularities around the optic nerve head of the right eye. For all thickness and ONH parameters, only outer retina thickness demonstrated significant interocular differences ( $p = 0.02$ , Table 3-3), with a mean difference of 1.70  $\mu\text{m}$ . For thickness measures, interocular ICCs ranged from 0.62 to 0.93 with CVs of 2.35% to 11.76%. For ONH parameters, ICCs ranged from 0.42 to 0.69 with CVs of 4.02% to 11.40%. Overall, these results indicate that the two eyes of each animal were correlated.

Intersession measurements showed high repeatability, with no parameters demonstrating a significant intersession difference (Table 3-4). For thickness measures, ICCs ranged from 0.93 to 0.97 with CVs of 0.90% to 4.17%. For ONH parameters, ICCs ranged from 0.44 to 0.90, with CVs of 4.96% to 10.23%. Bland-Altman analysis is shown for total retina, GC/NFL, outer retina and choroid thickness, and MRW and BMO diameter in Figure 3-7.

**Table 3-2:** Intraobserver measures for the left eye of each animal (n = 9), measurements compared with paired t-test (\* indicates significance at p < 0.05), intraclass correlation coefficient (ICC), 95% confidence interval (CI), and coefficient of variation (CV)

	Segmentation 1	Segmentation 2	Difference	p value	ICC	95% CI	CV (%)
Total retinal thickness (µm)	152.29 ± 5.04	154.24 ± 4.85	1.95	* <0.0001	0.99	0.98 to 0.99	0.95
GC/NFL thickness (µm)	41.73 ± 2.53	44.11 ± 2.40	0.56	* <0.0001	0.97	0.88 to 0.99	4.25
Outer retinal thickness (µm)	68.32 ± 2.76	68.11 ± 2.98	0.21	0.62	0.95	0.79 to 0.99	1.24
Choroidal Thickness (µm)	70.50 ± 10.94	76.55 ± 13.46	6.05	* 0.01	0.94	0.73 to 0.99	7.75
BMO area (mm <sup>2</sup> )	0.19 ± 0.02	0.19 ± 0.02	0.002	0.13	0.98	0.91 to 0.99	1.81
BMO diameter (µm)	493.79 ± 31.89	490.76 ± 29.98	3.03	0.16	0.98	0.92 to 0.99	0.88
MRW (µm)	130.43 ± 15.63	127.16 ± 15.50	3.27	0.17	0.91	0.66 to 0.98	3.59
Rim volume (mm <sup>3</sup> )	0.013 ± 0.002	0.012 ± 0.002	0.001	0.06	0.83	0.42 to 0.98	7.56

**Table 3-3:** Interocular measures for each animal (n = 8); right and left eyes are compared with paired t-test (\* indicates significance at p < 0.05), intraclass correlation coefficient (ICC), 95% confidence interval (CI), and coefficient of variation (CV)

	OD	OS	Difference	P value	ICC	95% CI	CV (%)
Total retinal thickness (µm)	150.51 ± 8.45	151.75 ± 5.10	1.24	0.55	0.80	0.02 to 0.96	2.66
GC/NFL thickness (µm)	39.13 ± 5.71	41.65 ± 2.69	2.52	0.17	0.62	-0.92 to 0.92	11.15
Outer retinal thickness (µm)	70.29 ± 3.13	68.59 ± 3.24	1.70	*0.02	0.93	0.64 to 0.99	2.35
Choroidal Thickness (µm)	74.76 ± 8.75	69.77 ± 11.46	4.99	0.23	0.62	-0.89 to 0.92	11.76
BMO area (mm <sup>2</sup> )	0.183 ± 0.017	0.196 ± 0.014	0.011	0.15	0.44	-1.80 to 0.89	8.16
BMO diameter (µm)	482.70 ± 22.28	496.62 ± 18.31	13.92	0.15	0.42	-1.88 to 0.88	4.02
MRW (µm)	140.34 ± 22.32	138.34 ± 18.45	2.0	0.22	0.69	-0.53 to 0.94	11.40
Rim Volume (mm <sup>3</sup> )	0.0127 ± 0.0032	0.0127 ± 0.0016	6.15 x 10 <sup>-5</sup>	0.95	0.63	-0.85 to 0.93	16.51

**Table 3-4:** Intersession measures for the left eye of each animal (n = 9), sessions compared with paired t-test (\* indicates significance at p < 0.05), intraclass correlation coefficient (ICC), 95% confidence interval (CI), and coefficient of variation (CV)

	Session 1	Session 2	Difference	P value	ICC	95% CI	CV (%)
Total retinal thickness (µm)	152.29 ± 5.04	152.26 ± 6.01	0.03	0.96	0.96	0.84 to 0.99	0.90
GC/NFL thickness (µm)	41.72 ± 2.52	42.28 ± 3.31	0.56	0.22	0.95	0.78 to 0.99	2.17
Outer retinal thickness (µm)	68.32 ± 2.75	68.37 ± 3.09	0.05	0.92	0.93	0.67 to 0.98	1.50
Choroidal Thickness (µm)	70.5 ± 10.93	71.38 ± 10.55	0.88	0.52	0.97	0.85 to 0.99	4.17
BMO area (mm <sup>2</sup> )	0.192 ± 0.023	0.189 ± 0.018	0.002	0.79	0.46	-1.39 to 0.88	10.23
BMO diameter (µm)	493.79 ± 31.89	490 ± 24.07	2.81	0.81	0.44	-1.50 to 0.87	4.96
MRW (µm)	130.43 ± 15.64	137.23 ± 17.57	6.80	0.08	0.90	0.55 to 0.98	6.08
Rim Volume (mm <sup>3</sup> )	0.0126 ± 0.0022	0.0126 ± 0.0013	3.3 x 10 <sup>-6</sup>	0.99	0.88	0.47 to 0.97	6.98

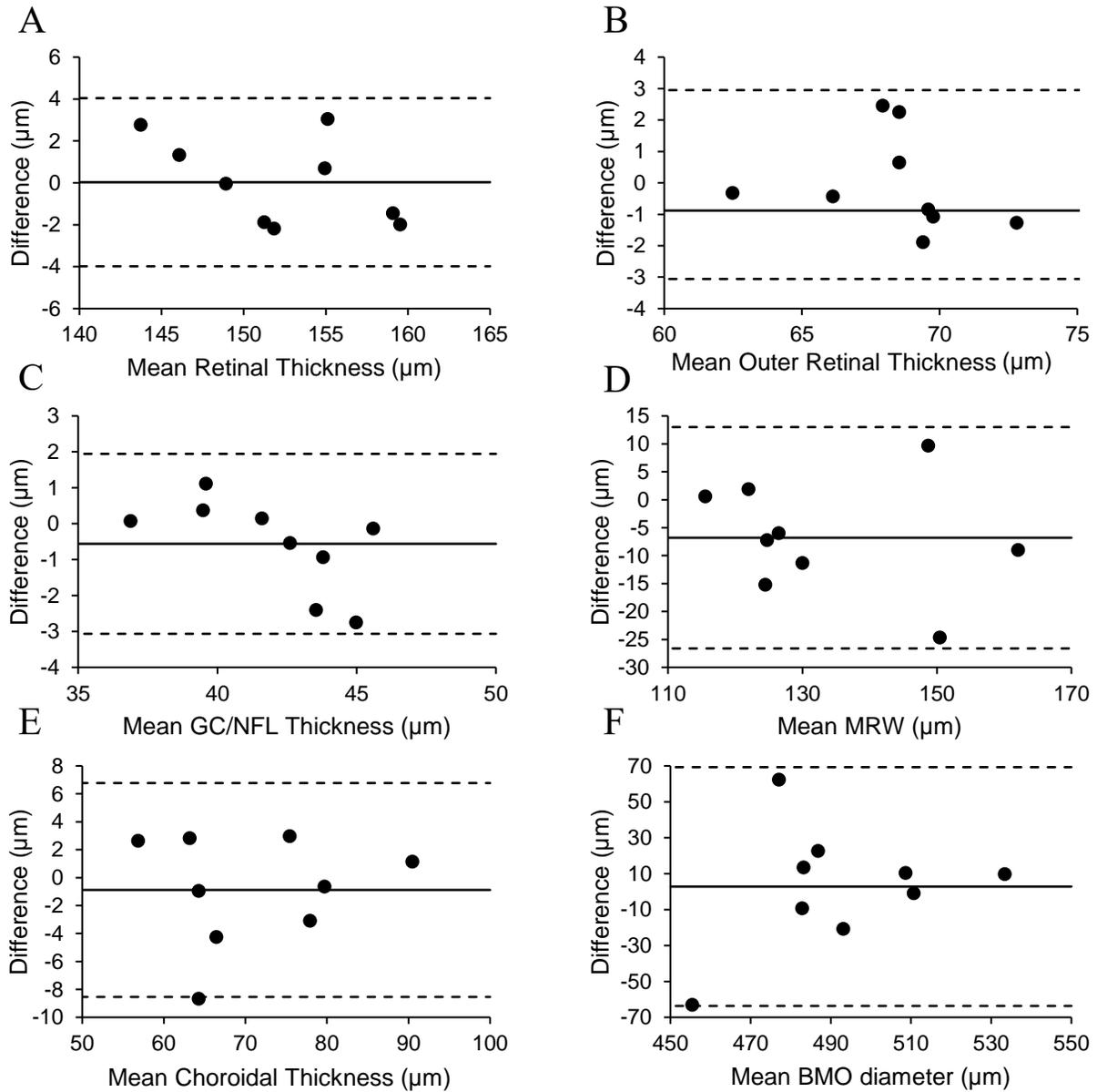


**Figure 3-7:** Intersession Bland-Altman analysis

A) total retinal thickness, B) outer retinal thickness, C) ganglion cell/nerve fiber layer (GC/NFL) thickness, D) minimum rim width (MRW), E) choroidal thickness, and F) Bruch's membrane opening (BMO) diameter.

### 3.4.5 In vivo versus histological measurements

Histological sections (cryosection) showed that all retinal layers were visible in the OCT image (Figure 3- 8). Hyper-reflective regions of the OCT images corresponded to the RPE, inner/outer segment junction, outer plexiform layer, inner plexiform layer, and nerve fiber layer. OCT and histological thickness measurements are shown in Table 3-5. Total retinal thickness measured from histological images was  $140.41 \pm 10.57$ , which was not significantly different than that from the OCT images of the same eyes, at  $151.17 \pm 8.16$  (paired t-test,  $p = 0.11$ ). The GC/NFL, outer retinal, and choroid thickness were also not significantly different between *in vivo* and *in vitro* measures ( $p > 0.05$  for all).

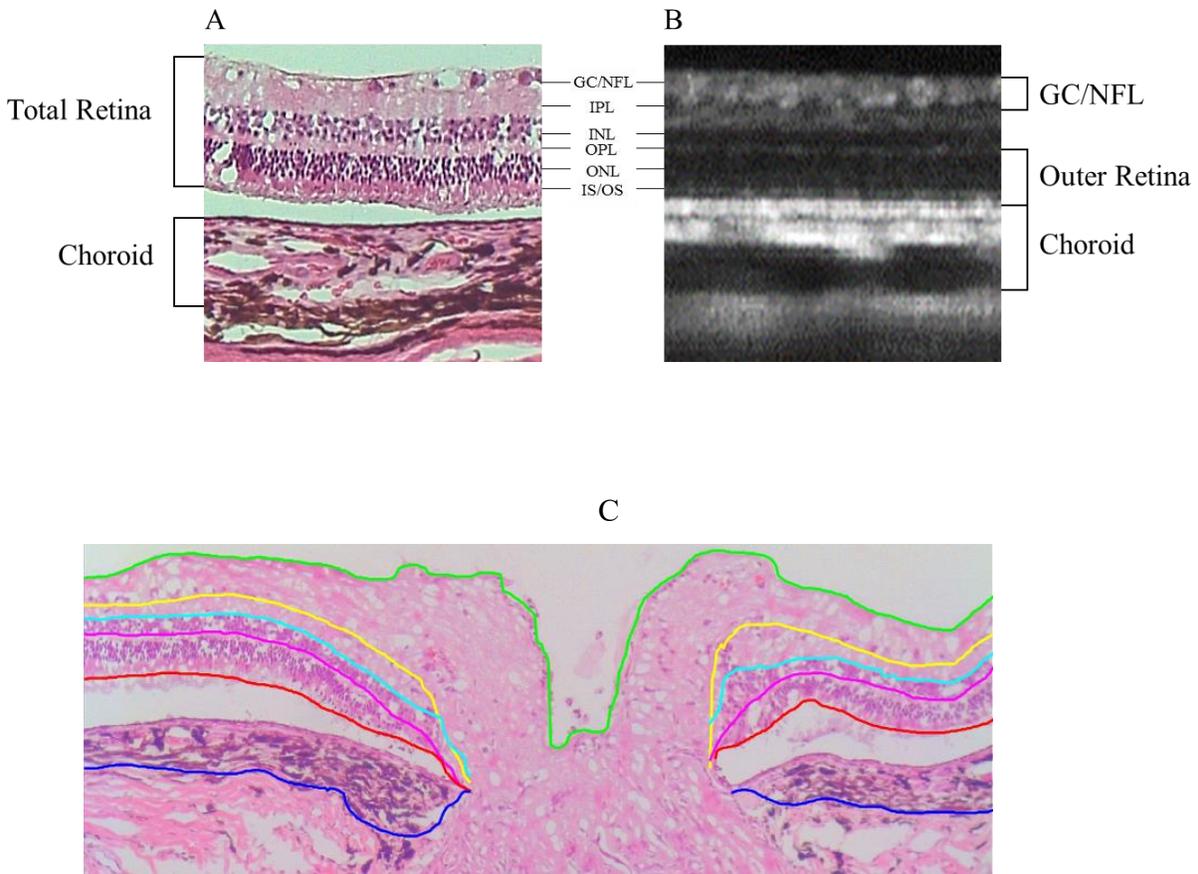


**Figure 3-8:** Representative images comparing OCT b-scan with histological section

A) Histological section showing tissue layers with corresponding layers in the (B) OCT b-scan. C) Segmentation of the layers in a representative histological section showing the inner plexiform layer (ILM, green), ganglion cell/nerve fiber layer complex (GC/NFL, yellow), inner plexiform layer (IPL, light blue), outer plexiform layer (OPL, magenta), Bruch's membrane (BM, red), and choroid (blue).

**Table 3-5:** Measures derived from OCT imaging and histology for the same eyes (n = 7)

<b>Variable (<math>\mu\text{m}</math>)</b>	<b>OCT</b>	<b>Histology</b>	<b>Difference</b>	<b>r</b>	<b>p value</b>
Total retinal thickness	151.17 $\pm$ 8.16	140.41 $\pm$ 10.57	10.76	0.65	0.11
GC/NFL thickness	39.49 $\pm$ 6.14	52.84 $\pm$ 10.29	13.34	0.58	0.17
Outer Retina thickness	70.26.32 $\pm$ 1.98	60.28 $\pm$ 8.42	9.99	0.29	0.53
Choroid thickness	69.82 $\pm$ 6.36	62.47 $\pm$ 1.13	7.35	-0.17	0.72

### 3.5 Discussion

The main goals of this study were to demonstrate the feasibility of *in vivo* imaging in guinea pigs with OCT, assess the repeatability, and compare findings with histology. Our results show that *in vivo* imaging demonstrates high repeatability within and between imaging sessions. Findings were similar between eyes of the same animal. We successfully quantified ONH parameters, including minimum rim width and BMO area, which will be important in future studies assessing effects of experimental glaucoma, as well as assessing potential structural changes in experimental myopia.

#### 3.5.1 Biometry

We used the LenStar biometer to determine axial dimensions of the guinea pig eye to calculate transverse magnification of the OCT images. Although LenStar is calibrated for measuring axial dimensions in human eyes, its use for measurement of axial dimensions has been previously reported in smaller eyes, including those of tree shrews, which have ocular dimensions similar to that of guinea pigs.<sup>159, 160</sup> In the chick eye, Penha, et al, report high correlation for anterior chamber depth, vitreous chamber depth, and axial length, with only a 0.5 mm difference in axial length between A-scan ultrasound and optical low-coherence tomography.<sup>169</sup> Here, we measured enucleated globes and isolated lenses against a ruler under a dissecting microscope, and found the measurements were similar to those from the LenStar. However, enucleated tissue may be subject to deformation. Therefore, we also compared the ocular dimensions of the guinea pig eye from the LenStar with A-scan ultrasonography using immersion technique for two additional eyes, and found that measurements between ultrasound and the LenStar corresponded well.

### 3.5.2 Refractive Indices

The refractive indices for schematic eye calculations were derived using Abbe refractometer<sup>161</sup> which generally uses the standard wavelength of 589 nm, although the latest models allow use of wavelength other than 589 nm. We assume that the standard wavelength was used for refractive index calculation, though this is not specified. Since the central wavelength used in the Spectralis in our experiments is 870 nm, we can expect some small difference in the refractive indices of different media when compared to the literature. In rat eye, the refractive indices of different ocular components have previously been evaluated across the visible spectrum.<sup>170</sup> The authors demonstrated a change in refractive index of the ocular components by approximately 0.02 across the visible spectrum, which suggests that although the index does change with wavelength, the change is small. In the same paper, the authors also demonstrated that the posterior nodal distance (PND) has a trivial variation across the visible spectrum ( $3^\circ$ ), which suggests that the difference in wavelength used to calculate the refractive index and the one used in OCT should be negligible in the calculations for ocular magnification and image compensation.

### 3.5.3 Comparing measurements from in vivo imaging with histological measurements

It is important to evaluate whether OCT accurately reflects the true measure of the anatomy. In humans, non-human primates and rats, *in vivo* OCT imaging of retinal and ONH morphology has been found to correspond well with histology.<sup>56, 136, 171</sup> Here, reflective features in OCT images corresponded to plexiform and RPE layers, while dark regions corresponded to nuclear layers. Though histological thickness measurements have historically been the gold standard for tissue structure studies, histological preparation alters tissue thickness with shrinkage during fixation and expansion during rehydration. Shrinkage can occur unevenly across a given sample because of differing protein content between different cell types. We were unable to

validate the thickness measurements from OCT imaging with histological sectioning as our histological sections showed variable tissue behavior (shrinkage/expansion/detachment) between the retinal layers. Studies show that fixed retinal tissue tends to undergo shrinkage, with the retinal nerve fiber layer least susceptible to shrinking, likely accounting for observed differences between our *in vivo* and histological measurements.<sup>172</sup>

#### 3.5.4 RNFL thickness

The retinal NFL thickness is an important clinical diagnostic measure in glaucoma.<sup>173</sup> Decreased thickness of the NFL and alterations in ONH parameters, including minimum rim width and BMO area, have been observed in human glaucoma subjects using SD-OCT.<sup>142, 174</sup> Similar results have been shown in non-human primates,<sup>175</sup> mice,<sup>176</sup> and rats.<sup>177</sup> We demonstrated that the retinal ganglion cell/NFL thickness can be assessed with good repeatability using SD-OCT in guinea pigs, with an intraclass correlation coefficient of greater than 0.9 for intraobserver and intersession measurements.

#### 3.5.5 Retinal Thickness in Rodents

Unlike rats and mice, guinea pigs have an avascular inner retina, with blood supply provided by the choroid. Avascular retinæ that wholly depend on choroidal blood supply are generally thinner than their intrinsically vascular counterparts.<sup>178</sup> In accordance with this, we found that the guinea pig retinal thickness, at about 152  $\mu\text{m}$ , is less than what has been reported in rats (242  $\mu\text{m}$ ),<sup>157</sup> and in mice (175  $\mu\text{m}$ ).<sup>179</sup> Similar results have been shown between vascular and avascular retinal thickness with retinal whole mounts.<sup>178</sup> The choroid, on the other hand was shown to be relatively thicker in guinea pigs, at about 70  $\mu\text{m}$ , while reported to be extremely thin in normal rats, at approximately 10  $\mu\text{m}$ .<sup>180</sup> The increased thickness of the guinea pig choroid potentially compensates for the absence of an inner retinal vascular supply.

### 3.5.6 Visual Streak and Retinal Thickness

Guinea pigs possess a visual streak, analogous to an area centralis in chicks<sup>181</sup> or fovea in primates,<sup>182</sup> which has a higher density of cells. In histological preparations, Choudhury reported a higher density of ganglion cells distributed in a nasal/temporal isodensity orientation inferior to the optic nerve head.<sup>112</sup> Conversely, other studies have reported a higher density of ganglion cells superior to the optic nerve head, within 1-2 mm above the ONH.<sup>111, 183</sup> With OCT imaging, we found greater retinal thickness superior to the optic nerve head. Specifically, this was due to an increased thickness of the outer retinal layer, suggesting a higher density of photoreceptors in this region. The 20 degrees scans centered on the ONH, utilized here, and extended approximately 1 mm in the superior retina. Thus, it is likely that the radial scans captured the region of visual streak. Further studies localizing the visual streak in guinea pigs, both *in vivo* and *in vitro*, will help to understand these observed regional variations. Because the guinea pig lacks a fovea, the pattern of arcuate field loss observed in humans with glaucomatous field damage might not be expected to occur in guinea pigs, similar to other rodent models of glaucoma. However, the many other similarities between human and guinea pig retinal and ONH structure discussed here still contribute to the guinea pig being a viable model of glaucoma.

### 3.5.7 Previous Findings

Our findings for retinal thickness ( $153.04 \pm 7.5 \mu\text{m}$ ) are comparable to those in previous studies of guinea pigs using OCT imaging, which reported retinal thicknesses of  $142.17 \pm 10.5 \mu\text{m}$  (3 mm from ONH), and  $129 \pm 1.3 \mu\text{m}$  (unspecified location).<sup>90, 158</sup> However, our measured choroidal thickness of  $79.01 \pm 13.43 \mu\text{m}$  is thinner than in both studies, which reported  $120.9 \pm 3.6 \mu\text{m}$  and  $134.20 \pm 16.22 \mu\text{m}$ . These differences in choroidal thickness could be due to the location that was sampled. Our measurements were derived from a 20 degree region surrounding

the ONH, covering a region of about 1 mm on either side of the ONH, whereas the previous study measured the choroid 3 mm from the ONH (the location in the other study was unspecified). Our OCT images show that choroidal thickness increases with distance from the ONH, as evident in the thickness maps in Figure 3- 6, which could explain the observed differences in choroid thickness between studies. Another potential source for variations between studies could be differences in the methods used for compensation of images during the analysis. Other possibilities that could account for differences between studies include guinea pig breed, age, OCT instrumentation, and image analysis methods. The guinea pigs used in this study were of Elm Hill breed and were 2.5 years old whereas those used in earlier studies were 5-6 weeks old and of unspecified strain.<sup>158</sup> It has been demonstrated in adult human subjects that choroidal thickness decreases with age.<sup>184, 185</sup>

Our results show greater variability of choroidal thickness across different imaging sessions compared to retinal thickness. The choroid is known to be a highly dynamic structure with variability in thickness resulting from a number of causes, including normal diurnal variation, use of dilating drops like tropicamide, water intake, and level of anesthesia. In our study, time of the day for repeat imaging was not controlled for; therefore, diurnal variation may have contributed to the variability in choroidal thickness. While not statistically different, the minimum rim width also demonstrated greater variability across imaging sessions compared to other parameters. The variability was likely due to difficulty in delineating the ILM at the ONH due to the protruding vascular tuft in some animals.

In OCT images, we were unable to reliably visualize the anterior lamina cribrosa surface, likely due to the thick nerve fiber layer and vascular sheath obscuring the ONH and decreasing the penetrance of the scanning laser. Using swept source OCT and additional image enhancement

techniques may improve the image quality for lamina cribrosa evaluation in guinea pigs, but that has yet to be demonstrated. However, presence of a distinct, collagenous lamina cribrosa in guinea pigs has been reported in a previous study using histological approaches.<sup>38</sup>

### 3.5.8 Limitations of Study

A limitation in imaging the guinea pig retina is the lack of retinal vasculature as a landmark, which is a disadvantage when attempting to identify the same retinal location over repeated sessions. The optic nerve head is the only clear structure visible in the fundus image. Scans were centered over the ONH, and positional rotation might be present from one session or one eye to another, which likely accounted for some variability observed here in intersession and interocular measurements. However, there are other prominent landmarks in the guinea pig retina, like vertical and horizontal streaks, which are also prominent around the ONH, and are likely the underlying choroidal vasculature seen through the thin avascular retina. The follow up mode from Heidelberg was used for repeated imaging, and the system appeared to track locations through these landmarks, as the scan tilts changed with eye positioning in follow-up scans, and the B-scan images for radial and circular scans were similar across sessions. Heidelberg states that it employs TruTrack eye tracking in the autorescan mode for precise follow up of retinal locations across imaging sessions; however, it is unclear which retinal landmarks are utilized by the instrument. While the lack of vasculature can make it difficult to identify precise locations in the retina, it can also be an advantage to isolate disease mechanisms that are nonvasculature in nature. Additionally, the absence of inner retinal vasculature allows direct measurements of the nerve fiber layer without requiring mathematical subtraction of the vessels. Another limitation in our study was the lack of cycloplegia during refraction measurements. Guinea pigs have an accommodative amplitude of approximately 5 diopters.<sup>186</sup> However, they have been shown to demonstrate a poor voluntary

accommodative response,<sup>187</sup> and therefore, we do not expect the lack of cycloplegia to have a significant effect on refraction measurements. Another limitation was variations in time of day for OCT imaging, which might have contributed to observed variability in choroidal thickness measurements between animals and between sessions. The extent to which the guinea pig choroid undergoes diurnal thickness changes has yet to be investigated. Finally, variability between our *in vivo* and histological measurements could have been from tissue shrinkage and other structural changes that occur during processing.

### **3.6 Conclusions**

In conclusion, we demonstrated that high quality retinal imaging and *in vivo* characterization of guinea pig retina, and ONH are repeatable and in close agreement to histological measurements. Such *in vivo* imaging in guinea pigs has potential benefits in myopia and glaucoma studies in this animal model.

Acknowledgements: Thanks to Nimesh Patel for help with software development, Jason Marsack for creating the custom contact lenses, Chris Kuether for constructing the custom stages, and David Calkins for helpful comments on the manuscript.

Conflicts of interest: none

## CHAPTER 4: RETINAL GANGLION CELL ABLATION IN GUINEA PIGS

Ashutosh Jnawali, Xiao Lin, Nimesh B Patel, Laura J Frishman, Lisa A Ostrin

### 4.2 Introduction

The guinea pig is a common model of human ocular conditions. Guinea pigs are a convenient model because they are precocial, docile, breed quickly, and reach developmental maturation at five months of age.<sup>34</sup> Guinea pigs are valuable in vision research because of ocular structural and functional similarities with humans.<sup>36-38</sup> For example, unlike rats and mice, guinea pigs possess a collagenous lamina cribrosa,<sup>38</sup> an optic nerve head structure implicated in glaucomatous axonal damage in humans.<sup>41-43</sup>

While guinea pigs are being more commonly used as a model for ocular conditions, there are very few published studies that have evaluated *in vivo* ocular structure or visual function in guinea pigs. Photopic electroretinograms (ERGs), an objective measure of retinal function, have been described in guinea pigs; brief flash ERGs were reported to be similar to the human photopic ERG.<sup>37</sup> In the mammalian retina, the negative a-wave of the photopic ERG originates from photoreceptors and OFF bipolar cells, the positive b-wave originates from ON bipolar cells,<sup>64-66</sup> and oscillatory potentials (OPs) likely originate from amacrine cells. The photopic negative response (PhNR), a later negative going response evident in light adapted conditions, has been related to retinal ganglion cell activity in primates and in some studies of rodent ERGs.<sup>69-72</sup> However, contributions of retinal ganglion cells to the guinea pig flash ERG have not been determined.<sup>36, 37</sup> Furthermore, a pattern ERG response has not been demonstrated in guinea pigs. The pattern ERG is a light adapted retinal response to a contrast reversing pattern, which has been demonstrated to represent ganglion cell activity in several species including cats, non-human

primates, humans, mice, and rats.<sup>74, 100-103, 121, 124, 188</sup> However, in pigeon and chicken, ganglion cells appear not to contribute to the pattern ERG, as retinal ganglion cell ablation does not affect the response.<sup>104, 106</sup>

Optic nerve crush injury is a surgical procedure whereby the retrobulbar optic nerve close to the globe is crushed with forceps for a few seconds to induce apoptotic retrograde degeneration of retinal ganglion cell axons and cell bodies over time.<sup>189</sup> Animal models of optic nerve crush are commonly used to investigate underlying mechanisms for axonal injury-related retinal ganglion cell degeneration and to evaluate retinal structural and functional changes following retinal ganglion cell loss.<sup>61, 190, 191</sup> Following optic nerve crush in mice, progressive neuronal loss in the inner retina and the contralateral superior colliculus were observed one and four weeks following injury, respectively.<sup>61</sup> At three weeks following optic nerve crush in mice, a 60% loss of the retinal ganglion cell population was reported.<sup>192</sup> Optic nerve crush or transection has been used in mice and rats to demonstrate retinal ganglion cell contributions to the PhNR of the flash ERG and the pattern ERG.<sup>74, 101</sup>

The goal of this study was to determine the contributions of retinal ganglion cells to structural and functional markers in the guinea pig. We developed a technique for ganglion cell ablation in the guinea pig using optic nerve crush, evaluated retinal structural and functional changes longitudinally following optic nerve crush injury, and determined the contribution of retinal ganglion cells to flash and pattern ERGs. These techniques and findings will help to further establish the guinea pig as a model of human ocular pathologies and will be valuable when assessing progression in conditions such as glaucoma.

## **4.2 Methods**

Adult pigmented guinea pigs (n = 12) obtained from Elm Hill Labs (MA, USA) were included in this study. Animals were kept under 12 hour light/dark cycle and provided with food and water *ad libitum*. Procedures were approved by the Institutional Animal Care and Use Committee at the University of Houston and conformed to the ARVO statement for the Use of Animals in Ophthalmic and Vision Research.

### **4.2.1 Optic nerve crush procedure**

Animals underwent unilateral optic nerve crush in the right eye, and the left eye served as a control. For this procedure, animals were anesthetized with a subcutaneous injection of ketamine (30 mg/kg, VEDCO Inc, MO USA) and xylazine (3 mg/kg, Lloyd Laboratories, Philippines), and placed on a 40° C heating pad. Using a dissecting microscope (model, company), an incision was made in the temporal conjunctiva followed by blunt dissection of sub-Tenon's space to expose the optic nerve. The nerve was grasped with blunt forceps under direct visualization, 2-3 mm behind the globe, and pressure was manually applied for approximately 10 seconds. Care was taken not to cause injury to the surrounding vasculature or to the central retinal artery and vein within the optic nerve. Immediate dilation of the ipsilateral pupil and loss of the pupillary light reflex in the nerve crushed eye were used as confirmation of disruption of axonal signal . transduction. Nylon micro sutures (8-0, Ad Surgical, USA) were used to close the conjunctiva, and were removed one week later. Post-operative care included application of topical antibiotic ointment (Neomycin-Polymyxin B Sulfate) for one week and oral systemic anti-inflammatory agent (meloxicam) for three days.

#### 4.2.2 Behavioral visual function

A custom optokinetic instrument was developed for assessment of behavioral visual function. Animals were tested before and two weeks following optic nerve crush. The instrument consisted of a cylindrical drum of 55 cm diameter with a stationary platform at the center. Photographic paper with square wave grating of 1.5 cycles per degree (cpd), a spatial frequency previously shown to elicit tracking responses in guinea pigs,<sup>99</sup> lined the inside of the drum. Awake animals were placed on the central stationary platform in a plastic beaker. The drum was rotated at a constant speed of 12 degrees per second in both clockwise and counterclockwise directions. The tracking response of the animals to the rotating stimulus was determined by an experienced observer by evaluating head rotation in the direction of rotating stimulus. Animals were tested both monocularly and binocularly. For monocular testing, one eye was occluded using a black piece of cloth. The test was repeated at least three times for each direction of rotation, and tracking was confirmed by a second observer. Previous studies in our lab have shown that guinea pigs demonstrate directional selectivity for rotating stimulus in their visual field, with optimum responses in the temporal to nasal direction of rotation.<sup>193</sup>

#### 4.2.3 Ocular Imaging

Retinal, choroidal, and optic nerve head imaging was performed in both eyes before and every two weeks following optic nerve crush using spectral domain optical coherence tomography (SD-OCT, Spectralis HRA+OCT, Heidelberg Engineering, Heidelberg, Germany), as described previously.<sup>194</sup> Additionally, fluorescein angiography was performed two weeks after optic nerve crush injury using the angiography module in the SD-OCT. For imaging, animals were anesthetized with ketamine and xylazine, as described above, and placed in a prone position on a custom-built stage. The eyelids were held open with a custom lid speculum. Custom contact lenses

fabricated in-house (DAC 2X-ALM OTT, DAC International, CA USA) with Boston XO material, and were inserted with artificial tears (Refresh Liquigel, Allergan) to prevent the corneal surface from drying and to optimize optical quality for imaging by maintaining a smooth optical surface. Contact lens parameters included a 3.5 mm central thickness, 8 mm total diameter, and 4.5 mm base curve, which were determined based on normal ocular dimensions of guinea pig eyes.<sup>161</sup>

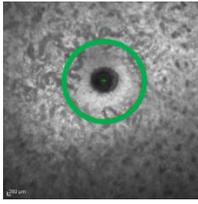
The SD-OCT instrument uses an 870 nm (average) super luminescent diode light source. High resolution imaging mode was utilized with an acquisition rate of 38,400 a-scans per second. Axial resolution of the instrument is 3.5  $\mu\text{m}$ /pixel digital (7  $\mu\text{m}$  optical) and lateral resolution of 6  $\mu\text{m}$ /pixel digital (14  $\mu\text{m}$  optical). The instrument was aligned with the eye using the x-y-z adjustment of the camera. The posterior segment was brought into focus by first adjusting the instrument's focus and then adjusting the reference arm to bring the retinal surface into sharp focus. A 12° circular scan (1536 a-scans, Figure 4-1A) centered on the optic nerve head was obtained. All scans had an image quality above 30 dB.

Scans were exported as raw (.vol) files. A custom program in MATLAB was used to optimize the image quality and manually segment the images. The internal limiting membrane (ILM) and ganglion cell/nerve fiber layer border were segmented to calculate thicknesses of retinal nerve fiber layer (RNFL, Figure 4-1B). Thicknesses were calculated for each of the 1536 a-scans of the circular scan, and analyzed for each of the four major quadrants (superior, inferior, nasal, and temporal).

Fluorescein angiography was used to assess the integrity of the choroid following optic nerve crush. The guinea pig inner retina is avascular, and the choroid is the primary source of nutrients and oxygen for the inner and outer retina. If the vasculature is compromised during optic nerve crush, both the inner and outer retina will undergo structural and functional loss, rather than

just the inner retina. For fluorescein angiography, 2 mg/kg sodium fluorescein (AK-Fluor, Akorn, IL, USA) was injected intraperitoneally in anesthetized animals approximately one minute prior to imaging. The method of intraperitoneal injection of fluorescein has been used for angiography with OCT imaging in rodents previously.<sup>195</sup> A 2.2 x 2.2 mm area centered at the optic nerve head was imaged using the scanning laser ophthalmoscopy function of the SD-OCT instrument, which uses a 488 nm light source for excitation of fluorescein. Images were captured for 5-10 seconds for on eye, and then the OCT camera was quickly moved to other eye, and the other eye was imaged for 5-10 seconds. This pattern of scanning with alternating between two eyes was continued for up to 4 minutes after the first appearance of fluorescein in the choroid.

A



B

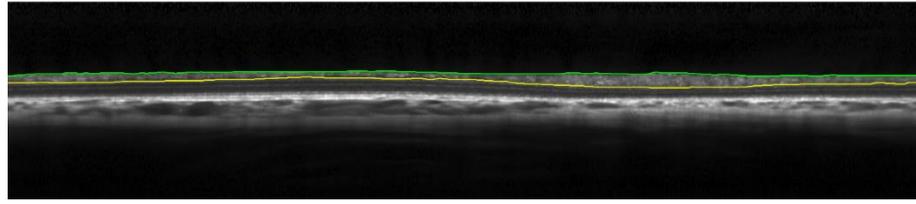


**Figure 4-1:** SD-OCT imaging of the guinea pig retina

A) 12° circumpapillary circular scan centered on the ONH B) corresponding b scan image segmented for ILM (green) and RNFL (yellow)

#### 4.2.4 Electrophysiology

Electrophysiological testing was performed in both eyes before and every two weeks following optic nerve crush for up to 12 weeks. Animals were anesthetized with ketamine and xylazine, and pupils were dilated with 1% tropicamide (Bausch and Lomb, NY, USA) for both flash and pattern ERGs. ERG recordings were obtained under light adapted conditions using the Celeris rodent ERG system (Diagnosys, LLC, MA, USA). The built-in heating function of the instrument's stage was used to maintain the body temperature at 37°C. A ground electrode was inserted under the skin on the fore limb. For pattern ERG, the probe, which includes an integrated electrode and stimulator, was placed in contact with the cornea and aligned with the center of the pupil, and the reference electrode was placed on the fellow eye. Based on schematic eye calculations of the guinea pig eye,<sup>194</sup> and specifications from Diagnosys, the pattern stimulus stimulated an area of approximately 4 x 4.6 mm in the central retina. The stimulus consisted of a square wave grating of 0.05 cycle per degree at 100% contrast, modulated at a temporal frequency of 1.05 Hz, and 1200 responses were averaged for each eye. The right, experimental eye was always recorded first, followed by the left, control eye. The stimulus of 0.05 cycle per degree was chosen because peak amplitude of PIN2 was obtained at this spatial frequency, as mentioned in chapter 2. Following pattern ERGs for each eye, flash ERGs were recorded. For flash ERG, stimulators were placed in contact with the cornea of each eye at the center of the pupil, and responses were collected from both eyes simultaneously. Flash strength was 10 cd.s/m<sup>2</sup>, and 30 responses were averaged for each eye.

ERG responses were analyzed using a custom written program in MATLAB (Mathworks, Inc., Natick, MA). For flash ERGs, a-wave amplitudes were measured in the raw trace from baseline to a-wave trough. For b-wave amplitude measurement, a band pass filter of 1-50 Hz was

applied to the raw trace, and the amplitude was measured from the a-wave trough to the b-wave peak. The PhNR was also measured from the filtered traces, from baseline to the immediate trough following the b-wave. Time to peak for a-wave, b-wave, and PhNR were also measured. With fast fourier transform (FFT) in MATLAB, the high frequency oscillatory potentials were noted in the ERG waves in the frequency band of 75-100 Hz. The OPs were extracted by the Celeris software during recording using a band pass filter of 75-300 Hz for the extraction. The OP waveforms were then analyzed in a MATLAB program without further processing. The amplitudes of the first through the third OPs were measured from the peak to the preceding trough, and the implicit time of the peak was measured from the stimulus onset.<sup>196</sup>

For analysis of pattern ERG responses, drift correction and a band pass filter of 1-100 Hz were applied to the raw traces. The first negative trough (N1), the first positive peak (P1) and the second negative trough (N2) were identified on the filtered waves. N1P1 and P1N2 amplitudes were determined.

#### 4.2.5 Intravitreal Injections

To further evaluate the retinal origins of the ERG and PERG waves, intravitreal injections of 10  $\mu$ l of GABA (gamma-aminobutyric acid, Sigma) dissolved in sterile Balanced Salt Solution (BSS, Acorn Ophthalmic) were performed to attempt to suppress inner retinal activity in the left eyes of six additional young guinea pigs of Elm Hill breed. Assuming a vitreal volume of 150uL the vitreal GABA concentration was 25 mM. Three subjects also received a vehicle intrvitreal injection of 10  $\mu$ l of BSS in their right eyes for vehicle control comparisons. The ERGs were recorded from these animals with the methods described earlier. Baseline flash and pattern ERGs were recorded, followed by the intravitreal injections using a 20 uL Hamilton syringe with a 30 G

needle. Flash ERGs were recorded starting at five minutes following the injections and were recorded for an additional 30 minutes. At the end, pattern ERGs were recorded again.

#### 4.2.6 In vitro ganglion cell quantification

At 4, 6, 9, and 12 weeks post optic nerve crush, animals were euthanized with 100 mg/kg sodium pentobarbital (Fatal-Plus or Euthasol, Vortech Pharmaceuticals, MI, USA). Experimental and control eyes were marked for orientation with sharpie markers, enucleated, and placed in phosphate buffered saline (PBS) solution. The orientations were further confirmed by evaluating the two posterior ciliary arteries running nasally and temporally around the globe from the optic nerve to the limbus. Eyes were fixed in 4% paraformaldehyde for 2 hours, orientation cuts were made, and the tissue was washed with PBS and PBS with tritonX. The whole eyecups with orientation cuts were then immersed in blocking buffer solution for at least an hour, and transferred to rounded bottomed tubes containing primary antibody, alpha-RBPMS (retinol binding protein with multiple splicing) rabbit Ab (Abcam, Cambridge, MA, USA) at 1:500 dilution. The eyecups were kept on rotator at 4°C for 5 days. On the sixth day, eyes were washed with PBS and PBS with tritonX, and the vitreous was removed under a light microscope (DM1000, Leica, Germany). Eyecups were labeled with secondary antibody, goat anti-rabbit alexa fluor 488 (ThermoFisher Scientific, Grand Island, NY, USA) at 1:250 dilution for 2 hours, followed by PBS with tritonX wash. Under low illumination, the retina was detached from the retinal pigment epithelium and choroid, and mounted on glass slides using Airvol mounting medium. The slides were left in dark overnight and imaged with DeltaVision wide field deconvolution fluorescence microscope (GE Life Sciences, Pittsburgh, PA) the following day.

Images of the retinal flat mounts were collected as panels under 20X. The panels were stitched together for composite images, saved as jpegs, and imported into ImageJ (NIH, MD, USA). The retinal whole mount images were divided into three concentric zones of equal areas, including center, mid-periphery, and periphery. In each zone, retinal ganglion cells were counted manually in five squares of 250 x 250 microns using cell counter in ImageJ (Figure 4-2). Counts were averaged for each zone and converted to cell density as cells/mm<sup>2</sup>.

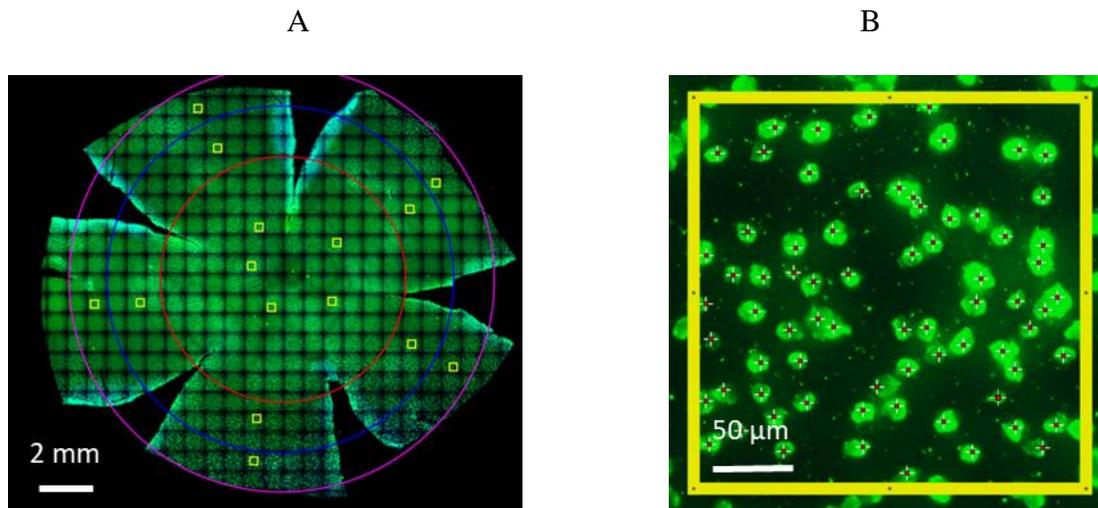


**Figure 4-2:** Retinal flat mount images from guinea pig eyes at 20X

A) Representative retinal flat mount image at 20X, immunostained with RBPMS for ganglion cells, and divided into 3 concentric zones of equal areas in ImageJ. Five 250 x 250 micron regions were analyzed from each of the three zones; B) Representative figure from one region of interest in the mid-periphery with retinal ganglion cells labeled using cell counter in ImageJ

#### 4.2.7 Statistical Analysis

Statistical analysis was performed using SPSS (IBM Corp., Armonk, N.Y., USA). Data are expressed as mean  $\pm$  standard deviation. Repeated measures ANOVAs with post-hoc Bonferroni corrected pairwise comparisons were used to assess differences between experimental and control eyes for OCT and ERG measurements. A critical value of  $< 0.05$  was considered statistically significant.

### **4.3 Results**

Fluorescein angiography showed that the choroidal vasculature was compromised in experimental eyes of two animals. The following analyses are therefore reported only for the remaining ten animals.

#### 4.3.1 Behavioral vision

Guinea pigs show optimal optomotor responses when the gratings are moving in the temporal to nasal visual field for each eye (see chapter 2).<sup>193</sup> At baseline, animals demonstrated tracking responses for each eye when monocularly viewing rotating gratings in the temporal to nasal direction of rotation with a spatial frequency of 1.5 cpd. When tested at two weeks following optic nerve crush, all animals had a total loss of tracking in experimental eyes. Tracking was intact in control eyes in all animals, and, similar to baseline, animals could track gratings of 1.5 cpd on all follow up sessions.

#### 4.3.2 Retinal structure

Thicknesses for peripapillary RNFL, and total retinal thickness, assessed with SD-OCT, are shown in Figure 3A and 3B, for baseline and every 2 weeks up to 12 weeks; data include progressively fewer animals as they were sacrificed at various time points during the course of the study. At 4 weeks following optic nerve crush, RNFL thickness in experimental eyes significantly

reduced from baseline (n = 10, baseline:  $49.43 \pm 2.45 \mu\text{m}$ ; 4 weeks:  $30.61 \pm 5.51 \mu\text{m}$ ,  $P < 0.05$ ). RNFL thinning was progressive, and at the end of the study period at 12 weeks, RNFL thickness was reduced by 65.32% from baseline, to  $17.14 \pm 2.13 \mu\text{m}$  (n = 3,  $P < 0.01$ ). RNFL thickness was also analyzed by quadrant (Table 4-1). At baseline, RNFL was thickest in the inferior quadrant (inferior > temporal > nasal > superior,  $P < 0.001$ ). RNFL thickness reduced progressively in all quadrants, and by the end of the study period at 12 weeks, the greatest reductions were observed in the inferior and temporal sectors, which were the thickest quadrants at baseline. There was no change in RNFL thickness contralateral control eyes throughout the study period ( $P > 0.05$ ). As seen in Figure 3B, the total retinal thickness was significantly reduced compared to contralateral control eyes at 8, 10 and 12 weeks following optic nerve crush.

**Table 4-1:** Retinal nerve fiber layer thickness ( $\mu\text{m}$ ) by quadrant at baseline and following optic nerve crush in right eyes; \*\* =  $P < 0.01$  indicating significant thinning at 12 weeks

<b>Time point</b>	<b>Superior</b>	<b>Nasal</b>	<b>Inferior</b>	<b>Temporal</b>
Baseline (n = 10)	39.9 $\pm$ 3.2	44.1 $\pm$ 2.4	57.1 $\pm$ 6.1	45.9 $\pm$ 4.5
2 weeks (n = 10)	34.9 $\pm$ 5.7	35.7 $\pm$ 7.5	51.8 $\pm$ 13.3	45.8 $\pm$ 12.1
4 weeks (n = 10)	28.1 $\pm$ 5.8	26.9 $\pm$ 4.9	35.6 $\pm$ 8.5	31.8 $\pm$ 7.1
6 weeks (n = 9)	22.7 $\pm$ 2.7	23.3 $\pm$ 3.5	28.0 $\pm$ 4.4	26.2 $\pm$ 3.3
8 weeks (n = 7)	19.9 $\pm$ 2.5	21.0 $\pm$ 3.0	21.4 $\pm$ 2.2	21.6 $\pm$ 4.2
10 weeks (n = 5)	18.8 $\pm$ 2.9	21.6 $\pm$ 3.7	21.0 $\pm$ 2.3	19.1 $\pm$ 4.7
12 weeks (n = 3)	17.1 $\pm$ 2.1	17.2 $\pm$ 1.7	16.2 $\pm$ 1.7	17.6 $\pm$ 4.4
P value	0.002**	< 0.001**	0.001**	< 0.001**

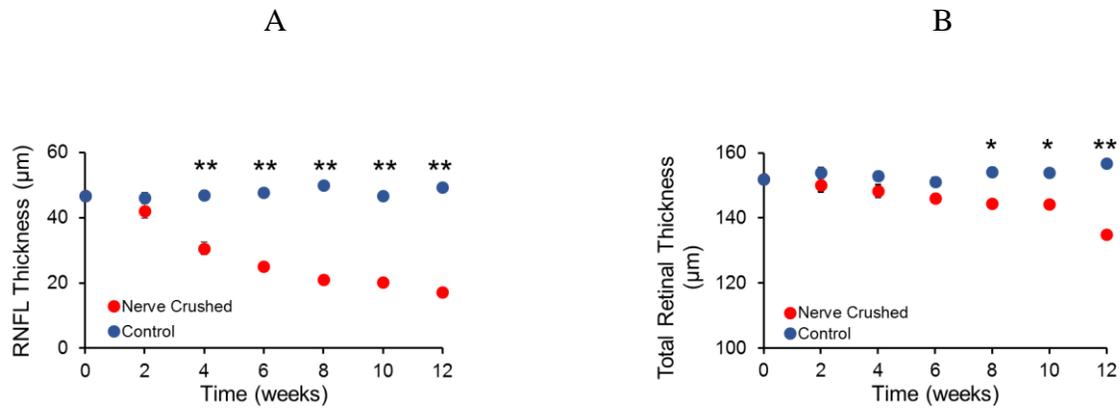


**Figure 4-3:** Retinal nerve fiber layer and total retinal thicknesses following optic nerve crush

A) Retinal nerve fiber layer (RNFL) thickness, and B) total retinal thickness for experimental (red) and control (blue) eyes from baseline to 12 weeks; \* =  $P < 0.05$  and \*\* =  $P < 0.01$  indicates a significant difference between experimental and control eyes

### 4.3.3 Full field flash ERG

Representative flash ERG responses for an experimental eye at baseline and at 10 weeks are shown in Figure 4-4A. Following optic nerve crush, there were no significant differences in the a- or b-wave amplitudes in experimental eyes compared to control eyes ( $P > 0.05$  for all, Figures 4-4B and 4-4C). Time to peak for a-waves, b-waves and PhNR was not affected by optic nerve crush. Mean baseline implicit times for a-wave, b-wave and PhNR were  $15.4 \pm 1.14$  ms,  $35.6 \pm 2.15$  ms and  $54.5 \pm 1.41$  ms respectively, and 10 weeks following the crush were  $16 \pm 1.76$  ms,  $32.7 \pm 1.85$  ms and  $58.3 \pm 6.64$  ms respectively. ( $P > 0.05$  for all). The PhNR amplitude in experimental eyes significantly decreased compared to control eyes 6 weeks following the nerve crush injury (repeated measures ANOVA, mean difference at 6 weeks =  $6.75 \pm 2.56 \mu\text{V}$ ,  $P < 0.01$ , Figure 4-4D).

Representative OPs before and 10 weeks after optic nerve crush are shown in Figure 4-5A. There was a significant decrease in OP1 amplitude in experimental compared to control eyes beginning 2 weeks following optic nerve crush (mean difference at 2 weeks =  $4.58 \mu\text{V} \pm 1.42$ ,  $P < 0.01$ , Figure 4-5B). However, there were no significant differences in OP2 and OP3 between the experimental and control eyes at any time point (Figures 4-5C and 4-5D). The relative timing of the OPs was unaffected by the crush. Mean baseline implicit times for OP1, OP2 and OP3:  $18.5 \pm 0.53$  ms,  $26.5 \pm 1.77$  ms, and  $36.5 \pm 1.92$  ms respectively, and mean implicit times 10 weeks following the crush for OP1, OP2 and OP3 were  $18.7 \pm 0.57$ ,  $27.3 \pm 1.52$ , and  $36.3 \pm 2.08$ , respectively ( $P > 0.05$  for all).

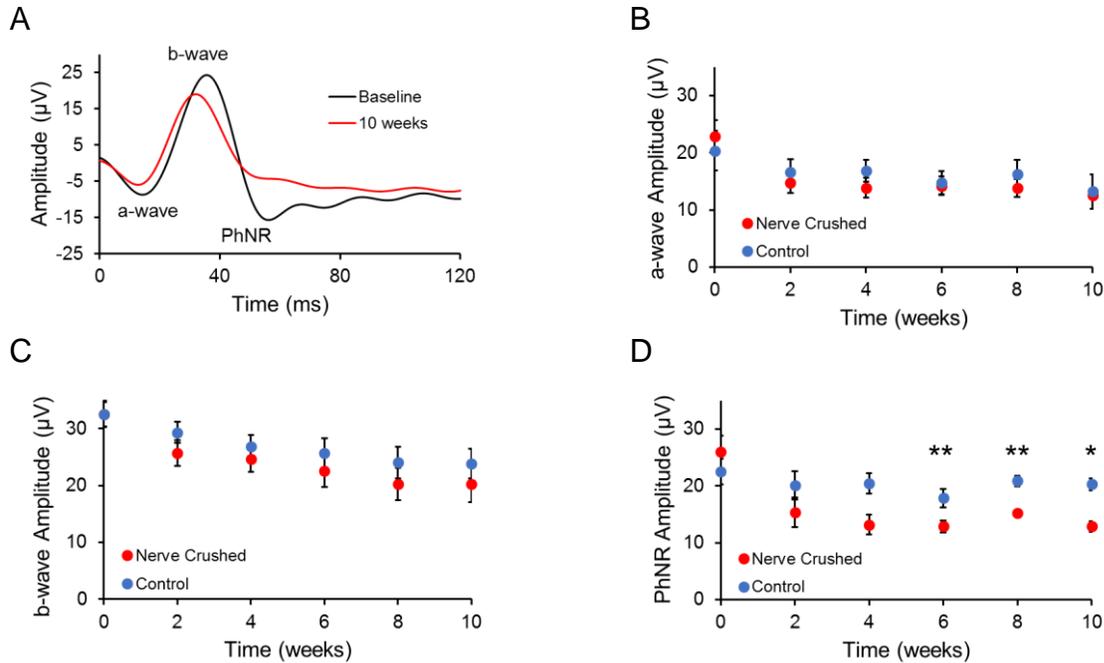


**Figure 4-4:** Results from flash ERG following optic nerve crush

A) Representative traces of flash ERG from one eye at baseline (black trace) and 10 weeks after optic nerve crush (red trace). B) A-wave, C) b-wave, and D) PhNR amplitudes ( $\mu\text{V}$ ) for optic nerve crush (red) and control (blue) eyes from baseline and up to 10 weeks following nerve crush injury; \* =  $P < 0.05$  and \*\* =  $P < 0.01$  indicate a significant difference between experimental and control eyes. Error bars represent standard error;  $n = 10$  at 0, 2 and 4 weeks,  $n = 9$  at 6 weeks,  $n = 7$  at 8 weeks, and  $n = 5$  at 10 weeks

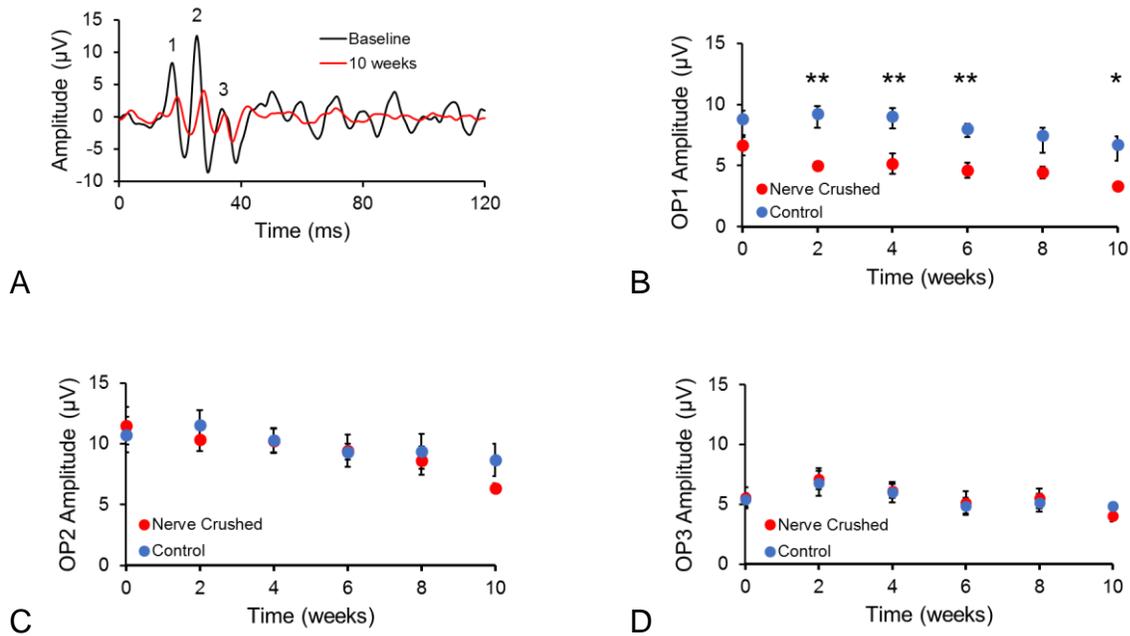


**Figure 4-5:** Results for oscillatory potentials following optic nerve crush

A) Representative traces of oscillatory potentials (OPs) from one eye at baseline (black trace) and 10 weeks after optic nerve crush (red trace). B) OP1, C) OP2, and D) OP3 amplitudes ( $\mu\text{V}$ ) for optic nerve crush (red) and control (blue) eyes from baseline and up to 10 weeks following nerve crush injury; \* =  $P < 0.05$  and \*\* =  $P < 0.01$  indicate significant differences between experimental and control eyes. Error bars represent standard error;  $n = 10$  at 0, 2 and 4 weeks,  $n = 9$  at 6 weeks,  $n = 7$  at 8 weeks and  $n = 5$  at 10 weeks

#### 4.3.3.2 Pattern ERG

Representative traces for pattern ERG to a 0.05 cpd square wave grating at 100% contrast and 1.05 Hz alternating frequency before and 10 weeks after optic nerve crush are shown in Figure 4-6 A. There were no significant differences in the amplitudes of N1P1 and P1N2 between the experimental and control eyes at baseline or at any point throughout the study ( $P > 0.05$  for all, Figures 4-6B and 4-6C).

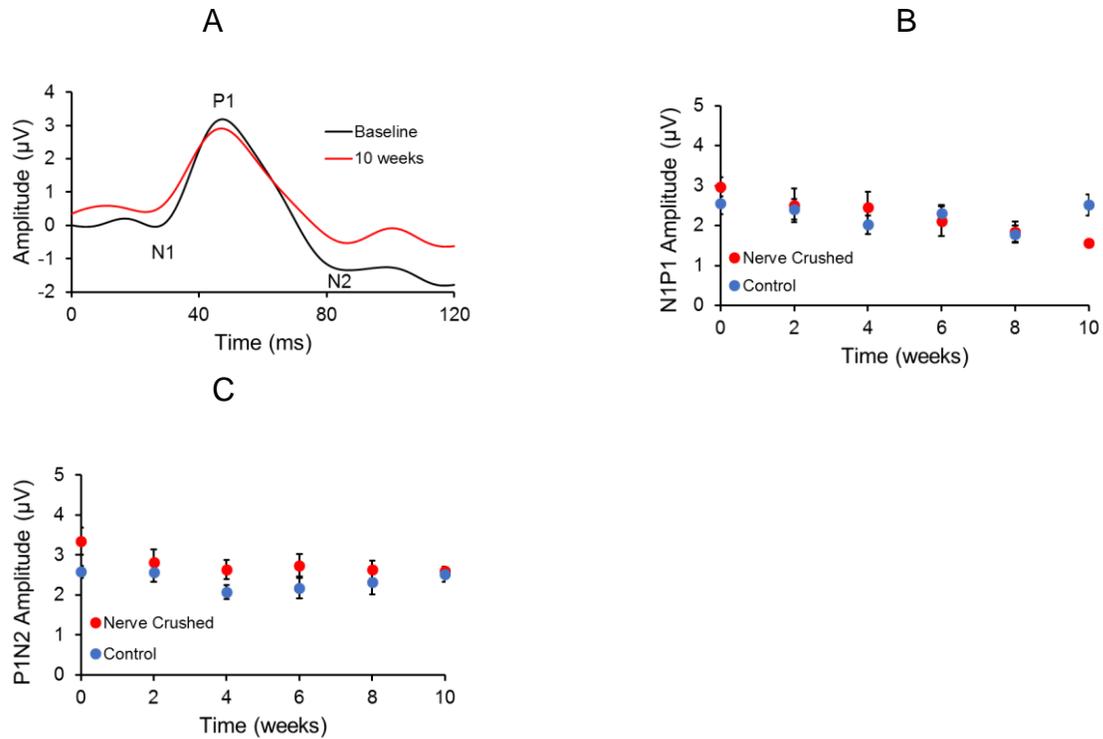


**Figure 4-6:** Results for pattern ERG following optic nerve crush

A) Representative raw trace of a pattern ERG from one eye at baseline (black trace) and 10 weeks after optic nerve crush (red trace); B) N1P1 and C) P1N2 amplitudes of the pattern ERG for optic nerve crush (red) and control (blue) eyes at baseline and up to 10 weeks following nerve crush injury. Error bars represent standard error;  $n = 10$  at 0, 2 and 4 weeks,  $n = 9$  at 6 weeks,  $n = 7$  at 8 weeks, and  $n = 5$  at 10 weeks

#### 4.3.4 Effects of GABA on the flash and pattern ERG

Intravitreal injections of GABA have been used to separate ERG waves (e.g. scotopic threshold response) generated by amacrine and ganglion cells that are subject to strong GABAergic inhibition for those originating from photoreceptors and bipolar cells that are less subject to the effects of inhibitory input. [Sieving and Naarendorp 1991 *Vis Res*, ; Saszik et al., 2002 *J. Physiol.*)

In general, GABA injection caused a reduction in the amplitude of the flash ERG and pattern ERG waves. In the flash ERG, there were significant reductions in the amplitudes of a-wave, and PhNR within 10 minutes following the intravitreal injections, while reduction in b-wave amplitude was not significant. At later times, the b-wave was significantly reduced in amplitude as well. There was significant reduction in the amplitude of a-wave, PhNR, OP1, OP2 and OP3 10 minutes following the intravitreal injections of GABA (table 4-2). Measurements at 30 minutes following the injection of GABA showed significant reduction in the N1P1 and P1N2 amplitudes of pattern ERG. Mean baseline amplitudes for N1P1 and P1N2 were  $2.55 \pm 1.03 \mu\text{V}$  and  $2.90 \pm 0.88 \mu\text{V}$  respectively; 30 minutes following the injection, they were reduced to  $1.75 \pm 1.18 \mu\text{V}$  and  $1.89 \pm 0.78 \mu\text{V}$  respectively,  $P < 0.05$  for both. There was no significant reduction in the amplitudes for N1P1 and P1N2 in the vehicle injected eyes. Mean baseline amplitudes for N1P1 and P1N2 were  $2.93 \pm 0.12$  and  $2.66 \pm 0.75$  respectively, 30 minutes following the injection, they were increased to  $3.43 \pm 0.11$  and  $2.93 \pm 0.11$  respectively,  $P > 0.05$  for both.

**Table 4-2:** Amplitude ( $\mu\text{V}$ ) of ERG waves before and 10 min after intravitreal injections of GABA in the left eyes of young guinea pigs (n=6)

<b>ERG wave</b>	<b>Pre-GABA Amplitude (<math>\mu\text{V}</math>)</b>	<b>Post-GABA Amplitude (<math>\mu\text{V}</math>)</b>	<b>P value</b>
a-wave	21.2 $\pm$ 6.05	10.91 $\pm$ 4.90	< 0.05
b-wave	30.2 $\pm$ 11.52	19.66 $\pm$ 7.52	0.24
PhNR	28.2 $\pm$ 12.29	20.33 $\pm$ 7.84	< 0.05
OP1	10.0 $\pm$ 3.03	4.5 $\pm$ 0.77	< 0.05
OP2	10.25 $\pm$ 2.78	4.5 $\pm$ 2.82	< 0.05
OP3	7.75 $\pm$ 2.99	3.33 $\pm$ 1.03	< 0.05

#### 4.3.5 In vitro retinal ganglion cell density

Representative images of retinal flat mount sections showing RBPMS labeled retinal ganglion cells in optic nerve crush and control eyes are shown in Figure 4-7. At 4 weeks, mean ganglion cell density was reduced by 78.1% in the optic nerve crush eye compared to contralateral control eyes. At 12 weeks, the mean percentage in ganglion cell density reductions for center, mid-periphery, and periphery in optic nerve crush eyes compared to control eyes were 89.8 %, 85.9 %, and 73.4%, respectively (Figure 4-8).

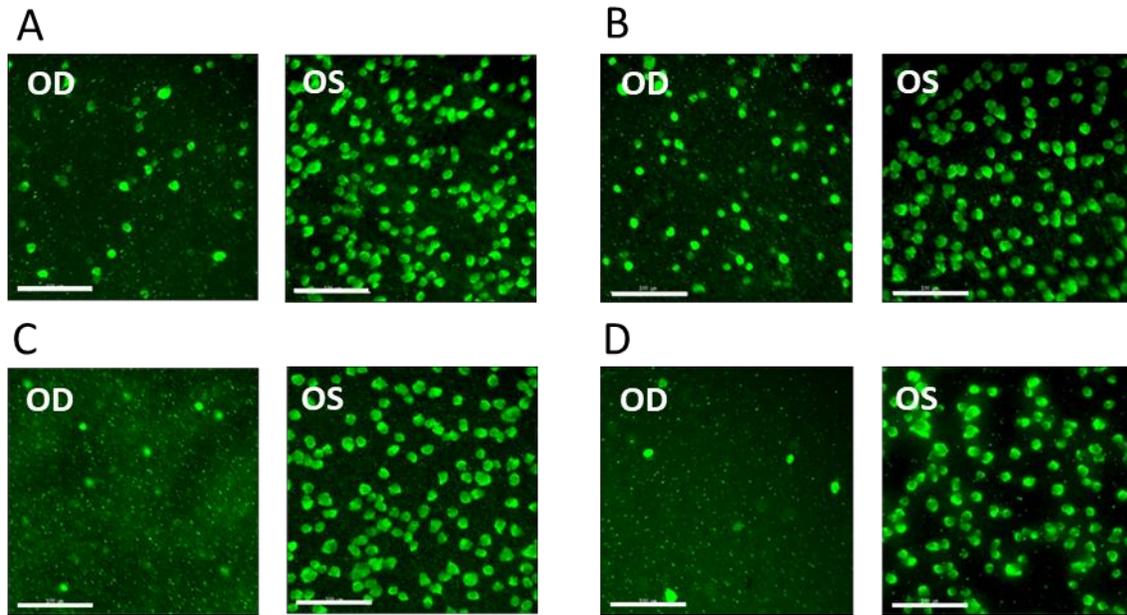


**Figure 4-7:** Representative images of retinal ganglion cells stained with RBPMS

A) 4 weeks, B) 6 weeks, C) 9 weeks, and D) 12 weeks in experimental (left panels) and contralateral control eyes (right panels) of the same animals. Images are from similar retinal locations, 7 mm inferior nasal retina from the optic nerve head center, for all eyes. Scale bar = 100  $\mu$ m

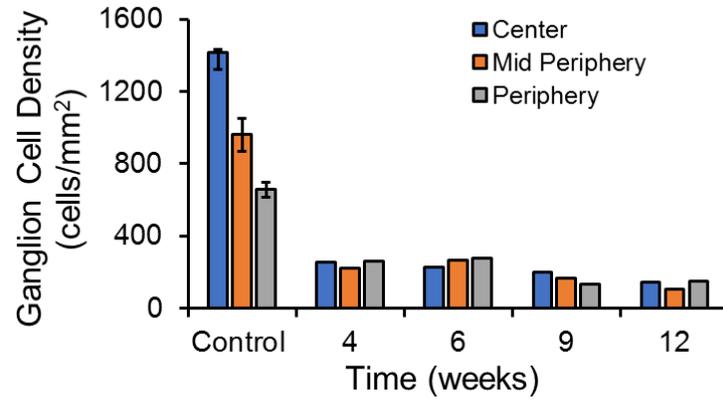


**Figure 4-8:** Retinal ganglion cell density from all control eyes (n = 7) and optic nerve crush eyes At 4 (n = 1), 6 (n = 2), 9 (n = 2), and 12 (n = 2) weeks for three retinal zones (central, mid-periphery,) periphery)

#### 4.4 Discussion

The goal of this study was to identify structural and functional markers of retinal ganglion cell loss in guinea pigs. We found strong evidence that retinal ganglion cells contribute to the photopic negative response (PhNR) of full field flash ERGs, similar to observations in primates<sup>69, 70</sup> but a smaller proportion of the response. Oscillatory potential 1 (OP1) amplitude was also reduced. Additionally, we found that the pattern ERG in guinea pigs to be independent of retinal ganglion cell loss. Structural losses were observed as substantial *in vivo* thinning of the retinal nerve fiber layer and *in vitro* decreases in retinal ganglion cell density.

The PhNR has been shown to be of retinal ganglion cell origin in mammals, including non-human primates, humans, and in several studies, rodents.<sup>69-71</sup> However, the presence of the PhNR in guinea pigs has not been reported previously. Recent studies have found a strong correlation of PhNR amplitude to structural changes, such as with retinal nerve fiber layer thinning in humans.<sup>197, 198</sup> In this study, we identified the PhNR of the full field flash ERG in all animals. Following optic nerve crush, there was a significant reduction in PhNR amplitude from baseline at 6 weeks. However, there were no changes in a- and b-wave amplitudes, suggesting relative preservation of outer retina despite the optic nerve crush injury. The effect on the PhNR with ganglion cell degeneration in mice has been variable. Chrysostomou et al., showed that PhNR of the full field ERG was sensitive to intraocular pressure elevation in mice, and reduced by approximately 70% from baseline within a week of intraocular pressure elevation.<sup>71</sup> They suggested that inner retinal responses from retinal ganglion cells and retinal glia were the likely contributors for PhNR component of ERG in mice. However, another study by Liu, et al showed no significant change in the PhNR amplitude in mice, even after four weeks following optic nerve crush, although there was a trend towards reduction of the PhNR amplitude.<sup>61</sup> In rats, significant reduction of PhNR

amplitude was observed as early as 24 hours following optic nerve transection, reaching a maximum reduction of 56% after 15 weeks.<sup>72</sup> Similar to these results from mice and rats, we found that the PhNR in guinea pigs is not entirely dependent on the retinal ganglion cell integrity, as even at 10 weeks following optic nerve crush, a measurable PhNR was still present (64% reduction from baseline). This suggests that while retinal ganglion cells appear to have a significant contribution to the PhNR component in guinea pigs, the PhNR may receive contributions from other retinal cells, as it was never abolished completely even when there was major loss ganglion cell loss through the retina (Figure 4-8). Other neural contributions could be from amacrine cells, and studies in the non-human primate and rat have suggested that glial cell also contribute to the PhNR,<sup>69, 199</sup> which may be the case in guinea pigs as well.

The oscillatory potentials (OPs) are small rhythmic wavelets superimposed on the ascending limb of the b-wave of the ERG.<sup>200</sup> The retinal source of origin of OPs is not well understood, although it is thought they have an inner retinal origin.<sup>200</sup> Pharmacological experiments in mudpuppy show that GABA mediated presumably inner retinal pathways contribute to the OPs,<sup>201</sup> and there were similar observations in photopic ERG of nonhuman primates.<sup>202</sup> Dong, et al. suggested that the early OPs may be generated by outer retina, while the intermediate and late OPs are generated by action-potential independent and dependent mechanisms in the ON pathway of the inner retina, respectively.<sup>203</sup> In contrast, we found that OP1 was significantly reduced in the experimental eyes compared to contralateral control eyes, whereas OP2 and OP3 were unaffected, suggesting that in guinea pig, OP1 depends on the integrity of retinal ganglion cells while OP2 and OP3 receive input from other retinal neurons.

GABA is the major inhibitory neurotransmitter in the retina.<sup>204, 205</sup> GABA receptors are found throughout the retina and particularly in the inner retina on amacrine and ganglion cells, but

also in cells such as bipolar cells (especially the axon terminals), horizontal cells.<sup>206, 207</sup> Previous studies in cats (SN VR 91) and mice (S JP 20020) selectively suppressed waves originating from amacrine and ganglion cells, the scotopic threshold response. In contrast, intravitreal injections of GABA in guinea pigs, significantly reduced the amplitudes of all components of the flash ERG except b-waves. Reductions occurred in the OPs, a-wave and PhNR as early as 10 minutes following the injection and progressed with time (not shown). Similarly, there was significant reduction in the N1P1 and P1N2 amplitude of the pattern ERG when they were assessed at 30 minutes following the injection. . Complete loss of OPs with intravitreal GABA injections have been demonstrated in mudpuppy retina, while the b-wave amplitude remained unaffected.<sup>201</sup> An increase in b-wave amplitude in cat and mouse has also been demonstrated (Naarendorp, Saszik). Given the general amplitude reduction caused by the GABA injections in guinea pigs, it was not possible to gain insight about the inner or outer retinal origins of the different waves in the flash and pattern ERGs.

The pattern ERG has been shown to be a direct measure of the functional integrity of retinal ganglion cells in the mammalian retina, including cats, rats, mice, non-human primates and humans.<sup>74, 100, 101, 124</sup> In this study, although trends indicated some reduction in P1N2 component of the pattern ERG in experimental eyes from baseline, the changes were not significant. Likewise, there were no significant changes in the N1P1 component of the pattern ERG. The pattern ERG has also been shown to be unaffected by ganglion cell degeneration in non-mammalian species, such as chicks.<sup>106</sup> In animals in which pattern ERGs originate from retinal ganglion cells, linear signals from outer retina presumably cancel in response to the alternating pattern stimuli. It is possible that there are signals originating from the outer retina in response to the patterned stimulation in guinea pig retina that do not be fully cancel. This non linearity of signals from the

outer retina might be the reason for the persistence of the pattern ERG despite ganglion cell loss in guinea pigs. Further studies using pharmacological techniques to block activity of specific cells and pathways may help to obtain more information about the origin of pattern ERG in guinea pigs.

We found the guinea pig pattern ERG responses to be of small amplitude, on the order of a 2-4  $\mu\text{V}$  for both N1P1 and P1N2. Like photopic flash ERG waves, the pattern ERG is also much smaller in amplitude in guinea pigs compared to those of mice and rats; peak P1N2 amplitude for mice and rat have been reported to be approximately 20  $\mu\text{V}$  and 10  $\mu\text{V}$ , respectively.<sup>74, 122</sup> Differences in amplitude across studies may be attributable in part to differences in properties of recording electrodes. Comparisons of pattern ERGs by more standard electrodes to the Celeris, which uses integrated electrodes, have not been made. In addition to their small amplitude, these responses in guinea pigs were highly variable. One potential source of variation could be related to alignment of the pattern stimulus with the visual streak of the guinea pig which is located in the superior retina.<sup>111</sup> While we attempted to align the stimulus probe with the visual axis, which would allow the 4 mm x 4.6 pattern stimulus to overlap the visual streak, small misalignments could have contributed to variable response amplitudes. Other recording conditions were strictly maintained between sessions; the right eye was always recorded first, followed by the left eye, and all sessions began with pattern ERG followed by flash ERG, and then the OCT imaging.

We used optomotor responses to assess behavioral visual function of guinea pigs before and after optic nerve crush. The optomotor response is simple, unlearned reflex turning of the head and neck to follow the rotation of a global visual pattern drifting in the horizontal plane.<sup>208</sup> Behavioral assessment of vision in rodents with optomotor responses is a well-established technique that allows rapid, non-invasive evaluation of visual discrimination.<sup>78, 79, 114</sup> Optomotor responses have been shown to be reduced or missing in rodent models of ganglion cell

degeneration, such as glaucoma.<sup>209, 210</sup> Here, we found total loss of optomotor responses in experimental eyes soon after optic nerve crush, confirming that the procedure was effective in causing axonal damage and preventing communication between the retina and higher brain centers.

OCT is a non-invasive *in vivo* imaging technique used to assess retinal structure. OCT imaging is often used to monitor the progression of retinal structural changes such as thinning of retinal layers in glaucoma.<sup>56, 137, 211</sup> In rodents, OCT has been used to evaluate retinal thinning in glaucoma and optic nerve crush and transection.<sup>61, 190</sup> Optic nerve crush and transection are disease models for traumatic optic neuropathy and glaucoma.<sup>212</sup> These optic nerve injuries induces retrograde apoptotic degeneration of retinal ganglion cell axons and cell bodies,<sup>192, 213</sup> resulting in thinning of the retinal nerve fiber layer.<sup>214, 215</sup> Here, we found progressive thinning of ganglion cell nerve fiber layer, first noted four weeks following optic nerve crush. Although some animals showed reduction even at two weeks following the crush, some animals showed initial thickening of inner retina following the crush. Transient thickening of the retina following optic nerve crush has been reported in previous studies, with a possible role of edema due to inflammatory response to the nerve crush injury.<sup>190</sup> We found significant retinal nerve fiber layer thinning of 35% from baseline four weeks following optic nerve crush. Using OCT, Munguba et al., reported an approximately 20% reduction from baseline in retinal nerve fiber layer thickness in mice following optic nerve crush.<sup>191</sup> However, in guinea pigs ganglion cell bodies are interspersed with ganglion cell axons in the nerve fiber layer,<sup>194</sup> which may have contributed to a greater loss of thickness than reported in mice. Additionally, the guinea pig retina is avascular, so results in guinea pigs may vary from those of other rodent models which possess inner retinal vasculature, as the mechanisms of changes following the optic nerve crush might be different. Total retinal thickness decreased in experimental eyes of all animals, which was significant at 8 weeks following the

crush, reflecting the loss of retinal nerve fiber layer thickness, although underestimating it, as the percentage reduction in total retinal thickness was less than that in retinal nerve fiber layer thickness. Furthermore, the a- and b-waves from the flash ERGs did not show significant changes in the experimental eyes, which suggests that the integrity of the outer retina was maintained in the nerve crush eyes.

We found that *in vivo* OCT imaging was valuable to detect and monitor progressive loss of nerve fiber layer in the guinea pig. *In vivo* imaging allows for monitoring of progressive retinal structural changes without the need to sacrifice the animal, thus reducing the number of animals required to obtain information about structural changes. Although approximately 78% of retinal ganglion cells were lost within 4 weeks following optic nerve crush, the retinal nerve fiber layer thickness was reduced by only about 35% at that time. A maximum reduction in thickness of 65% was observed at 12 weeks following nerve crush injury. Such lag of retinal nerve fiber layer thinning compared to retinal ganglion cell loss has also been reported in mouse model of optic nerve crush,<sup>191</sup> which can be explained by the fact that OCT measures the total space occupied by the retinal ganglion cell soma, axon, and dendrites, as well as glial elements for the retinal nerve fiber layer measurements while the retinal ganglion cell loss as suggested by the reduction in ganglion cell density represents loss of retinal ganglion cell soma only. Retinol binding protein with multiple splicing (RBPMS), used here to selectively label the retinal ganglion cells, has been shown to be highly selective for retinal ganglion cells in the mammalian retina including mice, rats, rabbit and guinea pigs.<sup>125</sup> In the guinea pig retina, approximately 55% of the cells in the ganglion cell layer are retinal ganglion cells, the rest are amacrine cells.<sup>111</sup>

Fluorescein angiography, a common clinical tool, has been used in mice and rats to evaluate the retinal vasculature.<sup>216, 217</sup> In this study, we used fluorescein angiography to assess the

integrity of choroidal vasculature following nerve crush, which is essential to the health of the retina. Because the guinea pig inner retina is avascular, all nutrients are likely supplied by the choroidal vasculature through diffusion.<sup>178</sup> We were able to visualize a small vascular tuft at the optic nerve head of guinea pigs in our angiography images, which are most likely the central retinal artery coming from the ophthalmic artery. This vascular tuft is limited to the optic nerve head and does not supply the retina.

#### ***4.5 Conclusions***

In conclusion, we demonstrated that retinal ganglion cell loss in the guinea pig can be assessed non-invasively using OCT, optomotor responses, and ERG. Findings support a retinal ganglion cells contribution to the PhNR and OP1 wave of full field flash ERG in guinea pigs. The presence of the PhNR and its dependence on retinal ganglion cell integrity in guinea pigs suggests that full field flash ERG may be a useful tool to assess inner retinal function in this animal model.

#### **Acknowledgements**

Thanks to Alan Burns for help with Delta Vision imaging, Krista Beach for help with immunohistochemistry, Jason Marsack for creating custom contact lenses, Chris Kuether for constructing the custom stages, John Bauer for help with constructing the custom optokinetic drum, and Alex Schill for help with calibration of the PERG stimulus.

Grant information: This work was supported by NIH NEI K08 EY022696 and NIH NEI P30 EY007551

## **CHAPTER 5: THE OPTIC NERVE HEAD, LAMINA CRIBROSA, AND NERVE FIBER LAYER IN NON-MYOPIC AND MYOPIC CHILDREN**

Ashutosh Jnawali, Hanieh Mirhajianmoghadam, Gwen Musial, Jason Porter, Lisa A Ostrin

Published in Experimental Eye Research. 2020 Apr 28;195:108041.

### ***5.2 Introduction***

Optic nerve head assessment is important in the evaluation and diagnosis of a number of ocular conditions, including myopia, glaucoma, and optic nerve edema, which result in structural changes in the posterior globe. However, there is significant variation in optic nerve head structure within the normal population,<sup>218-220</sup> which can make the evaluation of such ocular conditions difficult. Along with the optic nerve head, other ocular structures, such as the retinal nerve fiber layer, peripapillary sclera, and choroid, have also been found to have significant variation in the normal population.<sup>22, 221, 222</sup>

Several studies have focused on characterizing optic nerve head structure and the lamina cribrosa in healthy and pathological eyes of adults. The lamina cribrosa is a collagenous sieve-like structure located within the optic nerve head that provides structural support to the retinal ganglion cell axons and vasculature passing in and out of the eye.<sup>223</sup> Histological and *in vivo* studies in humans and non-human primates have demonstrated variability in the depth and thickness of the lamina cribrosa and size of laminar pores and collagenous beams in healthy eyes.<sup>40, 224, 225</sup> Histological studies in adult human eyes have shown that the lamina cribrosa is thinner in eyes with high myopia or increased axial length.<sup>24, 226</sup> With the advent of *in vivo* optical coherence tomography with enhanced depth imaging, it has become possible to better evaluate lamina cribrosa structure, such as depth and tilt angle, non-invasively.<sup>129, 227</sup> With *in vivo* imaging, Yun, et al. found that the lamina cribrosa was thinner in eyes with longer axial lengths. The authors also

reported that lamina cribrosa depth was associated with axial length in adults with glaucoma, but not in healthy eyes.<sup>50</sup> While some studies have reported that *in vivo* lamina cribrosa structure is associated with age and refractive error,<sup>228, 229</sup> Lee, et al. found that lamina cribrosa thickness in adults was not associated with axial length.<sup>230</sup>

Choroidal and retinal nerve fiber layer thickness have also been shown to be associated with refractive error.<sup>21, 22, 231</sup> Thinner choroids, both in the foveal and peripapillary regions, have been reported in myopic children and adults compared to non-myopes.<sup>21, 22, 52, 232, 233</sup> Additionally, studies have reported thinning and redistribution of the peripapillary retinal nerve fiber layer with myopia.<sup>211, 221, 234</sup> However, conflicting results exist, with some studies suggesting that associations of the retinal nerve fiber layer thickness with refraction and axial length disappear after correcting for magnification effects related to the imaging modality.<sup>53, 235</sup> These studies demonstrate the importance of scaling images based on ocular biometry to draw correct conclusions on the relationship between retinal nerve fiber layer thickness with axial length and refractive error.<sup>236</sup>

There is little information on optic nerve head structure and the lamina cribrosa in children. Investigations of ocular structure in children are important because significant growth and remodeling are known to occur in childhood, which may provide insight to the processes of emmetropization<sup>82, 83</sup> and myopia development.<sup>84</sup> The goal of this study was to assess the optic nerve head, retina, and choroid in healthy school age children as a function of age, axial length, and refraction to understand how these structures vary towards the end of the emmetropization process and when school age myopia is known to onset and progress.

### **5.3 Methods**

#### **5.3.1 Subjects**

Children, ages 6 to 15 years, were recruited for this cross-sectional study. Exclusion criteria were ocular pathology, corneal opacities, cataracts, posterior segment anomalies, and contraindications for dilation. Parental permission and children's assent were acquired prior to enrollment. The study was approved by the Institutional Review Board at the University of Houston and followed the tenets of the Declaration of Helsinki.

Before participation, all children underwent slit lamp examination to confirm eligibility. Best corrected visual acuity was assessed monocularly in both eyes with a Snellen letter chart. Eyes were dilated with topical instillation of one drop each of 1% tropicamide (Henry Schein Inc., NY USA) and 2.5% phenylephrine (Paragon Bio Teck Inc., OR USA). Intraocular pressure was measured with a rebound tonometer (ICare Tiolat Oy, Helsinki, Finland). Three readings were recorded for each eye, with each reading being an average of six measures.

Optical biometry was performed on each eye (Lenstar, LS 900, Hagg-Streit, Germany) to determine anterior corneal curvature, central corneal thickness, anterior chamber depth, lens thickness, and axial length. Five measurements were acquired for each eye and averaged. Cycloplegic autorefractometry was performed with a Grand-Seiko autorefractor (WAM-5500, Shigiya Machinery Works Ltd., Hiroshima, Japan). At least five measurements were recorded and averaged for each eye. The mean spherical equivalent refractive error (SER) was calculated and used to categorize study participants into refractive error groups; the non-myopic group included  $SER \geq -0.50$  D and the myopic group included  $SER < -0.50$  D.

### 5.3.2 Image Acquisition

*In vivo* imaging was performed on both eyes of each subject with spectral domain optical coherence tomography (SD-OCT, Spectralis HRA+OCT; Heidelberg Engineering, Heidelberg, Germany). Scans were acquired using high resolution mode with an acquisition rate of 38,400 A-scans per second and a super luminescent diode light source with a central wavelength of 880 nm. As per the manufacturer, the instrument's axial resolution was 3.5  $\mu\text{m}$ /pixel digital (7  $\mu\text{m}$  optical), and lateral resolution was 6  $\mu\text{m}$ /pixel digital (14  $\mu\text{m}$  optical). To acquire images, subjects were seated comfortably at the instrument and instructed to place their head on the chin and forehead rests, viewing the internal fixation target with the eye being scanned. The protocol included three scans of each eye; 1) a 48-line radial scan (20°, 1024 A-scans per B-scan, Figure 1A), 2) a 12° peripapillary circular scan (1536 A-scans, Figure 1B) centered at the optic nerve head, and 3) a 97-line macular volume scan (20° x 20°, 1024 A-scans per B-scan, Figure 1C). Enhanced depth imaging mode was used for radial scans to better visualize deeper structures, including the choroid and lamina cribrosa surface. For optimum noise reduction and image quality, averaging was set to 100 frames per B-scan for the peripapillary circular scan, 16 frames per B-scan for the radial scan, and 9 frames per B-scan for the macular volume scan. Image quality for all scans was greater than 30 dB.

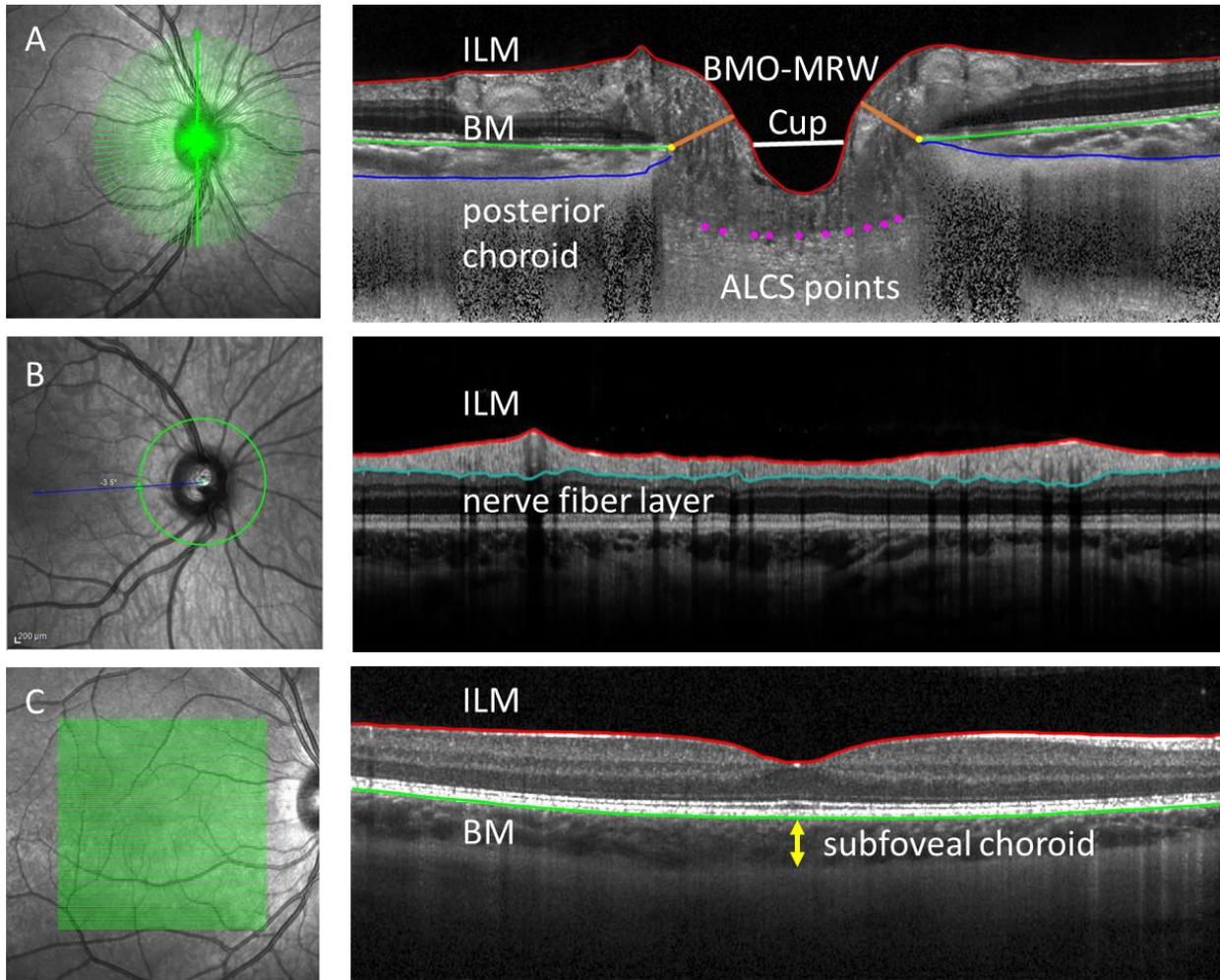


**Figure 5-1:** Representative SLO images and corresponding b-scan images from OCT scans

A) Optic nerve head radial scan, B) optic nerve head circular scan, and C) macular volume scan (green lines) overlaid on the scanning laser ophthalmoscope (SLO) images. Corresponding SD-OCT B-scans for each scan type are shown adjacent to each SLO image. Segmentation included inner limiting membrane (ILM, red), nerve fiber layer (teal), Bruch's membrane (BM, green), posterior choroid (blue), Bruch's membrane opening (BMO, yellow), Cup (white), minimum rim width (MRW, orange), and anterior lamina cribrosa surface points (ALCS, magenta)

### 5.3.3 Image analysis

#### 5.3.3.1 Optic Nerve Head Radial Scan

For the radial scan centered on the optic nerve head, images were exported as raw (.vol) files and analyzed with a custom MATLAB program (MATLAB, Mathworks, Inc., Natwick, MA). Scans were laterally scaled using biometric data collected from each eye and a four surface schematic eye.<sup>237, 238</sup> The model assumes four major refractive surfaces – anterior and posterior cornea and anterior and posterior lens. Input parameters included axial length, average anterior corneal radius of curvature, anterior chamber depth, and lens thickness. Corneal thickness was a constant. To modify the schematic eye for children, previously published values of the anterior and posterior radii of curvature of the lens based on the age of each child were used, which were obtained using equations 1 and 2.<sup>239</sup>

$$\text{Equation 1: lens anterior radius of curvature (mm)} = -0.021 x^2 + 0.151 x + 11.45$$

$$\text{Equation 2: lens posterior radius of curvature (mm)} = 0.004 x^2 + 0.063 x + 6.236$$

where  $x = (\text{age in years} - 10)$

The perpendicular direction for axial scaling was based on refractive index and interference of the components of the ocular media and was taken as  $3.87 \mu\text{m}/\text{pixel}$ .

For each B-scan image, segmentation errors for the internal limiting membrane (ILM) were manually corrected. For enhanced visualization of Bruch's membrane and the lamina cribrosa, adaptive compensation algorithms were applied to remove shadows and recover signals from the bottom of the image, as described previously.<sup>240</sup> The termination of Bruch's membrane was marked manually on each side of the optic nerve head to determine Bruch's membrane opening (BMO). Image processing for radial scans is shown for a representative B-scan image in Figure 1A. BMO-based minimum rim width (MRW) was calculated for each B-scan as the minimum

(perpendicular) distance from the BMO point to the ILM, and the average MRW from all 48 line scans was used as the mean MRW for each eye. BMO diameter and area were calculated by fitting an ellipse through the 96 BMO points.<sup>241</sup> The location of the cup on each B-scan was defined as the point of intersection of the line joining two BMO points and the ILM. Cup diameter was calculated in the horizontal and vertical meridians. Anterior lamina cribrosa surface (ALCS) points were marked manually on each B-scan. Using these points, a thin plate spline surface was fit to generate the ALCS plane in three dimensions, using algorithms described previously.<sup>241</sup> A reference plane was fit over the BMO points, and the average of the distance from the BMO reference plane to the ALCS plane was used as the mean ALCS depth (ALCSD) for each eye.

For peripapillary choroidal thickness measurements, 12 of the 48 radial scans at equal intervals were analyzed. For each B-scan, segmentation errors for the ILM and Bruch's membrane were manually corrected. The posterior border of the choroid, represented by the choroid-sclera interface, was manually segmented. Thickness maps were generated for the peripapillary choroid with the method of interpolation, for all points between the 12 radial scans.<sup>194</sup> To measure the choroidal thickness at the same distance from the BMO points for all subjects, a total of 96 points at a distance of 1.7 mm from the BMO points on either side were selected, and an ellipse was fit over those points (Figure 2). A distance of 1.7 mm was chosen for analysis as this was the furthest distance we could measure peripapillary choroidal thickness from the BMO points in all subjects based on our calculations for lateral magnification and scan length for radial scans. After calculations for magnification effects, this distance was approximately 2.5 mm from the center of the optic nerve head. The thickness of the peripapillary choroid within the ellipse was calculated from the choroidal thickness maps for global and sectoral (temporal, superior, nasal and inferior) measurements for all subjects. The optic nerve head was excluded by applying a mask calculated

from the BMO diameter. This method allowed for measurement of peripapillary choroidal thickness at the same distance from the BMO in all subjects, thus reducing the possibility of variation in thickness with different distances from the BMO margin and varying effects of lateral magnification between myopes and non-myopes.

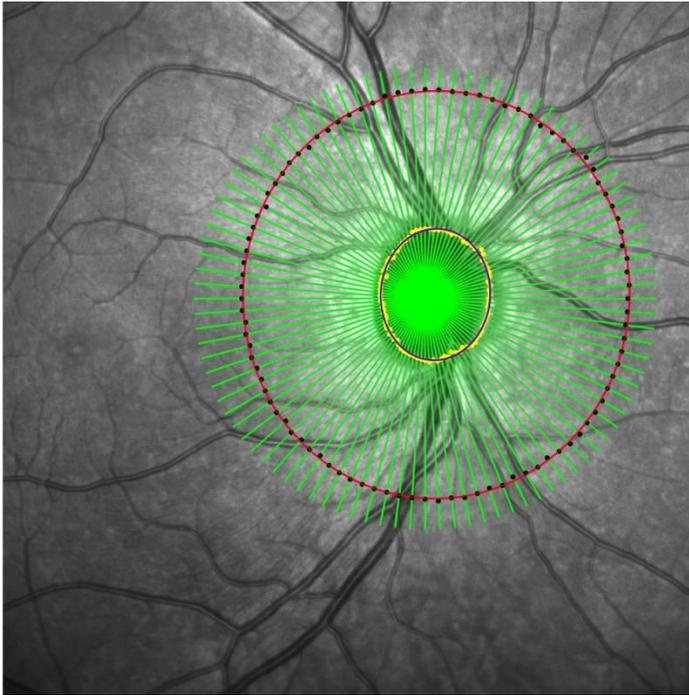


**Figure 5-2:** Representative SLO image with 48 line radial scans (green)

The blue ellipse at the center represents the BMO ellipse fit over the BMO points (yellow dots). Black symbols represent the newly selected points at a distance of 1.7 mm from the BMO points for each line scan. The larger red ellipse towards the edge represents the adjusted ellipse fit over the newly selected points.

### 5.3.3.2 Optic Nerve Head Circular Scan

For the circular scan centered on the optic nerve head, images were analyzed for peripapillary retinal nerve fiber layer (RNFL) thickness using the SD-OCT instrument's built-in software. Segmentation errors for the ILM and RNFL were manually corrected, and global and sectoral thickness values were provided by the software. The global and sectoral RNFL thicknesses obtained from peripapillary circular scans were further compensated for ocular magnification using methods described previously.<sup>59</sup> Briefly, the transverse scaling obtained from the schematic eye calculation was used to calculate the scan circumference using Equation 3:

*Equation 3:* calculated scan circumference =  $2\pi r$ , where  $r$  is the scan radius in microns obtained from the transverse scaling

This information was used to scale RNFL thickness using Equation 4 and a nominal scan circumference of 10.9 mm for an emmetropic eye.<sup>59</sup>

*Equation 4:* scaled RNFL thickness

$$= \frac{\text{RNFL thickness } (\mu\text{m}) \times \text{calculated scan circumference (mm)}}{10.9 \text{ mm}}$$

### 5.3.3.3 Macular Volume Scan

For the macular volume scan, images were also analyzed using the instrument's software. Segmentation errors for the ILM and Bruch's membrane were manually corrected, and measurements were obtained from the thickness map generated by the instrument, including minimum foveal thickness, retinal thickness within the central 1 mm diameter, and retinal thickness for each quadrant within the 6 mm annulus surrounding the central 1 mm (Figure 3). To measure subfoveal choroidal thickness, the line scan passing through the fovea was identified on the OCT instrument, the image was adjusted to a 1:1 aspect ratio, and the built-in caliper in the

instrument was used to determine the thickness from Bruch's membrane to the choroid-sclera interface. Subfoveal choroidal thickness was measured by two observers (AJ and HM) who were masked to the refractive status of the subject to assess interobserver variability.

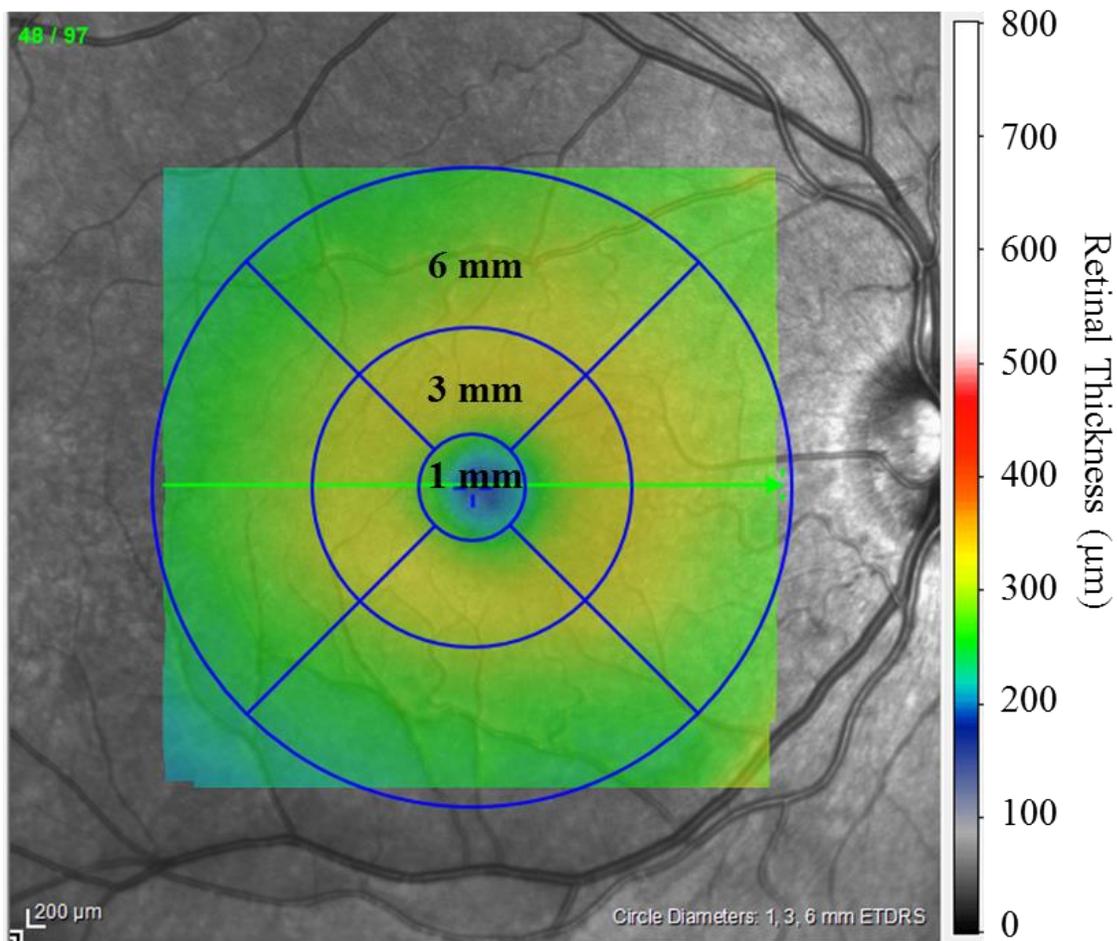


**Figure 5-3:** Representative macular volume scan thickness map

The regions that were analyzed (1 mm diameter, and 6 mm annulus) are overlaid on the corresponding SLO image

#### 5.3.4 Statistical Analysis

All right eyes were analyzed for the study. A subset of left eyes (n=16) were selected from the study population using a random number generator in MS Excel to perform interocular comparisons. Biometric parameters between the two refractive groups were assessed with unpaired t-tests. Statistical analysis was performed using SPSS (IBM Corp., Armonk, N.Y., USA). Data are expressed as mean  $\pm$  standard deviation. Normality of data was assessed with a Shapiro-Wilk test. The relationship of age with axial length and refractive error was assessed with simple linear regression. The associations of retinal, choroidal, and optic nerve head parameters with axial length and refractive error were assessed with a multiple linear regression, and variables were adjusted for age as an independent variable. Repeated measures ANOVA was used to assess the retinal, RNFL, and choroidal thicknesses by sector (within subjects factor) and refractive error group (between subjects factor), with post-hoc pairwise Bonferroni comparisons. Interocular symmetry for ocular parameters was assessed using the coefficient of variation and intraclass correlation coefficient. As subfoveal choroidal thickness was measured manually and tends to show increased variability compared to other measures, this parameter was measured by two independent observers (AJ and HM), and the coefficient of variation and intraclass correlation coefficient were calculated.

### **5.4 Results**

#### 5.4.1 Subjects

Subject characteristics are shown in Table 1. Fifty-three children participated, including 30 males and 23 females. However, we excluded one subject from the analysis, whose SER was

determined to be an outlier using the Tukey outlier test (SER = +7.22 D). The results are presented for the remaining 52 subjects. Mean subject age was  $11.2 \pm 2.61$  years. All subjects had a best corrected visual acuity of 20/20 or better.

Mean SER for right eyes ( $n = 52$ ) was  $-0.31 \pm 1.80$  D (range -5.43 to +5.37 D), and for left eyes ( $n = 52$ ) was  $-0.34 \pm 1.84$  D (range -5.55 to +5.12 D). SER was similar for right and left eyes ( $P = 0.94$ ). The following primary analyses were done on right eyes only. Mean age for the myopic group was significantly older than the non-myopic group ( $12.43 \pm 2.31$  years vs  $10.17 \pm 2.45$  years,  $P < 0.01$ ). The myopic group exhibited a greater axial length ( $P < 0.0001$ ), deeper anterior chamber ( $P < 0.01$ ), and a thinner crystalline lens ( $P < 0.05$ ), compared to the non-myopic group. Linear regression analysis revealed that age was associated with axial length and refractive error; axial length increased with age ( $R^2 = 0.25$ ,  $P < 0.0001$ ) and mean SER became more myopic ( $R^2 = 0.27$ ,  $P < 0.001$ ).

**Table 5-1:** Subject characteristics and biometry (n = 52); P values are shown for unpaired t-tests between non-myopes (n = 29) and myopes (n = 23)

	<b>All Subjects (n = 52)</b>	<b>Non-Myopes (n = 29)</b>	<b>Myopes (n = 23)</b>	<b>P value</b>
Age (Years)	11.12 ± 2.64	10.16 ± 2.48	12.43 ± 2.31	0.001*
Sex (M:F)	29:23	17:13	13:10	n/a
Spherical Equivalent Refractive Error (D)	-0.37 ± 1.85	+0.84 ± 1.12	-1.89 ± 1.41	< 0.0001*
Axial Length (mm)	23.63 ± 0.94	23.11 ± 0.76	24.29 ± 0.70	< 0.0001*
Central Corneal Thickness (µm)	558.32 ± 32.70	564.37 ± 33.17	551.66 ± 31.74	0.15
Corneal Curvature (mm)	7.78 ± 0.26	7.80 ± 0.24	7.74 ± 0.28	0.34
Anterior Chamber Depth (mm)	3.75 ± 0.30	3.64 ± 0.25	3.89 ± 0.29	0.002*
Lens Thickness (mm)	3.39 ± 0.16	3.44 ± 0.14	3.34 ± 0.17	0.02*
Intraocular Pressure (mmHg)	15.60 ± 2.97	15.54 ± 3.41	16.05 ± 2.80	0.61

\* = significance at  $P < 0.05$

#### 5.4.2 Optic Nerve Head and Lamina Cribrosa Structure

The relationships between optic nerve head parameters with axial length and SER, adjusted for age, are summarized in Table 5-2. The data for cup-to-disc ratio is shown for 38 subjects as the cup could not be demarcated on 14 subjects. A representative point cloud derived from the 48-line radial scan is shown in Figure 4. BMO diameter increased significantly with increasing axial length ( $R^2 = 0.07$ ,  $\beta = 0.05$ ,  $P = 0.05$ ) and increasing myopic SER ( $R^2 = 0.12$ ,  $\beta = -0.04$ ,  $P < 0.01$ ), and BMO area significantly increased with increasing myopic SER ( $R^2 = 0.16$ ,  $\beta = -0.09$ ,  $P < 0.01$ ), suggesting eyes with increasing myopia have larger disc sizes. Although there was a trend of increasing BMO area with axial length, it did not reach significance ( $R^2 = 0.07$ ,  $\beta = 0.12$ ,  $P = 0.06$ ). Vertical cup-to-disc ratio significantly decreased with increasing axial length ( $R^2 = 0.12$ ,  $\beta = -0.05$ ,  $P < 0.05$ ) and myopic SER ( $R^2 = 0.11$ ,  $\beta = 0.03$ ,  $P = 0.05$ ). Mean MRW, mean ALCSD, and horizontal cup-to-disc ratio were not associated with axial length or SER ( $P > 0.05$  for all). No optic nerve head or lamina cribrosa parameter showed a significant relationship with intraocular pressure ( $P > 0.05$  for all).

Global and sectoral peripapillary choroidal thicknesses are shown in Table 5-3. One subject was excluded due to poor visibility of the posterior choroid border. The mean global peripapillary choroidal thickness of the study population was  $185.37 \pm 41.48 \mu\text{m}$ . Global peripapillary choroidal thickness was not associated with age ( $P = 0.11$ ), axial length ( $P = 0.53$ ), or SER ( $P = 0.98$ ). Repeated measures ANOVA showed that peripapillary choroidal thickness varied by sector ( $P < 0.001$ ), but not by refractive error group ( $P = 0.09$ ); the inferior choroid was the thinnest and the temporal choroid was the thickest.

**Table 5-2:** Relationships of optic nerve head parameters, including Bruch’s membrane opening (BMO) area, minimum rim width (MRW), anterior lamina cribrosa surface depth (ALCSD), and vertical and horizontal cup-to-disc ratio, with axial length (AL) and spherical equivalent refractive error (SER), for all subjects (n = 52); age-adjusted R<sup>2</sup> and P values are shown for multiple regression analysis

<b>Optic Nerve Head Parameter</b>	<b>Mean ± SD</b>	<b>Relation with AL (R<sup>2</sup>, P value)</b>	<b>Relation with SER (R<sup>2</sup>, P value)</b>
BMO area (mm <sup>2</sup> )	1.89 ± 0.4	R <sup>2</sup> = 0.02, P = 0.1	R <sup>2</sup> = 0.1, P < 0.01*
Mean MRW (µm)	369.4 ± 65.2	R <sup>2</sup> = -0.03, P = 0.7	R <sup>2</sup> = -0.04, P = 0.9
Mean MRW vertical (µm)	412.4 ± 87.4	R <sup>2</sup> = -0.01, β = -15.5, P = 0.3	R <sup>2</sup> = -0.01, β = 7.0, P = 0.4
Mean MRW horizontal (µm)	313.2 ± 59.2	R <sup>2</sup> = -0.04, β = -0.5, P = 0.9	R <sup>2</sup> = -0.04, β = 1.2, P = 0.8
ALCSD (µm)	369.0 ± 85.6	R <sup>2</sup> = -0.03, P = 0.7	R <sup>2</sup> = -0.04, P = 0.8
Vertical C/D	0.4 ± 0.1	R <sup>2</sup> = 0.1, P = 0.04*	R <sup>2</sup> = 0.06, P = 0.05*
Horizontal C/D	0.4 ± 0.1	R <sup>2</sup> = -0.01, P = 0.4	R <sup>2</sup> < 0.01, P = 0.4

\* = significance at P < 0.05

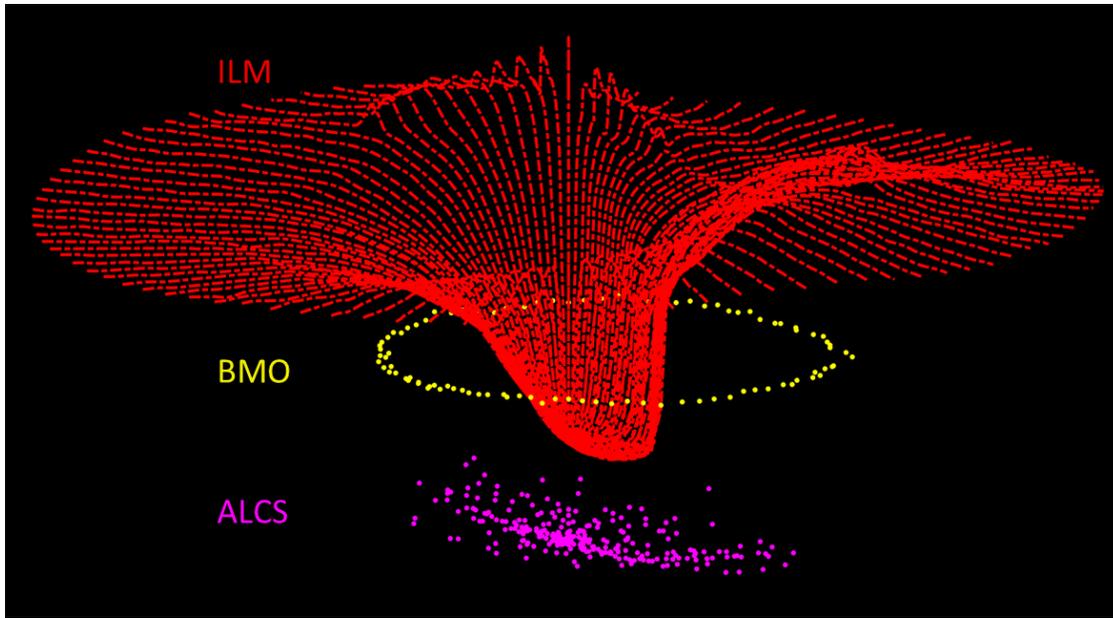


**Figure 5-4:** Representative point cloud for a 12 year old subject

Figure shows the inner limiting membrane (ILM, red), Bruch's membrane opening (BMO, yellow), and anterior lamina cribrosa surface (ALCS, magenta).

**Table 5-3:** Global and sectoral peripapillary choroidal thicknesses for all subjects (n = 51), for non-myopes (n = 28), and for myopes (n = 23); repeated measures ANOVA showed a significant difference by sector ( $P < 0.001$ ) but not by refractive error group ( $P = 0.09$ )

<b>Peripapillary Choroidal Region</b>	<b>All Subjects (n = 51)</b>	<b>Non-Myopes (n = 28)</b>	<b>Myopes (n = 23)</b>
Global	185.4 ± 41.5	177.3 ± 32.3	195.2 ± 49.5
Temporal	205.5 ± 50.5	196.3 ± 41.4	216.7 ± 58.7
Superior	188.8 ± 41.5	179.1 ± 36.3	198.8 ± 46.0
Nasal	179.3 ± 40.8	172.7 ± 29.3	186.8 ± 51.1
Inferior	166.4 ± 42.7	162.7 ± 35.2	173.3 ± 51.5

Global and sectoral peripapillary scaled (i.e. adjusted for lateral magnification) RNFL thicknesses, are shown for non-myopes and myopes in Table 5-4. Three subjects were excluded due to poor image quality. Mean global raw peripapillary RNFL thickness for the study population was  $102.34 \pm 9.08 \mu\text{m}$  (range 81 to 127  $\mu\text{m}$ ). The mean global scaled peripapillary RNFL thickness was  $99.74 \pm 9.44 \mu\text{m}$ . Using multiple regression, age adjusted raw RNFL thickness decreased significantly with increasing axial length ( $R^2 = 0.11$ ,  $\beta = -3.18$ ,  $P < 0.05$ ). However, when RNFL was scaled to account for magnification effects due to axial length and refractive error, the relationship with axial length was no longer present ( $R^2$  adjusted = 0.07,  $\beta = 2.72$ ,  $P = 0.09$ ). Neither raw RNFL nor scaled RNFL were associated with SER when adjusted for age using multiple regression ( $P > 0.05$  for all). Repeated measures ANOVA showed that peripapillary RNFL thickness varied by sector ( $P < 0.001$ ), but not by refractive error group ( $P = 0.57$ ).

**Table 5-4:** Scaled global and sectoral peripapillary RNFL thicknesses for all subjects (n = 49), for non-myopes (n = 29), and for myopes (n = 23); repeated measures ANOVA showed that peripapillary RNFL thickness varied by sector (P < 0.001), but not by refractive error group (P = 0.23).

<b>Peripapillary Retinal Region</b>	<b>All Subjects (n = 49)</b>	<b>Non-Myopes (n = 28)</b>	<b>Myopes (n = 21)</b>
Global	99.7 ± 9.44	103.8 ± 9.2	100.4 ± 8.8
Temporal	68.9 ± 9.9	71.2 ± 9.8	70.4 ± 11.5
Superior temporal	140.1 ± 20.7	148.6 ± 21.0	138.2 ± 23.6
Superior nasal	124.6 ± 41.5	126.7 ± 16.5	116.4 ± 22.5
Nasal	99.2 ± 12.2	71.4 ± 11.5	71.9 ± 12.8
Inferior nasal	120.6 ± 19.4	125.7 ± 21.8	116.4 ± 19.7
Inferior temporal	142.3 ± 20.6	147.9 ± 20.7	146.4 ± 18.2

Optic nerve head parameters were assessed in relation to each other to assess potential interactions. The ALCS was deeper in eyes with a thinner MRW ( $R^2 = 0.41$ ,  $\beta = -0.83$ ,  $P < 0.0001$ ). Mean ALCSD showed no relationship with scaled RNFL thickness ( $R^2 = 0.06$ ,  $\beta = 2.37$ ,  $P = 0.07$ ). BMO area was not associated with global raw RNFL thickness ( $R^2 = 0.001$ ,  $\beta = -0.001$ ,  $P = 0.86$ ), global scaled RNFL thickness ( $R^2 = 0.04$ ,  $\beta = 0.008$ ,  $P = 1.49$ ), vertical cup-to-disc ratio ( $R^2 = 0.01$ ,  $\beta = 0.43$ ,  $P = 0.40$ ), mean MRW ( $R^2 = 0.03$ ,  $\beta = -0.001$ ,  $P = 0.22$ ), or mean ALCSD ( $R^2 = 0.002$ ,  $\beta = -0.0002$ ,  $P = 0.71$ ). Mean MRW and scaled RNFL measures were not associated with each other ( $R^2 = 0.03$ ,  $\beta = 0.02$ ,  $P = 0.23$ ). Raw RNFL and scaled RNFL were also strongly correlated to each other ( $R^2 = 0.65$ ,  $\beta = 0.85$ ,  $P < 0.0001$ ).

#### 5.4.3 Macular Structure

For all subjects, minimum foveal thickness was  $216.90 \pm 13.91 \mu\text{m}$ . The mean total retinal thickness within the central 1 mm centered on the fovea was  $264.22 \pm 21.27 \mu\text{m}$ . Mean global total retinal thickness for the 6 mm annulus centered on the fovea surrounding the central 1 mm and total retinal thickness by quadrant are shown by refractive group in Table 5-5. Multiple regression analysis showed that minimum foveal thickness increased with increasing age ( $R^2 = 0.14$ ,  $\beta = 2.4$ ,  $P < 0.01$ ), but showed no relationship with axial length ( $P = 0.07$ ) or with SER ( $P = 0.46$ ). Total retinal thickness within the central 1 mm diameter was significantly associated with age ( $R^2 = 0.11$ ,  $\beta = 3.16$ ,  $P < 0.05$ ), but not axial length ( $P = 0.12$ ) or SER ( $P = 0.37$ ). Repeated measures ANOVA showed that macular retinal thickness varied by sector ( $P < 0.001$ ), but not by refractive error group ( $P = 0.79$ ).

**Table 5-5:** Total global and sectoral retinal thicknesses ( $\mu\text{m}$ ) in the 6 mm annulus for all subjects ( $n = 52$ ), for non-myopes ( $n = 29$ ), and for myopes ( $n = 23$ ); repeated measures ANOVA showed that macular retinal thickness varied by sector ( $P < 0.001$ ), but not by refractive error group ( $P = 0.79$ )

<b>6 mm Annulus</b>	<b>All Subjects</b>	<b>Non-Myopes</b>	<b>Myopes</b>
<b>Retinal Region</b>	<b>(n = 52)</b>	<b>(n = 29)</b>	<b>(n = 23)</b>
Global	318.1 $\pm$ 13.7	309.2 $\pm$ 15.6	306.8 $\pm$ 12.1
Temporal	308.3 $\pm$ 13.5	308.7 $\pm$ 14.3	308.5 $\pm$ 11.9
Superior	321.9 $\pm$ 13.3	323.3 $\pm$ 14.3	320.9 $\pm$ 11.3
Nasal	328.6 $\pm$ 15.9	330.0 $\pm$ 0.6	327.5 $\pm$ 13.6
Inferior	313.6 $\pm$ 13.7	314.3 $\pm$ 15.4	312.9 $\pm$ 11.2

The mean subfoveal choroidal thickness of the population was  $328.82 \pm 73.97 \mu\text{m}$ , and was not significantly different between non-myopes ( $325.75 \pm 62.45 \mu\text{m}$ ) and myopes ( $332.85 \pm 91.26 \mu\text{m}$ ,  $P = 0.74$ ). Subfoveal choroidal thickness was not associated with age ( $P = 0.31$ ), axial length ( $P = 0.84$ ), or SER ( $P = 0.62$ ). The coefficient of variation for subfoveal choroidal thickness measured by two observers was 5.54% (95% CI 3.24-7.13), and the intraclass correlation coefficient was 0.96 (95% CI 0.91 - 0.98), suggesting excellent agreement of measurements between two observers.

#### 5.3.4 Interocular Symmetry

The biometric and SD-OCT derived measures between the two eyes of 16 randomly selected subjects were assessed for interocular symmetry with coefficient of variation and intraclass correlation coefficient. The measures were highly correlated between the two eyes (CV range 0.88-13.86, ICC range 0.67 - 0.98). Paired t-tests for measures between the two eyes showed no significant difference ( $P > 0.05$  for all).

### 5.5 Discussion

Findings from the current study show that optic disc area, calculated from Bruch's membrane opening, is larger in myopic children, and that vertical cup-to-disc ratio decreases with increasing axial length and myopic refractive error. Additionally, central retinal thickness and minimum foveal thickness increase with age. These findings suggest that the retina and optic nerve head undergo remodeling in school age children during the late stages of emmetropization and during early stages of myopia development.

Optic nerve head structure is known to be altered in myopic adults, which may contribute to the increased risk of glaucoma in myopic individuals.<sup>23, 25, 242</sup> We were interested to understand if myopia-related changes in the optic nerve head are evident in children. In the population of

school age children studied here, anterior lamina cribrosa surface depth was not associated with axial length or refractive error. We found that mean anterior lamina cribrosa surface depth in children was similar to previous reports in adults.<sup>228, 243</sup> Our findings showed that the anterior lamina cribrosa surface was deeper in eyes with a thinner minimum rim width, suggesting that retinal ganglion cell axons are packed more closely along the rim of the optic nerve head in eyes with deeper anterior lamina cribrosa surface.

Optic disc area increased with myopic refractive error, being 0.09 mm<sup>2</sup> larger per diopter. Consistent with other studies, there was no association of optic disc area with age.<sup>244-246</sup> Mean disc area in our study population was  $1.88 \pm 0.37$  mm<sup>2</sup>, similar to previous studies in children (1.68 to 2.30 mm<sup>2</sup>).<sup>245, 247</sup> Although it has been suggested that optic disc size is largely independent of refractive error in the range of -8 D to +4 D,<sup>248</sup> our findings, and those of others,<sup>54, 245, 247</sup> suggest that changes in disc area can be detected across a smaller range of refractive errors. Additionally, the vertical cup-to-disc ratio decreased in eyes with a longer axial length and increased myopic refractive errors. The association of only the vertical cup-to-disc ratio may represent a disproportionate stretching or expansion of the disc relative to the cup margins with increasing axial length and myopic refractive error.

Few studies have evaluated neural rim width in children.<sup>249</sup> The mean minimum rim width found here in children ( $371 \pm 64$  μm) was greater than previous reports in adults (303 to 366 μm).<sup>250, 251</sup> Age-related decreases in minimum rim width have been reported;<sup>246, 250</sup> thus, children might be expected to have a greater minimum rim width than adults. We did not find a relationship between minimum rim width and axial length or refractive error. There was not a significant relationship between minimum rim width and age in our population, likely due to the narrow age range included in this study.

Retinal thickness within the central 1 mm diameter showed a small but significant increase with age for this population, similar to other studies in children.<sup>252-255</sup> Retinal thickness was not associated with axial length or refractive error. Significant associations with age suggest that the organization of the central retina continues to change even after the paracentral retina has reached developmental maturity.<sup>255</sup>

There were no associations between nerve fiber layer thickness and axial length or refractive error. Similar to previous reports, we found that the inferior-temporal peripapillary retinal nerve fiber layer was thickest, followed by the superior-temporal region.<sup>256, 257</sup> Previous studies have reported a negative association between retinal nerve fiber layer thickness and axial length,<sup>258</sup> however, not all studies have corrected for magnification effects inherent with OCT imaging. The thickness of the peripapillary retinal nerve fiber layer decreases with increasing distance from the optic nerve head rim margin.<sup>259</sup> The circular scan used for imaging has a fixed angular size of 12 degrees and assumes an axial length of 24 mm. Therefore, the scan lands closer to the optic nerve head margin in shorter eyes and farther from the margin in longer eyes. This theory is supported in the current study, as the relationship between retinal nerve fiber layer thickness and axial length was lost after scaling retinal images for lateral magnification. These results demonstrate that adjusting for ocular magnification effects is important before interpreting the results of retinal nerve fiber layer thickness relationships with axial length or refractive error. Previous studies in adult human subjects have reported a significant thinning of peripapillary retinal nerve fiber layer with age of approximately 0.3  $\mu\text{m}$  per year.<sup>260</sup> Additionally, studies have reported that age-related thinning of the peripapillary retinal nerve fiber layer varies by sector,<sup>261</sup> suggesting a redistribution of axons with age. However, here in children, we did not observe a relationship between retinal nerve fiber layer thickness with age, either globally or by sector.

Several studies have reported that eyes with longer axial lengths and increasing myopic refractive error have thinner subfoveal choroidal thicknesses.<sup>21,262</sup> Additionally, some studies have reported an increase in choroidal thickness with age,<sup>21</sup> while others reported a decrease.<sup>52, 262</sup> The pattern of choroidal thickness distribution by quadrant around the optic nerve head is also variable in the literature.<sup>232, 233, 263</sup> Here, there were no significant associations between subfoveal or peripapillary choroidal thickness with age, axial length, or refractive error. We found that the inferior peripapillary choroid was the thinnest, while the temporal quadrant was the thickest, followed by the superior and nasal quadrants. We did not observe regional variations in peripapillary choroidal thickness between refractive error groups. Conflicting results between studies may be attributed to choroidal thickness variability, which is known to be influenced by numerous factors, such as time of day<sup>264</sup> and physical activity.<sup>265</sup>

Limitations of the current study include the fact that OCT imaging was not performed at the same time of the day for all subjects, which may have resulted in variation due to diurnal rhythms in choroidal thickness.<sup>266</sup> Additionally, subjects were dilated with tropicamide, an antimuscarinic cycloplegic agent, which may have affected choroidal thickness. However, while recent studies have shown that the antimuscarinic agents atropine and cyclopentolate result in choroidal thickening,<sup>267</sup> tropicamide was reported to have no effect on choroidal thickness.<sup>268</sup> The fact that this study had a small sample size with a limited number of subjects with moderate to high refractive errors may also have contributed to the insignificant relationships found between a majority of the measured parameters, including choroidal thickness with age, axial length, and refraction. Additionally, there was difference in age between the myopes and non-myopes, although age was included as independent variable in multiple regression analysis. Furthermore,

this was a cross-sectional study; a longitudinal study following subjects over time might better elucidate relationships between ocular parameters.

In conclusion, we report normal values for retinal and optic nerve head parameters in non-myopic and myopic school age children, which will be useful when evaluating structural changes in ocular pathology. This study highlights the importance of OCT image scaling to account for the effects of axial length on retinal nerve fiber layer thickness measures in order to accurately assess relationships between parameters, such as with refractive error. Findings provide evidence that ocular structural remodeling occurs in school age children, which may help in understanding the retinal and optic nerve head changes associated with refractive error development and other ocular pathologies.

### **Acknowledgements**

The authors thank the clinical faculty, staff, and students at the University of Houston College of Optometry for help with subject recruitment, and Hope Queener and Nimesh Patel for help with MATLAB programming.

## CHAPTER 6: DISCUSSION

In this chapter, I will summarize the overall results from the experimental studies described in chapters 2, 3, 4, and 5, discuss their implications, and provide thoughts for future studies derived from the current work.

### *6.1 A brief summary of results of the specific study aims*

In chapter 2, retinal function was assessed in normal adult guinea pigs ( $n = 6$ ) using full field flash and pattern ERGs. We demonstrated the presence of a photopic negative response (PhNR) in guinea pigs, and found that the responses were similar in morphology and time course to human PhNR responses. We also demonstrated the presence of pattern ERG responses in guinea pigs, which were again similar in morphology to other mammalian pattern ERG responses. We determined the optimal stimulus size for the P1N2 component of the guinea pig pattern ERG to be 0.05 cycle per degree. The ERG measures, both flash and pattern, showed good repeatability across sessions. We determined the spatial frequency discrimination in guinea pigs with custom optomotor setup, and demonstrated the presence of directional sensitivity in this species, albeit less strong than in rats and mice. We also confirmed the location of visual streak in guinea pigs, using selective marker for retinal ganglion cells, the RBPMS.

In chapter 3, normal retinal, choroidal, and optic nerve head structures were described using *in vivo* imaging technique with OCT imaging in guinea pigs. The thickness values for the guinea pig retina found in this study were comparable to those from other studies, and additional analysis for thickness of different retinal layers and optic nerve head parameters was presented. The *in vivo* measurements from OCT were comparable to those obtained from histological measures in the same eyes.

In chapter 4, we determined the contribution of retinal ganglion cells to the electrophysiological responses from the guinea pig retina and provided a quantification of the structural and functional measures that would occur with major ganglion cell loss in end stage glaucoma in this species. For this purpose, retrograde degeneration of retinal ganglion cells was induced with unilateral optic nerve crush in right eyes. Spatial frequency discrimination was lost in experimental eyes after the crush injury, while having no effect in control eyes. The PhNR was found to be the earliest affected measure of ERG following the crush, suggesting the contribution of retinal ganglion cells to this component of ERG in guinea pigs. We also found significant reduction in the first oscillatory potential (OP1) in the experimental eyes compared to contralateral control eyes, while OP2 and OP3 were unaffected. Other components of flash ERG, as well as all waves of pattern ERG, were relatively unaffected. Structural measures with OCT showed approximately 38% thinning of the circumpapillary RNFL thickness in experimental eyes within 4 weeks following the crush, with no effect on the contralateral control eyes. Approximately 78% of the retinal ganglion cells were lost within 4 weeks following the nerve crush in the experimental eyes, when compared to control eyes, and the reduction in following weeks was not significant from that in 4 weeks.

Chapter 5 aimed to assess retinal, choroidal, and optic nerve head parameters in school age children as a function of age, axial length, and refraction, and to compare these parameters among non-myopic and myopic children. Significant thinning of retinal nerve fiber layer with increasing axial length was observed; however, this relationship was lost following correction of the RNFL thickness for magnification effects, thus illustrating the importance of applying magnification adjustments before deriving conclusions about relationships with axial length or refraction. Myopic children were found to have larger optic nerve head area and diameter than non-myopic

children. Central retinal thickness and minimum foveal thickness increased with age in both groups.

## ***6.2 Visual function in guinea pigs***

One of the main purposes of this dissertation was to further explore visual function in guinea pigs using electrophysiological and behavioral methods, and to assess their relationship with retinal ganglion cell integrity. We wanted to know whether guinea pig retinal ganglion cell function could be described with electrophysiology, as demonstrated in other species, such as mice, rats, non-human primates, and humans. The presence of the PhNR and pattern ERG waveforms, including the N1, P1, and N2 components, were demonstrated in chapter 2. These waveforms had similar morphology to those from other mammalian retina.

With the work presented in chapter 4, we confirmed that the PhNR depends on the functional integrity of retinal ganglion cells for about half of its maximum amplitude, while pattern ERG waves seemed to be independent of ganglion cell function. Figure 4-5 A shows approximately 40% reduction of the PhNR amplitude from baseline to 2 weeks following optic nerve crush, which reached a maximum reduction of approximately 50% in 4 weeks. However, still a significant amount of PhNR amplitude remained despite loss of around 80% of the retinal ganglion cell population at 12 weeks following the crush, suggesting that PhNR receives input from other retinal neurons besides the ganglion cells. Contributions of other retinal cells, such as amacrine and glial cells, to the PhNR have been suggested in non-human primates.<sup>69</sup> Similarly, even after 15 weeks of optic nerve transection, a significant amount of PhNR persisted in rats,<sup>72</sup> further suggesting the likelihood of other retinal neurons contributing to the PhNR. Further experiments with pharmacology, blocking the activity of specific pathways and neurons in the retina, are necessary to determine other generators of the PhNR in guinea pigs. With the work from chapter

4, it was also found that the pattern ERG in guinea pigs does not largely depend on the functional integrity of retinal ganglion cells (figure 4-6 A, B; table 4-4). This independence of pattern ERG responses from retinal ganglion cells integrity was surprising, as pattern ERG in mammalian retina has been shown to depend on the functional integrity of retinal ganglion cells.<sup>74, 101, 124, 269</sup> Pattern ERG has been shown to remain unaffected following optic nerve transection in chicks and pigeons,<sup>104, 106</sup> although they are not mammalian species. It is likely that pattern ERG in guinea pigs reflects the functional integrity of other retinal neurons in addition to retinal ganglion cells. For example, in human subjects, the pattern ERG was reduced, but not completely eliminated, even after 30 months following surgical resection of the optic nerve,<sup>270</sup> suggesting that retinal neurons other than retinal ganglion cells might be contributing to human pattern ERG responses. Like the PhNR, further studies with pharmacology are needed to better understand the retinal source of origin of the pattern ERG in guinea pigs.

An additional aim of the work presented in chapter 2 was to confirm the location of visual streak in the guinea pig retina. Previous studies showed conflicting results on the location of visual streak in guinea pig retina; while Choudhury, et al. suggested that visual streak in the guinea pig retina was located inferiorly below the optic nerve head,<sup>112</sup> Do-Nascimento, et al. reported that it was in the superior retina above the optic nerve head.<sup>111</sup> Both of these studies used a non-specific marker for retinal ganglion cells, and relied on morphometric measures for quantification of cells. This limitation was addressed as a part of the work in chapter 2 by using selective marker for retinal ganglion cells, retinal binding protein with multiple splicing (RBPMS),<sup>125</sup> and the location of visual streak was confirmed to be in the superior retina in guinea pigs, 1-2 mm above the optic nerve head.

### ***6.3 Retinal structural change with optic nerve crush in guinea pigs***

Guinea pig normal retinal and optic nerve head structure was described using non-invasive *in vivo* imaging using optical coherence tomography in chapter 3. We found a mean retinal thickness of 152  $\mu\text{m}$  for the guinea pig retina, which is comparable to the retinal thickness of 142  $\mu\text{m}$  at a distance of 3 mm from the optic nerve head from a previous study.<sup>158</sup> The *in vivo* measurements found here were comparable to histological measurements obtained at similar locations in the retina in the same eyes (figure 3-8, table 3-5). Using a similar OCT imaging technique, the retina is reported to be much thicker in mice (approximately 215  $\mu\text{m}$ )<sup>271</sup> and rats (approximately 242  $\mu\text{m}$ ).<sup>157</sup> However, the guinea pig retina is avascular, except for the vascular tuft at the optic nerve head, and it has been suggested that avascular retinas are generally much thinner compared to vascular retinas.<sup>178</sup>

We found a progressive reduction in RNFL thickness starting at 4 weeks following optic nerve crush. This reduction was approximately 35% compared to baseline thickness. Significant reduction of the retinal ganglion cell nerve fiber layer of approximately 54% was reported within a week following optic nerve crush in mice<sup>63</sup>, and a reduction in RNFL thickness of 54% at 2 weeks following the crush was reported in rats.<sup>214</sup> Difference in species and retinal vascularity could be a factor for different rates of reduction of RNFL thickness following the optic nerve crush. Additional reduction of RNFL thickness in subsequent time points of 6, 8, 10, and 12 weeks was observed in this study, with a maximum of 65% reduction from baseline at 12 weeks following the crush. These results indicate that progressive thinning of RNFL in guinea pigs can be monitored with *in vivo* imaging using OCT.

#### ***6.4 Retinal and optic nerve head structure with age, axial length and refraction in school age children***

In addition to the guinea pig studies, we also aimed at to evaluate retinal and optic nerve head structure in school age children in relation to age, axial length and refraction, using similar imaging analysis techniques developed in chapter 3. This work is presented in chapter 5. With this work, we investigated whether these structures changed with age, axial length, or refraction in these young subjects and if there were differences in these structures among non-myopic and myopic children. Earlier studies in children suggested a thinning of retinal nerve fiber layer with increasing axial length, and the relation was described to disappear after magnification effects were corrected.<sup>236</sup> Similarly, in chapter 5, we reported a thinning of RNFL thickness with increasing axial length, and the relation disappeared once magnification effects were corrected. This result is not surprising, as the thickness of peripapillary retinal nerve fiber layer decreases with increasing distance from the optic nerve head rim margin,<sup>259</sup> and the circular scan used for peripapillary retinal nerve fiber layer thickness measurement having a fixed angular size of 12 degrees lands closer to the optic nerve head rim margin in shorter eyes and farther from the rim margin in longer eyes, thus resulting in thicker measurements in shorter eyes, such as in hyperopes, and thinner measurements in longer eyes, such as in myopes. Accordingly, such associations of retinal nerve fiber layer thickness with axial length and refraction disappeared with correction for magnification effects in this study. These findings highlight the importance of correcting for magnification effects before drawing conclusions on the relation of RNFL thickness with axial length.

Optic disc size, represented by the Bruch's membrane opening diameter and area, was found to be significantly larger in myopic children compared to non-myopic children. Optic nerve head diameter also increased with significantly with increasing axial length and myopic refraction.

The most likely mechanism for these observations is stretching of the posterior pole with increasing axial length, which would stretch the scleral tissue around the optic nerve head, thus increasing the optic nerve head size. Optic disc size has been found to be associated with refraction, with smaller size in hyperopes and larger size in myopes.<sup>54, 247</sup> Magnification effects can influence the measurements, however, our measurements and those from the previous studies were corrected for lateral magnification. Although Jonas, et al. suggested that optic disc size can be largely independent of refractive error in the range of -8 D to +4 D,<sup>248</sup> the measurements were based on optic disc photographs and not on estimation of disc size from Bruch's membrane opening calculations. The results from our study, and the aforementioned studies, suggest that small but significant associations between optic disc size and axial length and refraction can be detected from OCT based magnification corrected measurements.

The associations between peripapillary choroid and axial length or refractive error are not clear in the literature. Some studies have suggested thinner subfoveal choroid with increasing axial length and myopic refractive error.<sup>21, 262</sup> Interestingly, we did not find an association of choroidal thickness, either subfoveal or peripapillary, with age, axial length, or refractive error. Although subfoveal choroidal thickness was measured manually in this study, the measurements were in good agreement between two observers masked to the refractive status of the subjects. Several studies have suggested no association of peripapillary choroidal thickness with axial length or refractive error, although sectoral differences between non-myopic and myopic children for peripapillary choroid have been suggested.<sup>232, 233</sup> However, it is important to note that since peripapillary choroidal thickness varies with increasing distance from the optic nerve head margin,<sup>232</sup> the measurements must be obtained at same distance from the optic nerve head margin to confirm whether or not a relationship between peripapillary choroidal thickness and axial length

and refractive error exists. Our measurements of peripapillary choroidal thickness were obtained within an annulus of 1.7 mm from the optic nerve head margin in all subjects, thus standardizing the measurement distance across all subjects. However, our choroidal measurements have some limitations. We did not acquire images for all our subjects at the same time of the day, as most of them were recruited from the clinic and their appointment schedule and examination duration at the clinic were variable. As literature suggests, there is significant diurnal variation in choroidal thickness, which may have influenced our measurements.<sup>266</sup> There is also evidence that antimuscarinic agents, such as cyclopentolate and atropine, can affect choroidal thickness,<sup>267</sup> although another study suggested no effect of tropicamide, an antimuscarinic agent, on the choroidal thickness measurements.<sup>268</sup> It is unclear whether the dilating agent may have affected choroidal thickness in the current study.

#### ***6.4 Future directions***

In this section, I propose additional future studies that will complement the work that I have described in my dissertation.

1. The contribution of retinal ganglion cells to the flash and pattern ERG was investigated, showing that the PhNR significantly reduced following optic nerve crush, while the pattern ERG remained largely unchanged. We also showed that retinal thinning following retinal ganglion cell degeneration can be assessed longitudinally with OCT imaging in guinea pigs. Future studies using other methods of retinal ganglion cell dysfunction would provide further insight into guinea pig retinal function. For example, an elevated intraocular pressure (IOP) model in guinea pigs could be used to study structural and functional changes as a model of human glaucoma. Microbead injection and laser trabeculoplasty techniques to raise IOP in guinea pigs were carried out as part of this dissertation; however, the treatments were not

successful. Other techniques, such as episcleral vein cauterization or steroid injections, may be more successful to elevate the IOP in guinea pigs.

2. The retinal thinning following optic nerve crush was assessed with circumpapillary circular scan centered on the optic nerve head. Future studies evaluating the thickness profile of nerve fiber layer around the optic nerve with volumetric scans would be useful to assess the presence of localized patterns of retinal nerve fiber layer thinning. Our results for retinal NFL thicknesses following optic nerve crush show greatest reduction in the inferior sectors (figure 4-3, C and D).
3. The loss of retinal ganglion cells was shown with a selective marker for retinal ganglion cells in guinea pigs. This effect with optic nerve crush was assessed for different end points in the study period, from 4 to 12 weeks. The guinea pig retina possesses different subtypes of retinal ganglion cells with different sizes.<sup>125</sup> By including more animals per end point in the study, a pattern of specific subtypes of retinal ganglion cell degeneration following optic nerve crush may be evident. Different subtypes and sizes of retinal ganglion cells might show different kind of response with the retrograde degeneration. Towards the end of the study period, at 12 weeks following the optic nerve crush, there were still approximately 15% of the retinal ganglion cells that survived, compared to approximately 22% survival at 4 weeks following the crush. It appeared from the pictures that cells had shrunk in size, although it was not quantified. It would be interesting to study the types of retinal ganglion cells that survived until the end of 12 weeks with the injury; whether they were small cells that were immune to the injury from the beginning or they were large retinal ganglion cells that had shrunken in size progressively. It is also possible that different retinal eccentricities show different rate of

degeneration, which could be better assessed by having more animals per end point in the study period.

4. The results from chapter 3 demonstrated significant changes in PhNR amplitude within 2 weeks following optic nerve crush, with approximately 40% reduction from baseline. This reduction increased further to approximately 50% at 4 weeks and remained relatively constant for the rest of the study period, suggesting that the PhNR receives significant contribution from other retinal neurons. OP1 was also significantly reduced in the experimental eyes compared to control eyes following the crush, while OP2 and OP3 were relatively unaffected. Furthermore, there was no significant change in the pattern ERG responses following the crush injury. Future studies to assess what other retinal neurons might be contributing to these components of the ERGs in guinea pigs would be valuable, potentially through pharmacological studies with blocking of specific ON and OFF pathways of the retina. For example, intravitreal injection of L-AP4/APB (2-amino-4-phosphonobutyric acid) blocks ON bipolar cells light responses and thus the activity in the ON pathway,<sup>272</sup> and PDA (cis-2,3-piperidine dicarboxylic acid) blocks the activity in the hyperpolarizing second-order and all third order neurons.<sup>75, 273</sup> Similarly, TTX, which has been shown to block Na<sup>+</sup> dependent spiking activity in the retinal ganglion cells and amacrine cells,<sup>274</sup> and also in cone bipolar cells,<sup>275</sup> could be used to further study the retinal source of origin of the ERG components in guinea pigs.
5. The ultimate aim of this project is to evaluate susceptibility to glaucoma in myopic eyes. Future studies aimed at monitoring retinal structure and function in guinea pigs with both elevated IOP and myopia would provide insight into potential mechanisms that increase the risk of glaucoma in myopic individuals. The higher prevalence of glaucoma in myopic eyes might

reflect changes in retinal structure and function secondary to myopic eye growth, which can be assessed in guinea pigs using the imaging and electrophysiological methods developed in this dissertation. It has been demonstrated in guinea pigs that reduction of intraocular pressure slows myopia progression.<sup>276</sup> It would be really interesting to further evaluate retinal structure and function in this model with elevation of IOP to test the hypothesis that elevation of IOP increases myopia progression.

7. In children, relationships were observed with age, axial length, and refraction for some retinal and optic nerve head parameters. As age was related to axial length and refraction, future longitudinal studies would be valuable to better elucidate the retinal and optic nerve head structural changes as school age children grow older. Such longitudinal study will be able to show better the pattern of refractive changes with age in school age children along with structural changes, if any. Additionally, it would be interesting to assess the peripapillary choroidal thickness in more controlled conditions, such as obtaining OCT images prior to using dilating agents and accounting for diurnal variations, as choroidal thickness has been found to have significant diurnal variation and may be affected by the use of topically instilled dilating agents.<sup>266, 267</sup>

## REFERENCES:

1. Bourne RR, Stevens GA, White RA, et al. Causes of vision loss worldwide, 1990-2010: a systematic analysis. *Lancet Glob Health* 2014;1:e339-349.
2. Holden BA, Fricke TR, Wilson DA, et al. Global prevalence of myopia and high myopia and temporal trends from 2000 through 2050. *Ophthalmology* 2016;123:1036-1042.
3. Lin LL, Shih YF, Hsiao CK, Chen CJ. Prevalence of myopia in Taiwanese schoolchildren: 1983 to 2000. *Ann Acad Med Singapore* 2004;33:27-33.
4. Pan CW, Ramamurthy D, Saw SM. Worldwide prevalence and risk factors for myopia. *Ophthalmic Physiol Opt* 2011;32:3-16.
5. Vitale S, Sperduto RD, Ferris FL, 3rd. Increased prevalence of myopia in the United States between 1971-1972 and 1999-2004. *Arch Ophthalmol* 2009;127:1632-1639.
6. Williams KM, Bertelsen G, Cumberland P, et al. Increasing prevalence of myopia in Europe and the impact of education. *Ophthalmology* 2015;122:1489-1497.
7. Smith TS, Frick KD, Holden BA, Fricke TR, Naidoo KS. Potential lost productivity resulting from the global burden of uncorrected refractive error. *Bull World Health Organ* 2009;87:431-437.
8. Fricke TR, Holden BA, Wilson DA, et al. Global cost of correcting vision impairment from uncorrected refractive error. *Bull World Health Organ* 2012;90:728-738.
9. Ikuno Y. Overview of the complications of high myopia. *Retina* 2017;37:2347-2351.
10. Qiu M, Wang SY, Singh K, Lin SC. Association between myopia and glaucoma in the United States population. *Invest Ophthalmol Vis Sci* 2013;54:830-835.
11. Saw SM, Gazzard G, Shih-Yen EC, Chua WH. Myopia and associated pathological complications. *Ophthalmic Physiol Opt* 2005;25:381-391.
12. Xu L, Wang Y, Wang S, Jonas JB. High myopia and glaucoma susceptibility the Beijing Eye Study. *Ophthalmology* 2007;114:216-220.
13. Mitchell P, Hourihan F, Sandbach J, Wang JJ. The relationship between glaucoma and myopia: the Blue Mountains Eye Study. *Ophthalmology* 1999;106:2010-2015.
14. Marcus MW, de Vries MM, Junoy Montolio FG, Jansonius NM. Myopia as a risk factor for open-angle glaucoma: a systematic review and meta-analysis. *Ophthalmology* 2011;118:1989-1994.e1982.

15. Suzuki Y, Iwase A, Araie M, et al. Risk factors for open-angle glaucoma in a Japanese population: the Tajimi Study. *Ophthalmology* 2006;113:1613-1617.
16. Grodum K, Heijl A, Bengtsson B. Refractive error and glaucoma. *Acta Ophthalmol Scand* 2001;79:560-566.
17. Chen SJ, Lu P, Zhang WF, Lu JH. High myopia as a risk factor in primary open angle glaucoma. *Int J Ophthalmol* 2013;5:750-753.
18. Kuzin AA, Varma R, Reddy HS, Torres M, Azen SP. Ocular biometry and open-angle glaucoma: the Los Angeles Latino Eye Study. *Ophthalmology* 2010;117:1713-1719.
19. Shim SH, Sung KR, Kim JM, et al. The Prevalence of open-angle glaucoma by age in myopia: the Korea national health and nutrition examination survey. *Curr Eye Res* 2016;42:65-71.
20. Nagaoka N, Jonas JB, Morohoshi K, et al. Glaucomatous-type optic discs in high myopia. *PLoS One* 2015;10:e0138825.
21. Read SA, Collins MJ, Vincent SJ, Alonso-Caneiro D. Choroidal thickness in myopic and nonmyopic children assessed with enhanced depth imaging optical coherence tomography. *Invest Ophthalmol Vis Sci* 2013;54:7578-7586.
22. Wei WB, Xu L, Jonas JB, et al. Subfoveal choroidal thickness: the Beijing Eye Study. *Ophthalmology* 2012;120:175-180.
23. AttaAllah HR, Omar IAN, Abdelhalim AS. Evaluation of optic nerve head parameters and retinal nerve fiber layer thickness in axial myopia using SD OCT. *Ophthalmol Ther* 2017;6:335-341.
24. Jonas JB, Berenshtein E, Holbach L. Lamina cribrosa thickness and spatial relationships between intraocular space and cerebrospinal fluid space in highly myopic eyes. *Invest Ophthalmol Vis Sci* 2004;45:2660-2665.
25. Jonas JB, Ohno-Matsui K, Panda-Jonas S. Optic nerve head histopathology in high axial myopia. *J Glaucoma* 2017;26:187-193.
26. Howlett MH, McFadden SA. Form-deprivation myopia in the guinea pig (*Cavia porcellus*). *Vision Res* 2006;46:267-283.
27. Garcia MB, Jha AK, Healy KE, Wildsoet CF. A bioengineering approach to myopia control tested in a guinea pig model. *Invest Ophthalmol Vis Sci* 2017;58:1875-1886.
28. Howlett MH, McFadden SA. Spectacle lens compensation in the pigmented guinea pig. *Vision Res* 2009;49:219-227.
29. Li WH, Hide WA, Zharkikh A, Ma DP, Graur D. The molecular taxonomy and evolution of the guinea pig. *J Hered* 1992;83:174-181.

30. Loeliger M, Rees S. Immunocytochemical development of the guinea pig retina. *Exp Eye Res* 2005;80:9-21.
31. Spira AW. In utero development and maturation of the retina of a non-primate mammal: a light and electron microscopic study of the guinea pig. *Anat Embryol (Berl)* 1975;146:279-300.
32. Huang J, Wyse JP, Spira AW. Ontogenesis of the electroretinogram in a precocial mammal, the guinea pig (*Cavia porcellus*). *Comp Biochem Physiol A Comp Physiol* 1990;95:149-155.
33. Jacobs GH, Deegan JF, 2nd. Spectral sensitivity, photopigments, and color vision in the guinea pig (*Cavia porcellus*). *Behav Neurosci* 1994;108:993-1004.
34. Zhou X, Qu J, Xie R, et al. Normal development of refractive state and ocular dimensions in guinea pigs. *Vision research* 2006;46:2815-2823.
35. Racine J, Joly S, Lachapelle P. Longitudinal assessment of retinal structure and function reveals a rod-cone degeneration in a guinea pig model initially presented as night blind. *Doc Ophthalmol* 2011;123:1-19.
36. Lei B. The ERG of guinea pig (*Cavia porcellus*): comparison with I-type monkey and E-type rat. *Doc Ophthalmol* 2003;106:243-249.
37. Racine J, Joly S, Rufiange M, Rosolen S, Casanova C, Lachapelle P. The photopic ERG of the albino guinea pig (*Cavia porcellus*): a model of the human photopic ERG. *Doc Ophthalmol* 2005;110:67-77.
38. Ostrin LA. Optic nerve head and intraocular pressure in the guinea pig eye. *Exp Eye Res* 2016;7-16.
39. Morrison J, Farrell S, Johnson E, Deppmeier L, Moore CG, Grossmann E. Structure and composition of the rodent lamina cribrosa. *Exp Eye Res* 1995;60:127-135.
40. Jonas JB, Mardin CY, Schlotzer-Schrehardt U, Naumann GO. Morphometry of the human lamina cribrosa surface. *Invest Ophthalmol Vis Sci* 1991;32:401-405.
41. Minckler DS. Histology of optic nerve damage in ocular hypertension and early glaucoma. *Surv Ophthalmol* 1989;33 Suppl:401-402; discussion 409-411.
42. Quigley H, Anderson DR. The dynamics and location of axonal transport blockade by acute intraocular pressure elevation in primate optic nerve. *Invest Ophthalmol* 1976;15:606-616.
43. Quigley HA, Addicks EM, Green WR, Maumenee AE. Optic nerve damage in human glaucoma. II. The site of injury and susceptibility to damage. *Arch Ophthalmol* 1981;99:635-649.
44. Fujita Y, Imagawa T, Uehara M. Comparative study of the lamina cribrosa and the pial septa in the vertebrate optic nerve and their relationship to the myelinated axons. *Tissue & cell* 2000;32:293-301.

45. Dai C, Khaw PT, Yin ZQ, Li D, Raisman G, Li Y. Structural basis of glaucoma: the fortified astrocytes of the optic nerve head are the target of raised intraocular pressure. *Glia* 2012;60:13-28.
46. Albrecht May C. Comparative anatomy of the optic nerve head and inner retina in non-primate animal models used for glaucoma research. *Open Ophthalmol J* 2008;2:94-101.
47. Huang D, Swanson EA, Lin CP, et al. Optical coherence tomography. *Science* 1991;254:1178-1181.
48. Kang SH, Hong SW, Im SK, Lee SH, Ahn MD. Effect of myopia on the thickness of the retinal nerve fiber layer measured by Cirrus HD optical coherence tomography. *Invest Ophthalmol Vis Sci* 2010;51:4075-4083.
49. Kim MJ, Lee EJ, Kim TW. Peripapillary retinal nerve fibre layer thickness profile in subjects with myopia measured using the Stratus optical coherence tomography. *Br J Ophthalmol* 2009;94:115-120.
50. Yun SC, Hahn IK, Sung KR, Yoon JY, Jeong D, Chung HS. Lamina cribrosa depth according to the level of axial length in normal and glaucomatous eyes. *Graefes Arch Clin Exp Ophthalmol* 2015;253:2247-2253.
51. Shoji T. Correlation between lamina cribrosa tilt, myopia and glaucoma using optical coherence tomography with a wide band femtosecond mode-locked laser. *Nippon Ganka Gakkai Zasshi* 2016;120:764-771.
52. Fontaine M, Gaucher D, Sauer A, Speeg-Schatz C. Choroidal thickness and ametropia in children: a longitudinal study. *Eur J Ophthalmol* 2017;27:730-734.
53. Bae SH, Kang SH, Feng CS, Park J, Jeong JH, Yi K. Influence of myopia on size of optic nerve head and retinal nerve fiber layer thickness measured by spectral domain optical coherence tomography. *Korean J Ophthalmol* 2016;30:335-343.
54. Leung CK, Cheng AC, Chong KK, et al. Optic disc measurements in myopia with optical coherence tomography and confocal scanning laser ophthalmoscopy. *Invest Ophthalmol Vis Sci* 2007;48:3178-3183.
55. Kotowski J, Wollstein G, Folio LS, Ishikawa H, Schuman JS. Clinical use of OCT in assessing glaucoma progression. *Ophthalmic Surg Lasers Imaging* 2011;42 Suppl:S6-s14.
56. Schuman JS, Pedut-Kloizman T, Pakter H, et al. Optical coherence tomography and histologic measurements of nerve fiber layer thickness in normal and glaucomatous monkey eyes. *Invest Ophthalmol Vis Sci* 2007;48:3645-3654.
57. Leung CK, Lam S, Weinreb RN, et al. Retinal nerve fiber layer imaging with spectral-domain optical coherence tomography: analysis of the retinal nerve fiber layer map for glaucoma detection. *Ophthalmology* 2010;117:1684-1691.

58. Reznicek L, Burzer S, Laubichler A, et al. Structure-function relationship comparison between retinal nerve fibre layer and Bruch's membrane opening-minimum rim width in glaucoma. *Int J Ophthalmol* 2017;10:1534-1538.
59. Patel NB, Sullivan-Mee M, Harwerth RS. The relationship between retinal nerve fiber layer thickness and optic nerve head neuroretinal rim tissue in glaucoma. *Invest Ophthalmol Vis Sci* 2014;55:6802-6816.
60. Bellezza AJ, Rintalan CJ, Thompson HW, Downs JC, Hart RT, Burgoyne CF. Deformation of the lamina cribrosa and anterior scleral canal wall in early experimental glaucoma. *Invest Ophthalmol Vis Sci* 2003;44:623-637.
61. Liu Y, McDowell CM, Zhang Z, Tebow HE, Wordinger RJ, Clark AF. Monitoring retinal morphologic and functional changes in mice following optic nerve crush. *Invest Ophthalmol Vis Sci* 2014;55:3766-3774.
62. Gabriele ML, et al. Optic nerve crush mice followed longitudinally with spectral domain optical coherence tomography. - PubMed - NCBI. 2017.
63. Munguba GC, et al. Nerve fiber layer thinning lags retinal ganglion cell density following crush axonopathy. - PubMed - NCBI. 2017.
64. Bush RA, Sieving PA. A proximal retinal component in the primate photopic ERG a-wave. *Invest Ophthalmol Vis Sci* 1994;35:635-645.
65. Sieving PA, Murayama K, Naarendorp F. Push-pull model of the primate photopic electroretinogram: a role for hyperpolarizing neurons in shaping the b-wave. *Vis Neurosci* 1994;11:519-532.
66. Knapp AG, Schiller PH. The contribution of on-bipolar cells to the electroretinogram of rabbits and monkeys. A study using 2-amino-4-phosphonobutyrate (APB). *Vision Res* 1984;24:1841-1846.
67. Gur M, Zeevi YY, Bielik M, Neumann E. Changes in the oscillatory potentials of the electroretinogram in glaucoma. *Curr Eye Res* 1987;6:457-466.
68. Lan Y, Jian G, Liu Y. [The evaluation of oscillatory potentials of the electroretinogram in the early diagnosis of the patients with primary open angle glaucoma]. *Yan Ke Xue Bao* 1996;12:88-92.
69. Viswanathan S, Frishman LJ, Robson JG, Harwerth RS, Smith EL, 3rd. The photopic negative response of the macaque electroretinogram: reduction by experimental glaucoma. *Invest Ophthalmol Vis Sci* 1999;40:1124-1136.
70. Viswanathan S, Frishman LJ, Robson JG, Walters JW. The photopic negative response of the flash electroretinogram in primary open angle glaucoma. *Invest Ophthalmol Vis Sci* 2001;42:514-522.

71. Chrysostomou V, Crowston JG. The photopic negative response of the mouse electroretinogram: reduction by acute elevation of intraocular pressure. *Invest Ophthalmol Vis Sci* 2013;54:4691-4697.
72. Li B, Barnes GE, Holt WF. The decline of the photopic negative response (PhNR) in the rat after optic nerve transection. *Doc Ophthalmol* 2006;111:23-31.
73. Riggs LA, Johnson EP, Schick AM. Electrical responses of the human eye to moving stimulus patterns. *Science* 1964;144:567.
74. Miura G, Wang MH, Ivers KM, Frishman LJ. Retinal pathway origins of the pattern ERG of the mouse. *Exp Eye Res* 2009;89:49-62.
75. Luo X, Frishman LJ. Retinal pathway origins of the pattern electroretinogram (PERG). *Invest Ophthalmol Vis Sci* 2011;8571-8584.
76. Grillo SL, Koulen P. Psychophysical testing in rodent models of glaucomatous optic neuropathy. *Exp Eye Res* 2015;141:154-163.
77. Tauber ES, Atkin A. Optomotor responses to monocular stimulation: relation to visual system organization. *Science* 1968;160:1365-1367.
78. Thaug C, Arnold K, Jackson IJ, Coffey PJ. Presence of visual head tracking differentiates normal sighted from retinal degenerate mice. *Neurosci Lett* 2002;325:21-24.
79. Cowey A, Franzini C. The retinal origin of uncrossed optic nerve fibres in rats and their role in visual discrimination. *Exp Brain Res* 1979;35:443-455.
80. Frishman L, Sustar M, Kremers J, et al. ISCEV extended protocol for the photopic negative response (PhNR) of the full-field electroretinogram. *Doc Ophthalmol* 2018;136:207-211.
81. Bach M, Brigell MG, Hawlina M, et al. ISCEV standard for clinical pattern electroretinography (PERG): 2012 update. *Doc Ophthalmol* 2012;126:1-7.
82. Mutti DO, Mitchell GL, Jones LA, et al. Axial growth and changes in lenticular and corneal power during emmetropization in infants. *Invest Ophthalmol Vis Sci* 2005;46:3074-3080.
83. Ehrlich DL, Braddick OJ, Atkinson J, et al. Infant emmetropization: longitudinal changes in refraction components from nine to twenty months of age. *Optom Vis Sci* 1997;74:822-843.
84. Goss DA, Winkler RL. Progression of myopia in youth: age of cessation. *Am J Optom Physiol Opt* 1983;60:651-658.
85. Hopf S, Pfeiffer N. [Epidemiology of myopia]. *Ophthalmologe* 2017;114:20-23.
86. Jonas JB, Weber P, Nagaoka N, Ohno-Matsui K. Glaucoma in high myopia and parapapillary delta zone. *PLoS One* 2017;12:e0175120.

87. Jiang L, Long K, Schaeffel F, et al. Disruption of emmetropization and high susceptibility to deprivation myopia in albino guinea pigs. *Invest Ophthalmol Vis Sci* 2011;52:6124-6132.
88. McFadden SA, Howlett MH, Mertz JR. Retinoic acid signals the direction of ocular elongation in the guinea pig eye. *Vision Res* 2004;44:643-653.
89. Dong L, Shi XH, Kang YK, Wei WB, Wang YX, Jonas JB. Ocular size and shape in lens-induced Myopization in young Guinea pigs. *BMC Ophthalmol* 2019;19:102.
90. Lu F, Zhou X, Jiang L, et al. Axial myopia induced by hyperopic defocus in guinea pigs: A detailed assessment on susceptibility and recovery. *Exp Eye Res* 2009;89:101-108.
91. Lu F, Zhou X, Zhao H, et al. Axial myopia induced by a monocularly-deprived facemask in guinea pigs: A non-invasive and effective model. *Exp Eye Res* 2005;82:628-636.
92. Abdeljalil J, Hamid M, Abdel-Mouttalib O, et al. The optomotor response: a robust first-line visual screening method for mice. *Vision Res* 2005;45:1439-1446.
93. Kretschmer F, Kretschmer V, Kunze VP, Kretzberg J. OMR-arena: automated measurement and stimulation system to determine mouse visual thresholds based on optomotor responses. *PLoS One* 2013;8:e78058.
94. Prusky GT, Alam NM, Beekman S, Douglas RM. Rapid quantification of adult and developing mouse spatial vision using a virtual optomotor system. *Invest Ophthalmol Vis Sci* 2004;45:4611-4616.
95. Douglas RM, Alam NM, Silver BD, McGill TJ, Tschetter WW, Prusky GT. Independent visual threshold measurements in the two eyes of freely moving rats and mice using a virtual-reality optokinetic system. *Vis Neurosci* 2005;22:677-684.
96. Thomas BB, Seiler MJ, Satta SR, Coffey PJ, Aramant RB. Optokinetic test to evaluate visual acuity of each eye independently. *J Neurosci Methods* 2004;138:7-13.
97. Tusa RJ, Demer JL, Herdman SJ. Cortical areas involved in OKN and VOR in cats: cortical lesions. *J Neurosci* 1989;9:1163-1178.
98. Zee DS, Tusa RJ, Herdman SJ, Butler PH, Gucer G. Effects of occipital lobectomy upon eye movements in primate. *J Neurophysiol* 1987;58:883-907.
99. Jiang LQ, Zhang S, Mo DP, Ye LY, Qu J, Zhou XT. [Measurement of grating acuity in guinea pigs by a customized automated optomotor device]. *Zhonghua Yan Ke Za Zhi* 2010;46:725-730.
100. Mafei L, Fiorentini A. Electroretinographic responses to alternating gratings before and after section of the optic nerve. *Science* 1981;211:953-955.

101. Berardi N, Domenici L, Gravina A, Maffei L. Pattern ERG in rats following section of the optic nerve. *Exp Brain Res* 1990;79:539-546.
102. Viswanathan S, Frishman LJ, Robson JG. The uniform field and pattern ERG in macaques with experimental glaucoma: removal of spiking activity. *Invest Ophthalmol Vis Sci* 2000;41:2797-2810.
103. Dawson WW, Maida TM, Rubin ML. Human pattern-evoked retinal responses are altered by optic atrophy. *Invest Ophthalmol Vis Sci* 1982;22:796-803.
104. Porciatti V, Francesconi W, Bagnoli P. The pigeon pattern electroretinogram is not affected by massive loss of cell bodies in the ganglion layer induced by chronic section of the optic nerve. *Doc Ophthalmol* 1985;61:41-47.
105. Blondeau P, Lamarche J, Lafond G, Brunette JR. Pattern electroretinogram and optic nerve section in pigeons. *Curr Eye Res* 1987;6:747-756.
106. Ostrin LA, Choh V, Wildsoet CF. The pattern ERG in chicks - Stimulus dependence and optic nerve section. *Vision Res* 2016;128:45-52.
107. Cvenkel B, Sustar M, Perovsek D. Ganglion cell loss in early glaucoma, as assessed by photopic negative response, pattern electroretinogram, and spectral-domain optical coherence tomography. *Doc Ophthalmol* 2017;135:17-28.
108. Salinas-Navarro M, Jimenez-Lopez M, Valiente-Soriano FJ, et al. Retinal ganglion cell population in adult albino and pigmented mice: a computerized analysis of the entire population and its spatial distribution. *Vision Res* 2009;49:637-647.
109. Jeffery G. The relationship between cell density and the nasotemporal division in the rat retina. *Brain Res* 1985;347:354-357.
110. FA D. The Anatomy and Histology of the Eye and Orbit of the Rabbit. *Trans Am Ophthalmol Soc.* 1929;27.
111. Do-Nascimento JL, Do-Nascimento RS, Damasceno BA, Silveira LC. The neurons of the retinal ganglion cell layer of the guinea pig: quantitative analysis of their distribution and size. *Braz J Med Biol Res* 1991;24:199-214.
112. Choudhury BP. Retinotopic organization of the guinea pig's visual cortex. *Brain Res* 1978;144:19-29.
113. Schindelin J, Arganda-Carreras I, Frise E, et al. Fiji: an open-source platform for biological-image analysis. *Nat Methods* 2012;9:676-682.
114. Schmucker C, Seeliger M, Humphries P, Biel M, Schaeffel F. Grating acuity at different luminances in wild-type mice and in mice lacking rod or cone function. *Invest Ophthalmol Vis Sci* 2005;46:398-407.

115. Jen LS, So KF, Chang AB. An anterograde HRP study of the retinotectal pathways in albino and pigmented guinea pigs. *Brain Res* 1983;263:331-335.
116. Development of postreceptor function in pigmented and albino guinea pigs | Visual Neuroscience | Cambridge Core. 2020.
117. Naderian A, Bussieres L, Thomas S, Lesage F, Casanova C. Cellular origin of intrinsic optical signals in the rabbit retina. *Vision Res* 2017;137:40-49.
118. Rosolen SG, Rigaudiere F, LeGargasson JF, et al. Comparing the photopic ERG i-wave in different species. *Vet Ophthalmol* 2004;7:189-192.
119. Bui BV, Vingrys AJ. Development of receptor responses in pigmented and albino guinea-pigs (*Cavia porcellus*). *Doc Ophthalmol* 1999;99:151-170.
120. Porciatti V. The mouse pattern electroretinogram. *Doc Ophthalmol* 2007;115:145-153.
121. Luo X, Frishman LJ. Retinal pathway origins of the pattern electroretinogram (PERG). *Invest Ophthalmol Vis Sci* 2011;52:8571-8584.
122. Ben-Shlomo G, Bakalash S, Lambrou GN, et al. Pattern electroretinography in a rat model of ocular hypertension: functional evidence for early detection of inner retinal damage. *Exp Eye Res* 2005;81:340-349.
123. Feghali JG, Jin JC, Odom JV. Effect of short-term intraocular pressure elevation on the rabbit electroretinogram. *Invest Ophthalmol Vis Sci* 1991;32:2184-2189.
124. Maffei L, Fiorentini A, Bisti S, Hollander H. Pattern ERG in the monkey after section of the optic nerve. *Exp Brain Res* 1985;59:423-425.
125. Rodriguez AR, de Sevilla Muller LP, Brecha NC. The RNA binding protein RBPMS is a selective marker of ganglion cells in the mammalian retina. *J Comp Neurol* 2013;522:1411-1443.
126. Fontaine M, Gaucher D, Sauer A, Speeg-Schatz C. Choroidal thickness and ametropia in children: a longitudinal study. *Eur J Ophthalmol* 2017;0.
127. El-Shazly AA, Farweez YA, ElSebaay ME, El-Zawahry WMA. Correlation between choroidal thickness and degree of myopia assessed with enhanced depth imaging optical coherence tomography. *Eur J Ophthalmol* 2017;27:577-584.
128. Cull GA, Reynaud J, Wang L, Cioffi GA, Burgoyne CF, Fortune B. Relationship between orbital optic nerve axon counts and retinal nerve fiber layer thickness measured by spectral domain optical coherence tomography. *Invest Ophthalmol Vis Sci* 2012;53:7766-7773.
129. Ivers KM, Sredar N, Patel NB, et al. In vivo changes in lamina cribrosa microarchitecture and optic nerve head structure in early experimental glaucoma. *PloS one* 2015;10:e0134223.

130. Fortune B, Reynaud J, Hardin C, Wang L, Sigal IA, Burgoyne CF. Experimental glaucoma causes optic nerve head neural rim tissue compression: a potentially important mechanism of axon injury. *Invest Ophthalmol Vis Sci* 2016;57:4403-4411.
131. Liu Q, Wu J, Wang X, Zeng J. Changes in muscarinic acetylcholine receptor expression in form deprivation myopia in guinea pigs. *Mol Vis* 2007;13:1234-1244.
132. Demb JB, Haarsma L, Freed MA, Sterling P. Functional circuitry of the retinal ganglion cell's nonlinear receptive field. *J Neurosci* 1999;19:9756-9767.
133. Zaghoul KA, Boahen K, Demb JB. Different circuits for ON and OFF retinal ganglion cells cause different contrast sensitivities. *J Neurosci* 2003;23:2645-2654.
134. Racine J, Behn D, Lachapelle P. Structural and functional maturation of the retina of the albino Hartley guinea pig. *Doc Ophthalmol* 2008;117:13-26.
135. Rodriguez-Ramos Fernandez J, Dubielzig RR. Ocular comparative anatomy of the family Rodentia. *Veterinary ophthalmology* 2013;16 Suppl 1:94-99.
136. Huang D, Swanson EA, Lin CP, et al. Optical coherence tomography. *Science* 1991;254:1178-1181.
137. Bussell II, Wollstein G, Schuman JS. OCT for glaucoma diagnosis, screening and detection of glaucoma progression. *Br J Ophthalmol* 2014;98 Suppl 2:ii15-19.
138. Schuman JS, Pedut-Kloizman T, Hertzmark E, et al. Reproducibility of nerve fiber layer thickness measurements using optical coherence tomography. *Ophthalmology* 1996;103:1889-1898.
139. Sander B, Larsen M, Thrane L, Hougaard JL, Jorgensen TM. Enhanced optical coherence tomography imaging by multiple scan averaging. *Br J Ophthalmol* 2005;89:207-212.
140. Sakamoto A, Hangai M, Yoshimura N. Spectral-domain optical coherence tomography with multiple B-scan averaging for enhanced imaging of retinal diseases. *Ophthalmology* 2008;115:1071-1078.e1077.
141. Lee SH, Kim SH, Kim TW, Park KH, Kim DM. Reproducibility of retinal nerve fiber thickness measurements using the test-retest function of spectral OCT/SLO in normal and glaucomatous eyes. *J Glaucoma* 2010;19:637-642.
142. Chauhan BC, O'Leary N, Almobarak FA, et al. Enhanced detection of open-angle glaucoma with an anatomically accurate optical coherence tomography-derived neuroretinal rim parameter. *Ophthalmology* 2013;120:535-543.
143. Quigley HA, Broman AT. The number of people with glaucoma worldwide in 2010 and 2020. *Br J Ophthalmol* 2006;90:262-267.

144. Gelatt KN, Gum GG, Gwin RM, Bromberg NM, Merideth RE, Samuelson DA. Primary open angle glaucoma: inherited primary open angle glaucoma in the beagle. *Am J Pathol* 1981;102:292-295.
145. Sappington RM, Carlson BJ, Crish SD, Calkins DJ. The microbead occlusion model: a paradigm for induced ocular hypertension in rats and mice. *Invest Ophthalmol Vis Sci* 2010;51:207-216.
146. Bergen MA, Park HN, Chakraborty R, et al. Altered refractive development in mice with reduced levels of retinal dopamine. *Invest Ophthalmol Vis Sci* 2016;57:4412-4419.
147. Veth KN, Willer JR, Collery RF, et al. Mutations in zebrafish *lrp2* result in adult-onset ocular pathogenesis that models myopia and other risk factors for glaucoma. *PLoS Genet* 2011;7:e1001310.
148. Harwerth RS, Crawford ML, Frishman LJ, Viswanathan S, Smith EL, 3rd, Carter-Dawson L. Visual field defects and neural losses from experimental glaucoma. *Prog Retin Eye Res* 2002;21:91-125.
149. Rachida. Animal models of glaucoma. *J Biomed Biotechnol* 2012.
150. Aires ID, Ambrosio AF, Santiago AR. Modeling human glaucoma: lessons from the in vitro models. *Ophthalmic Res* 2017;57:77-86.
151. Burgoyne CF. The non-human primate experimental glaucoma model. *Exp Eye Res* 2015;141:57-73.
152. Sun D, Lye-Barthel M, Masland RH, Jakobs TC. The morphology and spatial arrangement of astrocytes in the optic nerve head of the mouse. *J Comp Neurol* 2009;516:1-19.
153. Quigley HA, Hohman, R.M., Addicks, E.M., Massof, R.W., Green, W.R. Morphologic changes in the lamina cribrosa correlated with neural loss in open angle glaucoma. *Am J Ophthalmol* 1983;673-691.
154. Roberts MD, Grau, V., Grimm, J., Reynaud, J., Bellezza, A.J., Burgoyne, C.F., Downs, J.C. Remodeling of the connective tissue microarchitecture of the lamina cribrosa in early experimental glaucoma. *Invest Ophthalmol Vis Sci* 2009;681-690.
155. Gabriele ML, Ishikawa H, Schuman JS, et al. Reproducibility of spectral-domain optical coherence tomography total retinal thickness measurements in mice. *Invest Ophthalmol Vis Sci* 2010;51:6519-6523.
156. Lozano DC, Twa MD. Quantitative evaluation of factors influencing the repeatability of SD-OCT thickness measurements in the rat. *Invest Ophthalmol Vis Sci* 2012;53:8378-8385.

157. Yang JH, Yu SY, Kim TG, Seo KH, Kwak HW. Repeatability and Reproducibility of Spectral-Domain Optical Coherence Tomography Measurements of Retinal Thickness in Rats. *Curr Eye Res* 2016;41:1346-1352.
158. Li T, Zhou X, Luo X, Jiang B. Optical coherence tomography and histologic measurements of retinal and choroidal thicknesses in guinea pig eyes. *Int J Clin Exp Med* 2016;9:7080-7087.
159. Gawne TJ, Ward AH, Norton TT. Long-wavelength (red) light produces hyperopia in juvenile and adolescent tree shrews. *Vision Res* 2017;140:55-65.
160. Gawne TJ, Siegwart JT, Jr., Ward AH, Norton TT. The wavelength composition and temporal modulation of ambient lighting strongly affect refractive development in young tree shrews. *Exp Eye Res* 2016;155:75-84.
161. Howlett MH, McFadden SA. Emmetropization and schematic eye models in developing pigmented guinea pigs. *Vision Res* 2007;47:1178-1190.
162. Bennett AG. A method of determining the equivalent powers of the eye and its crystalline lens without resort to phakometry. *Ophthalmic Physiol Opt* 1988;8:53-59.
163. Patel NB, Luo X, Wheat JL, Harwerth RS. Retinal nerve fiber layer assessment: area versus thickness measurements from elliptical scans centered on the optic nerve. *Invest Ophthalmol Vis Sci* 2011;52:2477-2489.
164. Holden AL, Hayes BP, Fitzke FW. Retinal magnification factor at the ora terminals: a structural study of human and animal eyes. *Vision research* 1987;27:1229-1235.
165. Lapuerta P, Schein SJ. A four-surface schematic eye of macaque monkey obtained by an optical method. *Vision research* 1995;35:2245-2254.
166. Shrout PE, Fleiss JL. Intraclass correlations: uses in assessing rater reliability. *Psychol Bull* 1979;86:420-428.
167. Bland JM, Altman DG. Statistical methods for assessing agreement between two methods of clinical measurement. *Lancet* 1986;1:307-310.
168. Cui D, Trier K, Zeng J, et al. Effects of 7-methylxanthine on the sclera in form deprivation myopia in guinea pigs. *Acta Ophthalmol* 2011;89:328-334.
169. Penha AM, Burkhardt E, Schaeffel F, Feldkaemper MP. Ultrasonography and optical low-coherence interferometry compared in the chicken eye. *Optom Vis Sci* 2012;89:916-921.
170. Chaudhuri A, Hallett PE, Parker JA. Aspheric curvatures, refractive indices and chromatic aberration for the rat eye. *Vision research* 1983;23:1351-1363.

171. Huang L, Schuman J, Wang N. Comparison of nerve fiber layer thickness between optical coherence tomography and histomorphometry in glaucomatous monkey eyes. *Zhonghua Yan Ke Za Zhi* 2002;37:188-192.
172. Abbott CJ, McBrien NA, Grunert U, Pianta MJ. Relationship of the optical coherence tomography signal to underlying retinal histology in the tree shrew (*Tupaia belangeri*). *Invest Ophthalmol Vis Sci* 2009;50:414-423.
173. Bowd C, Weinreb RN, Zangwill LM. Evaluating the optic disc and retinal nerve fiber layer in glaucoma. I: Clinical examination and photographic methods. *Semin Ophthalmol* 2000;15:194-205.
174. Firat PG1 DS, Demirel EE, Colak C. Comparison of ganglion cell and retinal nerve fiber layer thickness in primary open-angle glaucoma and normal tension glaucoma with spectral-domain OCT. *Graefes Arch Clin Exp Ophthalmol* 2013;831-838.
175. Fortune B CG, Reynaud J, Wang L, Burgoyne CF. Relating retinal ganglion cell function and retinal nerve fiber layer (RNFL) retardance to progressive loss of RNFL thickness and optic nerve axons in experimental glaucoma. *Invest Ophthalmol Vis Sci* 2015;3936-3944.
176. Nakano N1 IH, Hangai M, Muraoka Y, Toda Y, Kakizuka A, Yoshimura N. Longitudinal and simultaneous imaging of retinal ganglion cells and inner retinal layers in a mouse model of glaucoma induced by N-methyl-D-aspartate. *Invest Ophthalmol Vis Sci* 2011;8754-8762.
177. Huang XR1 ZY, Kong W, Knighton RW. Reflectance decreases before thickness changes in the retinal nerve fiber layer in glaucomatous retinas. *Invest Ophthalmol Vis Sci* 2011;6737-6742.
178. Buttery RG, Hinrichsen CF, Weller WL, Haight JR. How thick should a retina be? A comparative study of mammalian species with and without intraretinal vasculature. *Vision Res* 1991;31:169-187.
179. Kocaoglu OP, Uhlhorn SR, Hernandez E, et al. Simultaneous fundus imaging and optical coherence tomography of the mouse retina. *Invest Ophthalmol Vis Sci* 2007;48:1283-1289.
180. Toyoda F, Tanaka Y, Shimmura M, Kinoshita N, Takano H, Kakehashi A. Diabetic retinal and choroidal edema in SDT rats. *J. Diabetes Res.* 2016;2016:2345141.
181. Straznicky C, Chehade M. The formation of the area centralis of the retinal ganglion cell layer in the chick. *Development* 1987;100:411-420.
182. Patel NB, Hung LF, Harwerth RS. Postnatal maturation of the fovea in *Macaca mulatta* using optical coherence tomography. *Exp Eye Res* 2017;164:8-21.
183. Cobcroft M, Vaccaro T, Mitrofanis J. Distinct patterns of distribution among NADPH-diaphorase neurones of the guinea pig retina. *Neurosci Lett* 1989;103:1-7.

184. Margolis R, Spaide RF. A pilot study of enhanced depth imaging optical coherence tomography of the choroid in normal eyes. *Am J Ophthalmol* 2009;147:811-815.
185. Entezari M, Karimi S, Ramezani A, Nikkhah H, Fekri Y, Kheiri B. Choroidal thickness in healthy subjects. *J Ophthalmic Vis Res*; 2018:39-43.
186. Ostrin LA, Garcia MB, Choh V, Wildsoet CF. Pharmacologically stimulated pupil and accommodative changes in Guinea pigs. *Invest Ophthalmol Vis Sci* 2014;55:5456-5465.
187. Jiang L, Schaeffel F, Zhou X, et al. Spontaneous axial myopia and emmetropization in a strain of wild-type guinea pig (*Cavia porcellus*). *Invest Ophthalmol Vis Sci* 2009;50:1013-1019.
188. Porciatti V, Pizzorusso T, Cenni MC, Maffei L. The visual response of retinal ganglion cells is not altered by optic nerve transection in transgenic mice overexpressing Bcl-2. *Proc Natl Acad Sci U S A* 1996;93:14955-14959.
189. Li Y, Schlamp CL, Nickells RW. Experimental induction of retinal ganglion cell death in adult mice. *Invest Ophthalmol Vis Sci* 1999;40:1004-1008.
190. Gabriele ML, Ishikawa H, Schuman JS, et al. Optic nerve crush mice followed longitudinally with spectral domain optical coherence tomography. *Invest Ophthalmol Vis Sci* 2011;52:2250-2254.
191. Munguba GC, Galeb S, Liu Y, et al. Nerve fiber layer thinning lags retinal ganglion cell density following crush axonopathy. *Invest Ophthalmol Vis Sci* 2014;55:6505-6513.
192. Allcutt D, Berry M, Sievers J. A quantitative comparison of the reactions of retinal ganglion cells to optic nerve crush in neonatal and adult mice. *Brain Res* 1984;318:219-230.
193. Jnawali A PS, Beach K, Ostrin LA. Spatial frequency discrimination in guinea pigs: functional and structural measures. *Optom Vis Sci* 2017;94.
194. Jnawali A, Beach KM, Ostrin LA. In vivo imaging of the retina, choroid, and optic nerve head in guinea pigs. *Curr Eye Res* 2018;43:1006-1018.
195. Giannakaki-Zimmermann H, Kokona D, Wolf S, Ebner A, Zinkernagel MS. Optical coherence tomography angiography in mice: comparison with confocal scanning laser microscopy and fluorescein angiography. *Transl Vis Sci Technol*; 2016.
196. Bush RA, Tanikawa A, Zeng Y, Sieving PA. Cone ERG changes during light adaptation in two All-Cone mutant mice: implications for rod-cone pathway interactions. *Invest Ophthalmol Vis Sci*; 2019:3680-3688.
197. Machida S, Gotoh Y, Toba Y, Ohtaki A, Kaneko M, Kurosaka D. Correlation between photopic negative response and retinal nerve fiber layer thickness and optic disc topography in glaucomatous eyes. *Invest Ophthalmol Vis Sci* 2008;49:2201-2207.

198. Shen X, Huang L, Fan N, He J. Relationship among photopic negative response, retinal nerve fiber layer thickness, and visual field between normal and POAG eyes. *ISRN Ophthalmol* 2014;2013:182021.
199. Machida S, Raz-Prag D, Fariss RN, Sieving PA, Bush RA. Photopic ERG negative response from amacrine cell signaling in RCS rat retinal degeneration. *Invest Ophthalmol Vis Sci* 2008;49:442-452.
200. Wachtmeister L. Oscillatory potentials in the retina: what do they reveal. *Prog Retin Eye Res* 1998;17:485-521.
201. Wachtmeister L, Dowling JE. The oscillatory potentials of the mudpuppy retina. *Invest Ophthalmol Vis Sci* 1978;17:1176-1188.
202. Rangaswamy NV, Hood DC, Frishman LJ. Regional variations in local contributions to the primate photopic flash ERG: revealed using the slow-sequence mfERG. *Invest Ophthalmol Vis Sci* 2003;44:3233-3247.
203. Dong C-j, Agey P, Hare WA. Origins of the electroretinogram oscillatory potentials in the rabbit retina. *Vis Neurosci* 2004;21:533-543.
204. DM L. Neurotransmitters in the vertebrate retina. *Invest Ophthalmol Vis Sci* 1997;38:553-556.
205. Lukasiewicz PD, Eggers ED, Sagdullaev BT, McCall MA. GABAC receptor-mediated inhibition in the retina. *Vision Res* 2004;44:3289-3296.
206. E P. Ionotropic GABA receptors and distal retinal ON and OFF responses. *Scientifica* 2014;2014.
207. J W, DK M, J Y, et al. In vivo electroretinographic studies of the role of GABAC receptors in retinal signal processing. *Experimental eye research* 2015;139.
208. Shi Q, Stell WK. Die Fledermaus: regarding optokinetic contrast sensitivity and light-adaptation, chicks are mice with wings. *PLoS One* 2013;8:e75375.
209. Grillo SL, Montgomery CL, Johnson HM, Koulen P. Quantification of changes in visual Function During Disease Development in a Mouse Model of Pigmentary Glaucoma. *J Glaucoma* 2018;27:828-841.
210. Barabas P, Huang W, Chen H, et al. Missing optomotor head-turning reflex in the DBA/2J mouse. *Invest Ophthalmol Vis Sci* 2011;52:6766-6773.
211. Malakar M, Askari SN, Ashraf H, Waris A, Ahuja A, Asghar A. Optical coherence tomography assisted retinal nerve fibre layer thickness profile in high myopia. *J Clin Diagn Res* 2015;9:Nc01-03.

212. Tang Z, Zhang S, Lee C, et al. An optic nerve crush injury murine model to study retinal ganglion cell survival. *J Vis Exp* 2011;50:2685
213. Allcutt D, Berry M, Sievers J. A qualitative comparison of the reactions of retinal ganglion cell axons to optic nerve crush in neonatal and adult mice. *Brain Res* 1984;318:231-240.
214. Huang XR, Kong W, Qiao J. Response of the retinal nerve fiber layer reflectance and thickness to optic nerve crush. *Invest Ophthalmol Vis Sci* 2018;59:2094-2103.
215. Clark YL, Colleen MM, Zhang Z, Holly ET, Robert JW, Abbot F. Monitoring retinal morphologic and functional changes in mice following optic nerve crush. *Invest Ophthalmol Vis Sci* 2014;55:3766-3774.
216. Park JR, Choi W, Hong HK, et al. Imaging laser-induced choroidal neovascularization in the rodent retina using optical coherence tomography angiography. *Invest Ophthalmol Vis Sci* 2016;57:Oct331-340.
217. Liu W, Li H, Shah RS, et al. Simultaneous optical coherence tomography angiography and fluorescein angiography in rodents with normal retina and laser-induced choroidal neovascularization. *Opt Lett* 2015;40:5782-5785.
218. Jonas JB, Budde WM, Panda-Jonas S. Ophthalmoscopic evaluation of the optic nerve head. *Surv Ophthalmol* 1999;43:293-320.
219. Samarawickrama C, Pai A, Tariq Y, Healey PR, Wong TY, Mitchell P. Characteristics and appearance of the normal optic nerve head in 6-year-old children. *Br J Ophthalmol* 2011;96:68-72.
220. Efendic A, Muharemovic E, Skomorac R, et al. Anatomic variations of posterior paranasal sinuses and optic nerve. *Med Glas (Zenica)* 2016;14:49-54.
221. Hoffmann EM, Schmidtman I, Siouli A, et al. The distribution of retinal nerve fiber layer thickness and associations with age, refraction, and axial length: the Gutenberg health study. *Graefes Arch Clin Exp Ophthalmol* 2018;256:1685-1693.
222. Ren R, Li B, Gao F, et al. Central corneal thickness, lamina cribrosa and peripapillary scleral histomorphometry in non-glaucomatous Chinese eyes. *Graefes Arch Clin Exp Ophthalmol* 2010;248:1579-1585.
223. Anderson DR. Ultrastructure of human and monkey lamina cribrosa and optic nerve head. *Arch Ophthalmol* 1969;82:800-814.
224. Yang H, Downs, J.C., Girkin, C., Sakata, L., Bellezza, A., Thompson, H., Burgoyne, C.F. 3-D histomorphometry of the normal and early glaucomatous monkey optic nerve head: lamina cribrosa and peripapillary scleral position and thickness. *Invest Ophthalmol Vis Sci* 2007;4597-4607.

225. Girkin CA, Fazio MA, Yang H, et al. Variation in the three-dimensional histomorphometry of the normal human optic nerve head with age and race: lamina cribrosa and peripapillary scleral thickness and position. *Invest Ophthalmol Vis Sci* 2017;58:3759-3769.
226. Ren R, Wang N, Li B, et al. Lamina cribrosa and peripapillary sclera histomorphometry in normal and advanced glaucomatous Chinese eyes with various axial length. *Invest Ophthalmol Vis Sci* 2009;50:2175-2184.
227. Sigal IA, Wang B, Strouthidis NG, Akagi T, Girard MJ. Recent advances in OCT imaging of the lamina cribrosa. *Br J Ophthalmol* 2014;98 Suppl 2:ii34-39.
228. Xiao H, Xu XY, Zhong YM, Liu X. Age related changes of the central lamina cribrosa thickness, depth and prelaminar tissue in healthy Chinese subjects. *Int J Ophthalmol* 2018;11:1842-1847.
229. Rhodes LA, Huisinigh C, Johnstone J, et al. Variation of laminar depth in normal eyes with age and race. *Invest Ophthalmol Vis Sci* 2014;55:8123-8133.
230. Lee EJ, Kim TW, Weinreb RN, Suh MH, Kim H. Lamina cribrosa thickness is not correlated with central corneal thickness or axial length in healthy eyes: central corneal thickness, axial length, and lamina cribrosa thickness. *Graefes Arch Clin Exp Ophthalmol* 2012;251:847-854.
231. Lee JW, Yau GS, Woo TT, Yick DW, Tam VT, Lai JS. Retinal nerve fiber layer thickness in myopic, emmetropic, and hyperopic children. *Medicine (Baltimore)* 2015;94:e699.
232. Read SA, Alonso-Caneiro D, Vincent SJ, Collins MJ. Peripapillary choroidal thickness in childhood. *Exp Eye Res* 2015;135:164-173.
233. Wu XS, Shen LJ, Chen RR, Lyu Z. Peripapillary choroidal thickness in Chinese children using enhanced depth imaging optical coherence tomography. *Int J Ophthalmol* 2016;9:1451-1456.
234. Zhao L, Wang Y, Chen CX, Xu L, Jonas JB. Retinal nerve fibre layer thickness measured by Spectralis spectral-domain optical coherence tomography: The Beijing Eye Study. *Acta Ophthalmol* 2013;92:e35-41.
235. Savini G, Barboni P, Parisi V, Carbonelli M. The influence of axial length on retinal nerve fibre layer thickness and optic-disc size measurements by spectral-domain OCT. *Brit J Ophthalmol* 2011;96:57-61.
236. Oner V, Ozgur G, Turkyilmaz K, Sekeryapan B, Durmus M. Effect of axial length on retinal nerve fiber layer thickness in children. *Eur J Ophthalmol* 2014;24:265-272.
237. Ivers KM, Li C, Patel N, et al. Reproducibility of measuring lamina cribrosa pore geometry in human and nonhuman primates with in vivo adaptive optics imaging. *Invest Ophthalmol Vis Sci* 2011;52:5473-5480.

238. Li KY, Tiruveedhula P, Roorda A. Intersubject variability of foveal cone photoreceptor density in relation to eye length. *Invest Ophthalmol Vis Sci* 2010;51:6858-6867.
239. Mutti DO, Zadnik K, Fusaro RE, Friedman NE, Sholtz RI, Adams AJ. Optical and structural development of the crystalline lens in childhood. *Invest Ophthalmol Vis Sci* 1998;39:120-133.
240. Girard MJ, Strouthidis NG, Ethier CR, Mari JM. Shadow removal and contrast enhancement in optical coherence tomography images of the human optic nerve head. *Invest Ophthalmol Vis Sci* 2011;52:7738-7748.
241. Sredar N, Ivers KM, Queener HM, Zouridakis G, Porter J. 3D modeling to characterize lamina cribrosa surface and pore geometries using in vivo images from normal and glaucomatous eyes. *Biomed Opt Express* 2013;4:1153-1165.
242. Jonas JB, Gusek GC, Naumann GO. Optic disk morphometry in high myopia. *Graefes Arch Clin Exp Ophthalmol* 1988;226:587-590.
243. Seo JH, Kim TW, Weinreb RN. Lamina cribrosa depth in healthy eyes. *Invest Ophthalmol Vis Sci* 2014;55:1241-1251.
244. Knight OJ, Girkin CA, Budenz DL, Durbin MK, Feuer WJ. Effect of race, age, and axial length on optic nerve head parameters and retinal nerve fiber layer thickness measured by Cirrus HD-OCT. *Arch Ophthalmol* 2012;130:312-318.
245. Elia N, Pueyo V, Altemir I, Oros D, Pablo LE. Normal reference ranges of optical coherence tomography parameters in childhood. *Br J Ophthalmol* 2012;96:665-670.
246. Araie M, Iwase A, Sugiyama K, et al. Determinants and characteristics of Bruch's membrane opening and Bruch's membrane opening-minimum rim width in a normal Japanese population. *Invest Ophthalmol Vis Sci* 2017;58:4106-4113.
247. Wenner Y, Brauer V, Kunze K, et al. Comparison of optic disc parameters in hyperopic and emmetropic eyes of healthy children with HRT and OCT. *Klin Monbl Augenheilkd* 2017;235:1129-1137.
248. Jonas JB. Optic disk size correlated with refractive error. *Am J Ophthalmol* 2005;139:346-348.
249. Patel A, Purohit R, Lee H, et al. Optic nerve head development in healthy infants and children using handheld spectral-domain optical coherence tomography. *Ophthalmology* 2016;123:2147-2157.
250. Tun TA, Sun CH, Baskaran M, et al. Determinants of optical coherence tomography-derived minimum neuroretinal rim width in a normal Chinese population. *Invest Ophthalmol Vis Sci* 2015;56:3337-3344.

251. Sastre-Ibanez M, Martinez-de-la-Casa JM, Rebolleda G, et al. Utility of Bruch membrane opening-based optic nerve head parameters in myopic subjects. *Eur J Ophthalmol* 2017;28:42-46.
252. Barrio-Barrio J, Noval S, Galdos M, et al. Multicenter Spanish study of spectral-domain optical coherence tomography in normal children. *Acta Ophthalmol* 2013;91:e56-63.
253. Al-Haddad C, et al. Spectral domain optical coherence tomography in children: normative data and biometric correlations. *BMC Ophthalmol*. 2014;14:53
254. Molnar A, Holmstrom G, Larsson E. Macular thickness assessed with spectral domain OCT in a population-based study of children: normative data, repeatability and reproducibility and comparison with time domain OCT. *Acta Ophthalmol* 2015;93:470-475.
255. Read SA, Collins MJ, Vincent SJ, Alonso-Caneiro D. Macular retinal layer thickness in childhood. *Retina* 2015;35:1223-1233.
256. Eslami Y, Vahedian Z, Moghimi S, et al. Peripapillary retinal nerve fiber layer thickness in normal Iranian children measured with optical coherence tomography. *J Ophthalmic Vis Res* 2018;13:453-457.
257. Gama R, Santos JC, Costa RS, da Costa DC, Eiro N. Optical coherence tomography analysis of the inner retinal layers in children. *Can J Ophthalmol* 2018;53:614-620.
258. Chen CY, Huang EJC, Kuo CN, et al. The relationship between age, axial length and retinal nerve fiber layer thickness in the normal elderly population in Taiwan: The Chiayi eye study in Taiwan. *PLoS One*; 2018.
259. Cohen MJ, Kaliner E, Frenkel S, Kogan M, Miron H, Blumenthal EZ. Morphometric analysis of human peripapillary retinal nerve fiber layer thickness. *Invest Ophthalmol Vis Sci* 2008;49:941-944.
260. Bendschneider D, Tornow RP, Horn FK, et al. Retinal nerve fiber layer thickness in normals measured by spectral domain OCT. *J Glaucoma* 2010;19:475-482.
261. Feuer WJ, et al. Topographic differences in the age-related changes in the retinal nerve fiber layer of normal eyes measured by Stratus optical coherence tomography. - PubMed - NCBI. 2018.
262. Zhang JM, Wu JF, Chen JH, et al. Macular choroidal thickness in children: the Shandong children eye study. *Invest Ophthalmol Vis Sci* 2015;56:7646-7652.
263. Zha Y, Zhuang J, Du Y, Cai J, Zheng H. Evaluation of peripapillary choroidal distribution in children by enhanced depth imaging optical coherence tomography. *BMC Ophthalmol* 2018;18:173.
264. Ostrin LA, Jnawali A, Carkeet A, Patel NB. Twenty-four hour ocular and systemic diurnal rhythms in children. *Ophthalmic Physiol Opt* 2019;39(5);358-369.

265. Sayin N, Kara N, Pekel G, Altinkaynak H. Choroidal thickness changes after dynamic exercise as measured by spectral-domain optical coherence tomography. *Indian J Ophthalmol* 2015;63:445-450.
266. Burfield HJ, Patel NB, Ostrin LA. Ocular biometric diurnal rhythms in emmetropic and myopic adults. *Invest Ophthalmol Vis Sci* 2018;59:5176-5187.
267. Zhang Z, Zhou Y, Xie Z, et al. The effect of topical atropine on the choroidal thickness of healthy children. *Sci Rep* 2016;6:34936.
268. Oner V, Bulut A, Oter K. The effect of topical anti-muscarinic agents on subfoveal choroidal thickness in healthy adults. *Eye (Lond)* 2016;30:925-928.
269. Sieving PA, Steinberg RH. Proximal retinal contribution to the intraretinal 8-Hz pattern ERG of cat. *J Neurophysiol* 1987;57:104-120.
270. Harrison JM, O'Connor PS, Young RS, Kincaid M, Bentley R. The pattern ERG in man following surgical resection of the optic nerve. *Invest Ophthalmol Vis Sci* 1987;28:492-499.
271. Berger A, Cavallero S, Dominguez E, et al. Spectral-Domain optical coherence tomography of the rodent eye: highlighting layers of the outer retina using signal averaging and comparison with histology. *PLoS One*; 2014.
272. Slaughter MM, Miller RF. 2-amino-4-phosphonobutyric acid: a new pharmacological tool for retina research. *Science* 1981;211:182-185.
273. Slaughter MM, Miller RF. Bipolar cells in the mudpuppy retina use an excitatory amino acid neurotransmitter. *Nature* 1983;303:537-538.
274. Hille B. Common mode of action of three agents that decrease the transient change in sodium permeability in nerves. *Nature* 1966;210.
275. Cui J, Pan ZH. Two types of cone bipolar cells express voltage-gated Na<sup>+</sup> channels in the rat retina. *Visual neuroscience* 2008;25.
276. El-Nimri NW, Wildsoet CF. Effects of topical latanoprost on intraocular pressure and myopia progression in young guinea pigs. *Invest Ophthalmol Vis Sci* 2018;59.